

DOCTORAL THESIS

Displacements Analysis in Layered Rock Masses

JUAN MANUEL DAVILA MENDEZ

Institute for Rock Mechanics and Tunneling

Graz University of Technology

Reviewer:

O.Univ.-Prof. Dipl.-Ing. Dr.mont. Wulf Schubert

Institute for Rock Mechanics and Tunneling

Graz University of Technology

Graz, November 2015

Declaration

I declare in lieu of oath that I did this thesis in hand by myself using only literature cited at the end of this work.

Graz, November 2015

Juan Manuel Dávila Méndez

ACKNOWLEDGMENTS

I would like to express my sincere appreciation and gratitude to O.Univ.-Prof. Dipl.-Ing. Dr.mont. Wulf Schubert for his kind supervision, suggestions and help towards the completion of this thesis.

Finally, I wish to express my sincere gratitude to my dear family especially my parents for their continuing love and support. I would not have achieved this goal without their patience, understanding and encouragement.

ABSTRACT

The ground behavior is a key element of a geotechnical design of underground structures. According to the recommendation of the Austrian Society of Geomechanics, understanding failure mechanisms is of utmost importance for a reliable design, geological model updating and serves as aid for the observational approach in order to achieve a correct interpretation of monitoring data during construction.

Ground behavior and displacement patterns are strongly influenced by the relative orientation of the weakness planes (foliation/discontinuities) with respect to the direction and orientation of the tunnel axis.

In addition to the discontinuities orientation, primary stress magnitude and orientation, intrinsic properties of the rock mass and joints influence the rate and development of the tunnel closure. A numerical model was implemented and calibrated with the help of case studies. Through this model it was possible to achieve a large number of cases by varying the factors influencing the displacements.

The present work evaluates the influence of weakness planes on the displacement trends and ground behavior. A summary of its influence on the spatial displacement characteristic is provided, as well as a prediction tool developed, serving as an aid for tunnel engineers.

KURZFASSUNG

Das Wissen über des Gebirgsverhalten ist ein Schlüsselement der geotechnischen Planung von Hohlraumbauten. Gemäß der Empfehlung der Österreichischen Gesellschaft für Geomechanik, ist das Verständnis des Versagensmechanismus von größter Bedeutung für eine zuverlässige Planung und für die Anpassung des geologischen Modells, und dient als Hilfe für die Beobachtungsmethode um eine korrekte Auswertung der Messdaten während der Bauphase zu erzielen.

Gebirgsverhalten und Verschiebungsmuster werden stark von der relativen Orientierung von Störungzonen (Schieferung/Trennflächen) in Bezug auf die Richtung und Orientierung zur Tunnelachse beeinflusst.

Neben der Trennflächenorientierung beeinflussen sowohl Größe und Richtung des Primärspannungszustandes, als auch die spezifischen Gebirgs- und Trennflächeneigenschaften die Größe und die Entwicklung der Verformungen in der Tunnellaibung. Ein numerisches Modell wurde implementiert und mit Hilfe von Fallstudien kalibriert. Anhand dieses Modells war es möglich eine große Anzahl von Fällen durch Änderung der Einflussfaktoren zu erzielen.

Die vorliegende Arbeit untersucht den Einfluss von Schwächezonen auf Verschiebungstrends und Gebirgsverhalten. Eine Zusammenfassung der Einflüsse auf die Verschiebungscharakteristik wird erstellt ein Prognosetool entwickelt, welche als praktisches Hilfsmittel für den Tunnelbau Ingenieur dienen sollen.

ABBREVIATIONS

τ	Shear strength / stress
σ_{1-3}	Stress Components
E	Young's modulus
c	Cohesion
φ	Friction angle
R_{adm}	Admissible error
K_o	lateral earth pressure coefficient
H	Overburden
β	Displacement rotation beta 2D
α	Displacement rotation alpha 3D
J_coh.	Weakness plane cohesion
J_fric.	Weakness plane friction angle
BEM	Boundary Element Method
DEM	Displacement Evaluation Model
DD	Dip Direction
Eqn	Equation
FDM	Finite Difference Method
FEM	Finite Element Method
FVM	Finite Volume Method
NATM	New Austrian Tunneling Method
PDA	Partial Differential Equation
UCS	Unconfined Compressive Strength
UDEC	Universal Distinct Element Code

Table of contents

ACKNOWLEDGMENTS	III
ABSTRACT	IV
KURZFASSUNG.....	V
ABBREVIATIONS.....	VI
1. INTRODUCTION	1
1.1. Problem Description and Aim of this Work	1
1.2. Methodology	2
2. LITERATURE REVIEW	4
2.1. Ground Characterization.....	4
2.1.1. Key parameters	5
2.2. Ground Behavior.....	6
2.2.1. In-situ stress	7
2.2.2. Size and shape of the excavation	8
2.2.3. Relative orientation of geological structures (discontinuities)	10
2.2.4. Geotechnical model	12
2.3. Modeling Methods	14
2.3.1. Simplified models.....	14
2.3.2. Numerical methods.....	17
2.4. Monitoring Data Evaluation.....	23
3. FLAC3D NUMERICAL MODEL	26
3.1. Numerical Model Geometry	27
3.2. Model Implementation	28
3.3. Displacement Data Post-Processing	30
3.4. Numerical Model Validation	33
3.4.1. Implemented structural elements	36
3.4.2. Calibrated cross sections Galgenberg tunnel.....	38
3.4.3. Results validation.....	42
4. NUMERICAL MODEL RESULTS	49
4.1. Variation of Weakness Plane Orientation	51
4.1.1. Dip direction 000.....	51
4.1.2. Dip direction 180.....	54
4.1.3. Dip direction 090.....	59

4.1.4.	Dip direction 045.....	63
4.1.5.	Dip direction 225.....	65
4.2.	Material Properties Influence on the Displacement Behavior	69
4.2.1.	Scatter plots.....	69
5.	DISCUSSION	77
5.1.	Observed Trends	77
5.1.1.	Weakness plane orientated perpendicular to the tunnel axis.....	78
5.1.3.	Weakness planes in tunneling direction, acute angle between tunnel axis and weakness plane dip direction	79
5.1.4.	Weakness planes against tunneling direction, acute angle between tunnel axis and weakness plane dip direction	82
5.1.5.	Influence of material properties	84
5.2.	General Trend Overview.....	86
5.3.	Practical Application	91
5.3.1.	Design stage.....	91
5.3.2.	Construction stage.....	93
5.4.	Limitations and Recommendation for Further Investigations	94
6.	INTERFACE FOR DISPLACEMENT BEHAVIOR PREDICTION	97
6.1.	Interface Components	98
6.1.1.	Input section	99
6.1.2.	Output section.....	102
6.2.	Interface Assessment with Monitored Displacement Data.....	103
6.2.1.	Galgenberg tunnel	104
6.2.2.	Strengen tunnel	106
6.2.3.	Inntal tunnel	108
7.	CONCLUSIONS	110
8.	REFERENCES	111

List of Figures

Fig. 1:	Geotechnical approach.....	4
Fig. 2:	Influence of a discontinuity on the intact rock strength.....	8
Fig. 3:	Stress distribution on an elastic material A) In-situ stress B) Stress redistribution after excavation.....	9
Fig. 4:	Discontinuity orientation favorability estimate [37]	11
Fig. 5:	Ground behavior (bending/sliding) for multiple dip angles after Vardar [39]	12
Fig. 6:	Geotechnical model engineering parameters [46].....	13
Fig. 7:	Methods for rock mechanics modeling [47].....	14
Fig. 8:	Excavation sequence and support system after Rziha [48].....	15
Fig. 9:	UDEC simulation results, joint dip 90°, 60°, 30°, 00°. [1].....	18
Fig. 10:	Foliated rocks mass _ Button et al. [62].....	19
Fig. 11:	Cases studied by Wittke [68]	21
Fig. 12:	Shear and normal stress parallel to the schistosity (left) and deformation of the opening (right), after Wittke [68]	22
Fig. 13:	Schematic showing (a) erroneous shear that may arise in the ubiquitous joint model and (b) flexural toppling failure [2].....	23
Fig. 14:	Displacement vector plot a) cross section (b) longitudinal section. Geofit®	24
Fig. 15:	Flac3D weakness plane failure criterion [79]	26
Fig. 17:	Flac3D model geometry, excavation geometry	28
Fig. 18:	Model implementation flow chart	29
Fig. 19:	Local coordinate system and conventions	30
Fig. 20:	Conventions summary.....	31
Fig. 21:	Conventions summary examples, displacement scale 1:100.....	31
Fig. 22:	Results for DD=045, dip angle=20°	32
Fig. 23:	Results graphical representation, homogeneous model vs. DD90D45	33
Fig. 24:	Numerical model and monitoring points used for calibration at the Galgenberg tunnel project.....	34
Fig. 25:	Flow chart for the numerical model calibration.....	35
Fig. 26:	Shell elements E-modulus strength increment.....	37
Fig. 27:	Geological mapping, cross section: km 0+296.....	39
Fig. 28:	Geological mapping, cross section: km 0+340.....	39
Fig. 29:	2D Numerical model, cross section: km 0 + 296.....	40
Fig. 30:	Numerical model construction concept, cross section: km 0 + 290	41
Fig. 31:	Numerical model construction concept, cross section: km 0 + 340	42
Fig. 32:	Galgenberg tunnel vertical displacements, cross section: km 0+290	44
Fig. 33:	Galgenberg tunnel longitudinal displacements, cross section: km 0+340	45
Fig. 34:	Comparison monitored data vs. numerical model results, cross section: km 0+290.....	46

Fig. 35: Galgenberg tunnel displacements, cross section: km 0+290	46
Fig. 36: Comparison monitored data vs. numerical model results, cross section: km 0+340	47
Fig. 37: Galgenberg tunnel displacements, cross section: km 0+340	47
Fig. 38: Performed simulations summary	49
Fig. 39: Example DD000/Dip20 (left) and beta vs. homogenous models results (right).....	52
Fig. 40: Alpha results DD000 ($\sigma_1=6.25\text{MPa}$) and longitudinal cross section.....	53
Fig. 41: Alpha results DD000	53
Fig. 42: Normalized tunnel closure vs. distance to the face	54
Fig. 43: Example DD180/Dip70 (left) and radial displacements DD180 (right).....	55
Fig. 44: Alpha results DD180 ($\sigma_1=12.5\text{MPa}$). Longitudinal section, displacements scale 100:1	55
Fig. 45: Alpha results DD180 for σ_1 equal to 6.25MPa, 12.5 MPa, 18.75 MPa and 25 MPa	56
Fig. 46: Stress YY redistribution for DD180Dip60 A) $\sigma_1 = 12.5\text{MPa}$ and B) $\sigma_1 = 25\text{MPa}$	56
Fig. 47: Radial displacement variation for DD=000 and DD=180.....	57
Fig. 48: Alpha variation results for DD=000 and DD=180	57
Fig. 49: Displacement development for tunneling towards and against the weakness plane orientation.....	58
Fig. 50: Flac3D_SYY results for DD000D20 and DD180D20	58
Fig. 51: Flac3D_SXY results for DD090D90, DD090D20 and DD090D50	59
Fig. 52: Flac3D ubiquitous block state plot for DD090	60
Fig. 53: Alpha and beta results for DD090 ($\sigma_1 = 6.25\text{MPa}$)	61
Fig. 54: Percentage of displacement ahead of the face for DD090.....	62
Fig. 55: Variation of displacement ahead of the face for DD090Dip45.....	62
Fig. 56: Longitudinal displacements for DD045	63
Fig. 57: Radial and tangential displacements for DD000, DD045 and DD090 ($\sigma_1=6.25\text{MPa}$)	64
Fig. 58: Percentage of displacements ahead of the face for DD045	65
Fig. 59: Radial and tangential displacements for DD045 and DD225	66
Fig. 60: Alpha results for DD045 and DD225.....	67
Fig. 61: Variation of displacements ahead of the face for DD045/Dip45 and DD135/Dip45.....	68
Fig. 62: Displacements development for DD045 and DD225.....	68
Fig. 63: Scatter plots monitored points	70
Fig. 65: State plot for matrix (left) and weakness plane (right). Matrix friction angle equal to 20°	72
Fig. 66: Scatter plots, Δ beta vs. Elastic modulus	72
Fig. 67: Scatter plots, Δ alpha vs. Matrix friction angle.....	73
Fig. 68: Scatter plots, Displacement magnitude vs. Weakness plane cohesion.....	73
Fig. 69: Scatter plots, Displacement magnitude vs. Weakness plane friction angle	74

Fig. 70: Scatter plots, Δ beta vs. Weakness plane cohesion and friction angle.....	75
Fig. 71: Scatter plots, Δ alpha vs. Weakness plane cohesion and friction angle.....	75
Fig. 72: Comparison weakness plane DD015 (left) and DD045 (right).....	80
Fig. 73: Alpha results for DD000, DD045 and DD090.....	81
Fig. 74: Percentage of displacements ahead of the face for DD015, DD045 and DD090 ($\sigma_1 = 6.25\text{MPa}$).....	82
Fig. 75: Percentage of displacement ahead of the face for DD090, DD135 and DD160 ($\sigma_1 = 6.25\text{MPa}$).....	83
Fig. 76: Radial displacements variation for different J_coh values.....	85
Fig. 77: State plot for J_coh=3MPa/J_fric=20° (left) and J_coh=1MPa/J_fric=30° (right).....	85
Fig. 78: Scatter plots, Displacements vs. Dip angles for DD045.....	87
Fig. 79: Dip angle in which maximum displacements were registered for different dip directions.....	87
Fig. 80: Scatter plots, Displacements vs. Dip directions.....	88
Fig. 81: Scatter plots, Displacements vs. Dip directions.....	89
Fig. 82: Dip angle in which maximum beta (left) and alpha (right) rotation were registered for different dip directions.....	89
Fig. 83: Beta behavior at different dip directions and dip angles.....	90
Fig. 84: Alpha behavior at different dip directions and dip angles.....	90
Fig. 85: Design considering for homogeneous ground (left) and ground considering discontinuities influence (right).....	92
Fig. 86: Tunnel 6A, road Bogota-Villavicencio.....	93
Fig. 87: Displacement vector deviation.....	94
Fig. 88: Tangential and radial displacements for different stress conditions (DD045/Dip45).....	95
Fig. 89: Displacements contour plot for DD135/Dip45 ($\sigma_1 = 25\text{MPa}$).....	95
Fig. 90: Failure mechanism for DD270/Dip30 ($\sigma_1 = 6.25\text{MPa}$).....	96
Fig. 91: Example of a surface summarizing displacement magnitude results, monitoring point P9.....	98
Fig. 92: Graphical user interface (GUI) for displacement behavior prediction.....	98
Fig. 93: Feder's solution extension to include intermediate points.....	99
Fig. 94: Handling of weakness plane strength properties in the displacement characteristics.....	100
Fig. 95: Graphical results deliver by the interface.....	102
Fig. 96: Results deliver by the interface.....	103
Fig. 97: Displacements prediction and monitored data (Geofit®) _ Galgenberg tunnel, cross section: k 0+290.....	104
Fig. 98: Comparison between monitored and predicted displacements _ Galgenberg tunnel, cross section: k 0+290.....	105
Fig. 99: Displacements prediction and monitored data (Geofit®) _ Galgenberg tunnel, cross section: k 0+770.....	105
Fig. 100: Displacements prediction and monitored data (Geofit®) _ Galgenberg tunnel, cross section: k 0+770.....	106

Fig. 101: Displacements prediction and monitored data (Geofit®) _ Strengen tunnel, cross section: k 2+025	107
Fig. 102: Comparison between monitored and predicted displacements _ Strengen tunnel, cross section: k 2+025.....	107
Fig. 103: Displacements prediction and monitored data (Geofit®) _ Strengen tunnel, cross section: k 3+364	108
Fig. 104: Comparison between monitored and predicted displacements _ Inntal tunnel, cross section: k 3+364	109

List of Tables

Table 1: Discontinuities consideration in rock mass classification systems	16
Table 2: Input parameters	30
Table 3: Shotcrete input parameters	36
Table 4: Strength factor_shotcrete	36
Table 5: Rock bolts input parameters	37
Table 6: Steel arches (HEB100) input parameters	38
Table 7: Initial material properties and boundary conditions	40
Table 8: Calibrated material properties and boundary conditions	43
Table 9: Input parameters	50

1. INTRODUCTION

Understanding rock mass behavior influenced by discontinuities is a task a tunneling engineer has to face when characterizing ground and system behaviors. Mechanical properties in layered rock masses and its influence on a tunnel excavation will strongly depend on the direction and orientation of the tunnel axis with respect to the dominant discontinuity set and the intrinsic properties of the rock mass and joints. Goricki et al. [1] described the understanding of behavior changes due to discontinuity relative orientation as “invaluable”. Such understanding leads to appropriate excavation and support design, reducing risks and saving cost.

Through computational tools it is possible to simulate such behaviors as a continuum-layered medium (e.g. ubiquitous joint model from Flac3D). Such models account for the presence of an orientation of weakness (weak plane) in a Mohr Coulomb based model. The simplification can be formulated as long as consistency and statistical homogeneity in joint properties and spacing can be established [2].

The present work identifies behaviors and failure mechanisms associated with layered rock masses. More than 400 simulations were performed in a finite difference method based computational program (Flac3D from Itasca), which includes the so called Ubiquitous Joint Model, a constitutive model that allows one to simulate a set of discontinuities and its effect on the displacements magnitude and orientation development as the tunnel excavation advances.

1.1. Problem Description and Aim of this Work

There are two main goals the present work attempts to achieve, on the one hand it should assist tunnel designers on assessing the influence of discontinuities on the ground behavior and on the other hand for geotechnical model validation based on a correct interpretation of monitored data during construction.

In empirical rock mass classification systems discontinuities are “smeared” into a continuum, thus specific effects on the behavior are lost. Despite this, their use is a common approach used by tunnel designers. Such classification systems focus on qualitatively characterizing the ground in order to analytically evaluate tunnel support requirements. Several authors and institutions have highlighted the inherent shortcomings of such practices [3], [4], [5], [6], [7], [8] and [9].

Even though systems such as Geological Strength Index (GSI) [10] make an attempt to include the influence of discontinuities into the model by reducing the rock mass strength properties for different geological conditions, it cannot take into account the real influence of the discontinuities. Such systems deliver modified strength and deformability parameters usually used as input parameters for continuum numerical models. This common approach leads to errors in the prediction of failure mechanisms during design. The present study attempts to

assess the ground behavior based on the ubiquitous joint model from Flac3D. The model is considered a useful tool and requires relative low computational effort; however, it is important to bear in mind the drawbacks of a joint smeared continuum model and to set clear limits for its implementation.

During construction a problem often encountered is the correct interpretation of displacement monitoring data. The interpretation is fundamental for a ground model redefinition which, at the same time, leads to a system behavior update. An important tool for updating the geotechnical design and covering uncertainties contained in the geotechnical design is the observational approach which is strictly bounded to displacement monitoring [11]. Successful experience has been achieved by correctly implementing the observational approach in combination with the so called New Austrian Tunneling Method (NATM) [12], [13], [14]. The authors acknowledge that the observational approach has to be linked to the surrounding rock mass (including discontinuities) to attain an appropriate design update.

The present work presents the influence and importance of the inclusion of discontinuities during design. Recommendations are given on the implementation of smeared/ubiquitous approaches and a summary on the influence of discontinuities on the spatial displacement is displayed as an aid for designers and to properly interpret the ground behavior during construction.

1.2. Methodology

A literature review is made focusing on tunnels driven in rock masses influenced by discontinuities. Firstly an appraisal on the ground characterization is carried out emphasizing geotechnical relevant parameters (key parameters) that govern and influence the behavior of such rock masses (joint/rock strength properties, texture, persistence, etc.).

In a second step literature on discontinuities influence on ground behavior is reviewed in connection to the already assessed key parameters. As an introduction to the numerical model a summary on analysis methods for layered rock masses is presented, highlighting the advantages and disadvantages of the selected numerical method and constitutive model (Ubiquitous joint model - Flac3D).

It is important to state that the behavior referred to in the present work is defined by in-situ stresses, shape and size of the excavations (full face excavation) in combination with the relative orientation of discontinuities. No considerations are made regarding support and excavation sequences.

The next chapter deals with the numerical model and its validation. The model was assembled in order to evaluate and analyze the displacement characteristics with variation of joint/rock mass properties and relative orientation of discontinuities. However, before the numerical model was fully implemented a validation procedure was performed based on the absolute displacement data from Galgenberg tunnel; by comparing displacement magnitude and orientation (displacement vector) from monitored data and the numerical results. It is shown

that continuous models (Ubiquitous constitutive model) are able to accurately reflect/simulate the ground behavior under certain boundary condition.

The present work deals with considerable amount of data, requiring structured post processing. The post-processing procedure is presented, including a procedure for data handling and comparison. The procedure discards known erroneous result¹ to decrease statistical biases on the results, taking into account the restrictions of the selected constitutive model and numerical method.

This study concludes presenting the main findings regarding the influence of discontinuities on the ground behavior and displacement development, recommendations on the usage of the ubiquitous joint model are made and finally a computational displacement prediction tool with the implementation of the findings is presented.

¹ Erroneous results are given by the shortcomings of the selected constitutive model, shortcomings are further explained in chapter 2.3.2)

2. LITERATURE REVIEW

A study on displacements is a challenging task due to the amount of influencing factors that directly affect displacements e.g. stress distribution, size/shape of the excavation and multiple properties of the rock mass and the discontinuities among others factors. The following review focuses on the main relevant factor for this research.

2.1. Ground Characterization

The characterization mentioned in this chapter mainly refers to the recommendation given by the guideline of the Austrian Society of Geomechanics [15]. It is worth mentioning that the scope of this work is the assessment of the ground behavior, which is defined as the “reaction of the ground to the excavation of the full profile without considerations of sequential excavation and support” (Fig. 1). The Austrian approach includes selecting excavation sequences and support requirements (system behavior) based on the evaluated ground behavior and subsequently evaluating the resulting system behavior.

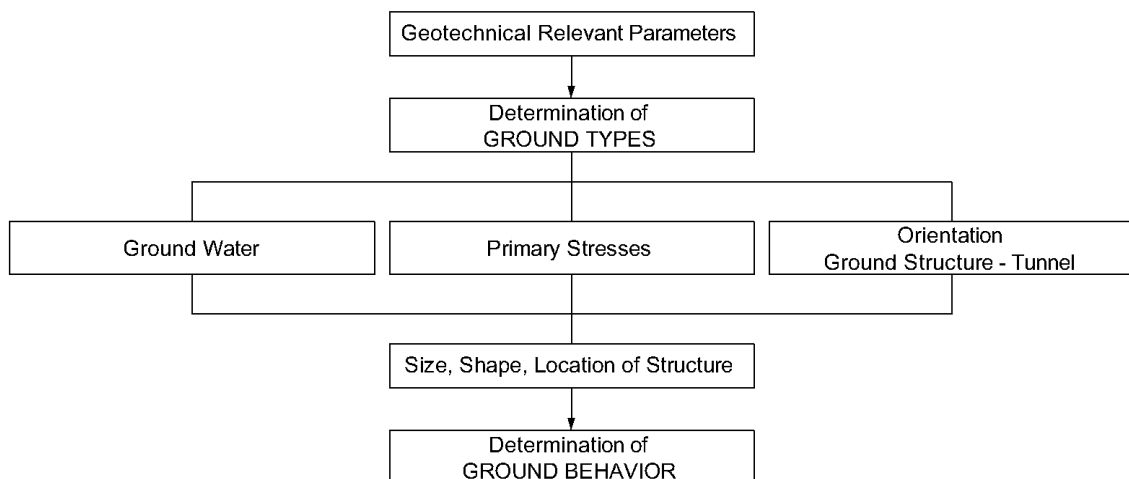


Fig. 1: Geotechnical approach

Different approaches to achieve a reliable characterization of the rock mass have been proposed having as a common ground a fair prediction of the ground behavior. The Austrian guideline firstly defines the key parameters in order to define ground types, which in combination with factors such as stress conditions, ground water conditions and construction process result in a complete prediction of the behavior. The key parameters included in the analysis, depends on their importance to the mechanical behavior, as well as the project specific requirements.

2.1.1. Key parameters

The key parameters are defined by the British standards Institution [16] as those parameters which describe the geotechnical relevant properties of the ground.

Button & Bluemel [17] and Button [18] carry out an intensive study on the set of parameters that govern the behavior of jointed rock masses, their research highlights the relevance of discontinuity properties such as:

- Foliation and joint characteristics: refers to roughness given by structural features, mineralogical composition and discontinuities filling. Button highlights that foliation/schistosity planes, unlike structural joints, are formed through a ductile deformation process creating significant tensile strength in highly persistent structures.
- Persistence: is expressed as a limit length ratio along a given line on a joint plane, and is of utmost importance to the rock mass strength [19].
- Joint shear strength: refers to the strength of the ground against a sliding failure along a plane that is parallel to the direction of the load and it is quantified based on the joint characteristics such as:
 - Joint friction angle
 - Cohesive strength of the surface
 - Dilatancy angle
 - Joint wall compressive strength (JCS) [20]
 - Joint roughness coefficient (JRC)

The researchers mainly underlined the importance of comparing laboratory results to 3D absolute displacements monitored data to validate the results and secondly, and probably the most important conclusion for the scope of this work, that “for a given rock mass structure –set of parameters- there is a characteristic displacement pattern”.

Most publications in the literature concede that the mentioned parameters govern the behavior of jointed rock masses, yet there are different procedures to obtain those parameters.

Laboratory testing results constitute one of the main sources of data for rock and joint parameters. New techniques and procedures have been developed for jointed material, delivering more accurate results. The standardized results ease the understanding of the rock mass behavior and the validation of the results is highly dependent on the quantity, quality of the test and the interpretation of the results.

In order to obtain peak and residual parameters for discontinuities in jointed rocks Bluemel & Bezat [21] developed a direct shearing test. Their procedure allows the simulation of specific boundary conditions and multiple stage shearing tests. There are clear advantages from the procedure, on the one hand, it allows the study of multiple boundary conditions with the usage of one sample and on the other hand,

its results, in combination with rock triaxial test, allow the usage of discontinuous models which requires separate input values for intact rock parameters (triaxial test) and joint properties (shearing test) [22].

A different approach was proposed by Jade and Sitharam [23]. Their research characterizes jointed rock masses based on statistical analysis of the intact rock properties in combination to the so called “joint factor” which summarizes spacing and orientation of joints (from the core sample). The authors develop an empirical equation which delivers the rock mass equivalent properties such as uniaxial compressive strength and elastic modulus of the rock mass considering joint features. The disadvantage of this procedure is that the usage of the equivalent properties homogenizes the ground in any numerical simulation, similar to the usage of the GSI [24] value. Such approaches, in most cases, cannot reflect the displacement pattern/behavior of the tunnel under construction.

In-situ characterization is a common practice in order to assign ground properties to the rock mass, Palmström [25] summarizes the in-situ characterization of jointed rock masses procedures as follow:

- The degree of jointing, including:
 - Density of joints
 - Jointing pattern;
 - Orientation of joint set or main discontinuities;
- The joint characteristics, consisting of:
 - Joint roughness (smoothness and waviness or planarity);
 - Joint condition or alteration (condition of joint walls and filling material)
- The rock material through which the joints intersect:
 - Strength and elastic properties of the rock;
 - Rock anisotropy;
 - Content of certain minerals with special properties (swelling, elastic, soluble, etc.).

2.2. Ground Behavior

The ground behavior is defined by the Austrian guideline as the reaction of the ground to a full face excavation, considering the already defined key parameters (summarized as Ground Types) and particular conditions such as in-situ stress, water conditions, shape and size of the excavation (secondary stress) and the relative orientation of discontinuities to the tunnel axis.

As stated in the introduction, the main focus of this work is the ground behavior of rock masses influenced by discontinuities. The ground behavior constitutes a fundamental element in order to evaluate failure mechanisms and correctly assess

support requirements. The following paragraphs summarize the influencing factors which effect layered rock masses.

2.2.1. In-situ stress

A complete summary on the components and influencing factors for the in-situ stress is presented by Amadei & Stephansson in [26]. The authors divided the in-situ stresses into four different categories: gravitational stress, residual stress due to metamorphism, residual stress and terrestrial stress.

A common assumption is that the in-situ stress has a vertical component $\sigma_v = \gamma \cdot g \cdot h$, governed by the density (γ) and magnitude of the overburden (h), and a horizontal component $\sigma_h = \sigma_v \cdot K_0$, as a function of the vertical component (σ_v) and a lateral pressure coefficient (K_0).

After Goodman [27], in terms of principal stresses σ_1 and σ_3 , the intact rock strength is equal to:

$$\sigma_1 - \sigma_3 = UCS + \sigma_3 \left[\tan^2 \left(\frac{\pi}{4} + \frac{\varphi}{2} \right) - 1 \right] \quad \text{Eqn. 1}$$

Where UCS is the unconfined compressive strength () defined by an internal cohesion c_0 and the internal friction angle φ .

$$UCS = 2c_0 \cdot \tan \left[\frac{\pi}{4} + \frac{\varphi}{2} \right] \quad \text{Eqn. 2}$$

The joint shear strength is defined by a Coulomb criterion with zero cohesion and a joint friction angle φ_j and is equal to:

$$\sigma_1 = \sigma_3 \cdot \frac{\tan(\alpha + \varphi_j)}{\tan \alpha} \quad \text{Eqn. 3}$$

Eqn. 1 and Eqn. 3 have been plotted in the right diagram shown in Fig. 2. The figure displays the variation of the intact rock strength depending on the weakness plane orientation α , slip along the weakness plane takes place, before the intact rock strength is mobilized, for α values close to $45^\circ + \varphi/2$.

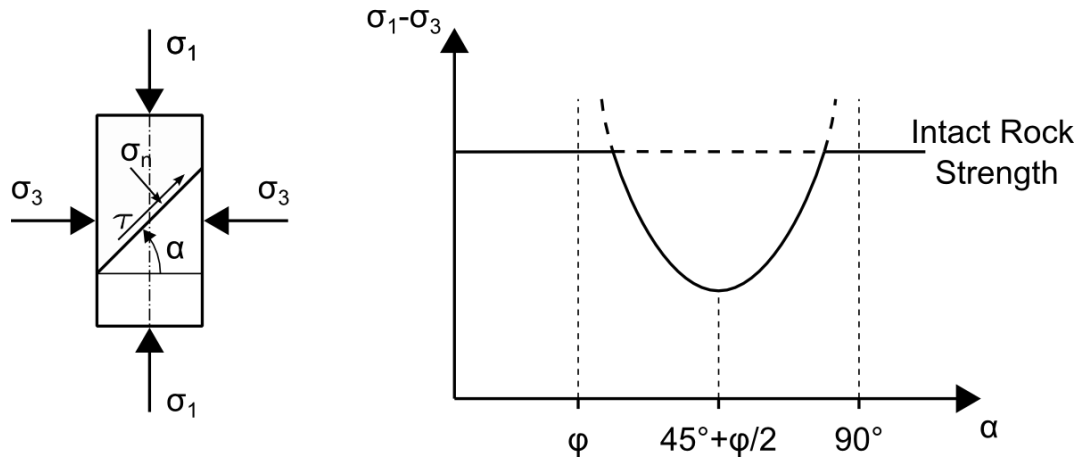


Fig. 2: Influence of a discontinuity on the intact rock strength

Under the conditions displayed in Fig. 2, it is possible to decrease the possible domain of the lateral pressure coefficient K_0 as follows:

$$k_{\min} = \frac{\tan \alpha}{\tan(\alpha + \varphi_j)} \quad \text{Eqn. 4}$$

$$k_{\max} = \frac{\tan(\alpha + \varphi_j)}{\tan \alpha} \quad \text{Eqn. 5}$$

Weakness planes, caused by discontinuities, have mainly two effects on the rock mass. Firstly, the shear strength is reduced and secondly, the tensile strength could reach values close to zero.

Authors have stated that the discontinuity pattern (e.g. number of sets, spacing, orientation, etc.) and its strength and deformation properties are related to the in-situ stress field [26], [28]. Taking this into account it is possible to further decrease the range of lateral pressure coefficient based on the discontinuity features.

It is important to highlight that Eqn. 3 applies for an axisymmetric and compressive strength. The redistribution of in-situ stresses around the excavation in most cases is not axisymmetric resulting in complex conditions, difficult to define with closed form solutions.

2.2.2. Size and shape of the excavation

The size and shape of the excavation influence the redistribution of stresses which is defined as a variation of the in-situ stress state due to an artificial intervention, e.g. caverns, tunnels, hollow cavities, etc. Disturbance on the stress conditions

induced by an excavation can exceed the strength of the rock mass leading to failure of the rock adjacent to the excavations boundary.

Closed form solutions for limited shapes and numerical methods are the two main approaches applied in order to calculate the stress magnitude around an excavation. Field methods such as hydraulic methods, relief methods, jacking methods, strain recovery methods and borehole breakout methods, are also used for measuring stress redistribution around an opening.

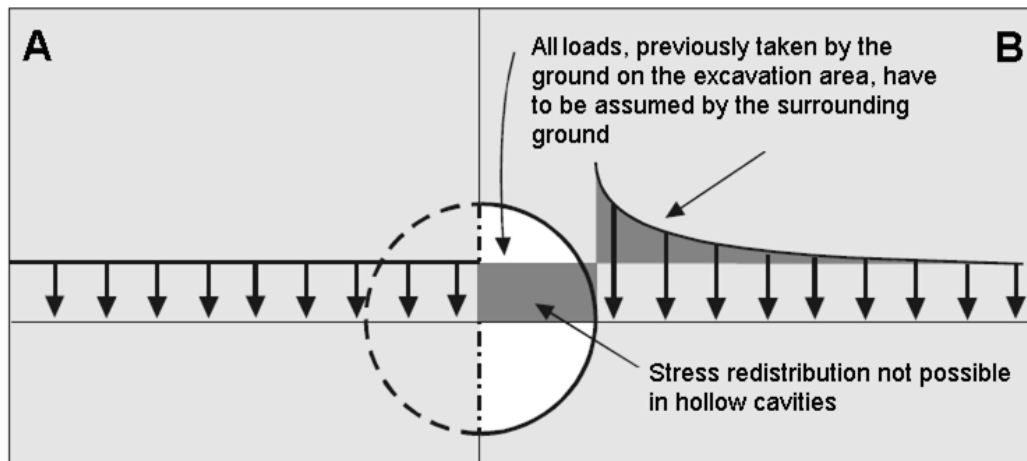


Fig. 3: Stress distribution on an elastic material A) In-situ stress B) Stress redistribution after excavation

Closed formed solutions have been developed for shapes such as circular and elliptical shape, among others [29], [30], [31], [32], [33]. Multiple authors have complemented or extended the basic analytical solutions to include a weakness plane, Bandy & Brown [34] merged a single discontinuity into Kirsch's basic solutions [32]. However the solutions presented by the authors have limited applicability since the location of the discontinuity has to be known and cross section shape and boundary restrictions exist.

Bandy & Brown [34] state that elastic closed form solutions deliver useful information on boundary stress for simplified geometries and even the inclusion of weakness planes is possible. Such solutions, at the same time, could be extrapolated in order to achieve fair approximation on the stress states for other similar shapes. However, as the authors stated, to determine the stress distribution around an opening in layered rock masses, a computational method of stress analysis would be necessary. Size and shape of the excavation are related to the zone of influence and stress redistribution.

The zone of influence is defined as the domain of significant disturbance from the initial in-situ stress. It is important to note that, in general, the zone of influence of an opening is related to excavation shape, size and in-situ stress.

A relative common mistake is to relate the size of an excavation with the stress magnitude. Stresses at the boundary of an excavation are independent of the excavated area. However, it is fundamental to keep in mind that the size of the excavations has a clear influence on the displacement magnitude and behavior of

the excavation as well as its stability, bearing in mind that the rock mass is not perfectly elastic and it is not completely free of discontinuities (homogeneous). Even if stresses are the same, the stability of the excavation in a fractured and jointed rock mass will be controlled, partially, by the ratio of the excavation size to the joint persistence/frequency. Consequently increasing the excavation size in a typical jointed rock mass may not cause an increase in stress, yet a significant influence on the stability [35].

For shapes other than circular the new distribution of stresses leads to anisotropic stress conditions. In order to estimate stresses around a hollow cavity, most analytical solutions are truncated by shape limitation.

Considering that the rock mass is not a linear elastic material, redistribution of stresses generates “plastic” zones which could be determined by numeric solutions. Raji & Sithram [36] carried out a research dealing with plastic radii and stress distribution around an opening using an elasto-plastic Mohr Coulomb medium. By means of a finite difference based software, the authors vary the lateral pressure coefficient (K_0) for different shapes, as conclusion the researchers stated that shape and lateral earth pressure ratio has no significant influence on the plastic zone created.

2.2.3. Relative orientation of geological structures (discontinuities)

It is well known that the relative orientation between tunnel axis and discontinuity orientation can have a significant influence on the displacement characteristics, including magnitude, orientation and potential failure mode.

Based on this fact, tunnel engineers have collected empirical data and summarized it into guidelines and rock mass classifications. However, there is limited information on how to incorporate such knowledge on jointed rock masses into the design or as a tool for proper interpretation during construction.

Most guidelines [37] and rock mass classifications [38] systems include qualitative diagrams, describing the influence of the discontinuities in terms of “favorable” and “unfavorable” conditions to the excavation stability. Classification systems simplify the rock mass into an equivalent continuum unable to represent displacement patterns and failure modes influenced by discontinuities.

Fig. 4 displays the favorability of the relative orientation of the discontinuities with respect to the tunnel axis. The favorability is given by the location, on a stereographic projection, of the plane’s pole considering a fixed orientation (S-N) of tunneling. Simplification such as the one presented the figure has to be used carefully taken into consideration that, the term “excavation stability” is not linked to the other factors which govern the failure mechanism and it could be misleading and erroneous to assume instability only based on the relative direction of the discontinuities (e.g. DD090Dip90 would be an unfavorable situation for the side-wall stability yet, at the same time, a favorable condition for the stability of the face during excavations). This simple example sets a precedent on the importance of considering all influencing factors in order to properly assess failure mechanisms.

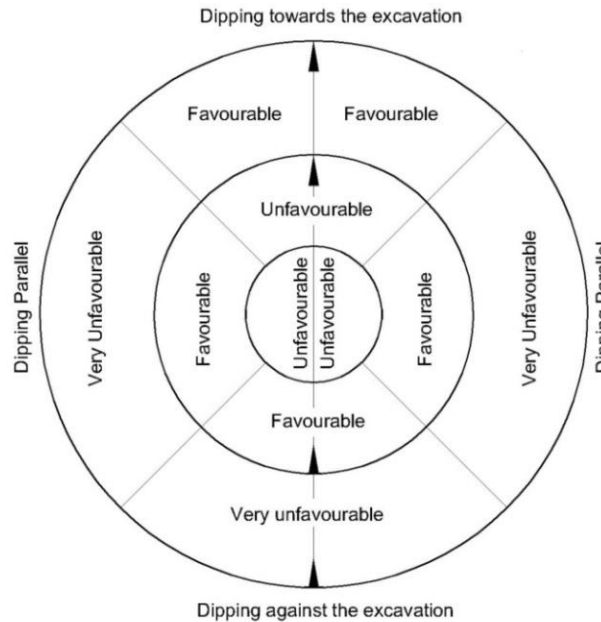


Fig. 4: Discontinuity orientation favorability estimate [37]

Physical models constitute a useful tool to evaluate failure mechanisms of jointed rock masses. The research carried out by Vardar [39] used a test model comparing homogeneous and jointed models. His research had some important findings for the present work, including:

- When the main joint set direction is normal or parallel to the primary stress, stress trajectories are similar to the homogeneous-isotropic (monolithic) model results.
- For Non-hydrostatic stress fields ($K_0 \neq 1$) the general displacement magnitude is higher than for a hydrostatic stress field.
- For the same stress field conditions, bending occurs on one side of the opening and sliding take place on the opposite side when the dip angle of the joint set is larger than the joint friction angle (φ). This conclusion implies that the failure mechanism is governed by the weakness planes rather than the intact rock.
- A second joint set causes an extension of the over stressed area.

By means of a base friction model Goricki [40], studied the ground behavior influenced by different cross sections, overburden, joint spacing and joint orientation for jointed rock masses. Important conclusions from Goricki's research for the present work are:

- If the dip angle is lower than the joint friction angle (φ), a flexural failure with an elliptical form takes place.
- For dip angles higher than the joint friction angle (φ), the failure will be governed by the tensile and shear strength.

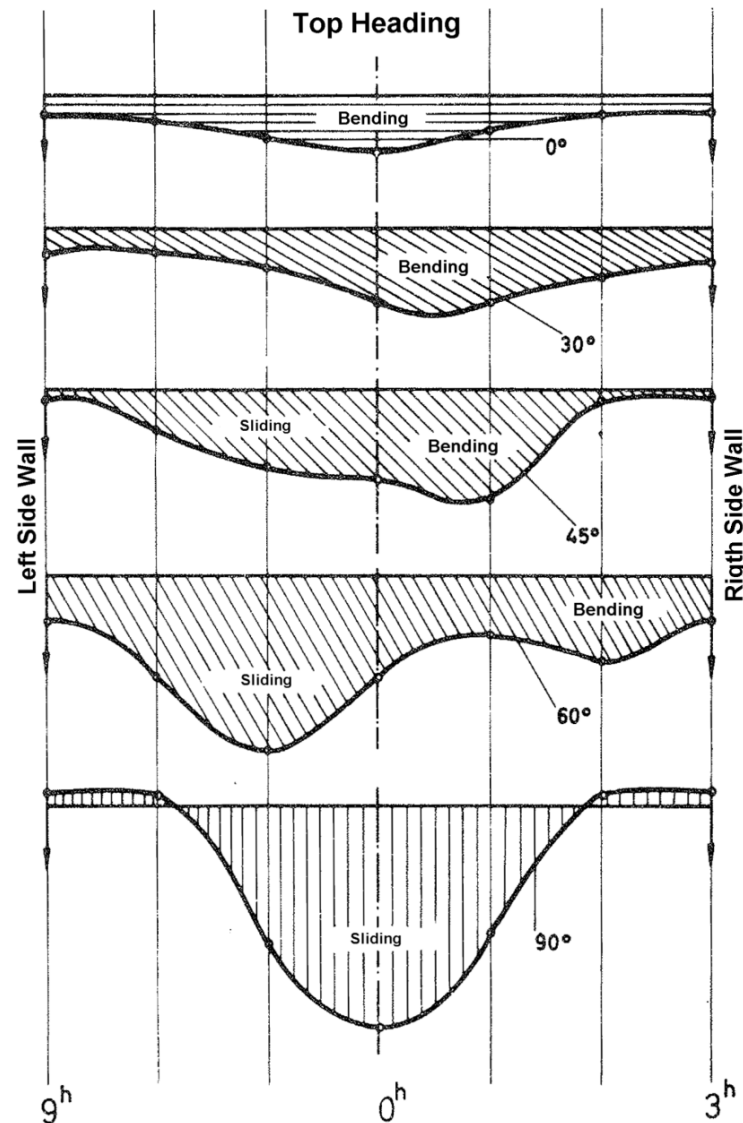


Fig. 5: Ground behavior (bending/sliding) for multiple dip angles after Vardar [39]

Vardar and Goricki's conclusions constitute a useful bench mark for the numerical model validation presented in this research. A proper validation of the numerical model should be carried out in order to assess its capability to simulate real conditions. An additional useful conclusion from the authors is the need of discrete approaches if complete detachment, large displacements and block sliding and rotation are expected to take place.

2.2.4. Geotechnical model

A key element throughout an underground project is the so-called geotechnical model which discloses the most relevant tunnel engineering parameters regarding features such as overburden, stresses distribution, rock type, rock mass and joint properties, hydrogeological conditions, faults length and magnitude, etc. [41], such features have a direct influence on the ground and displacement behavior.

During the design stage, the model allows tunnel engineers to predict potential failure mechanisms, characteristic displacements and design support systems accordingly. During construction, the monitored displacements shall be used to update the geotechnical model. It should be kept in mind that changes in the displacement characteristics (magnitude and orientation) can indicate changing ground conditions ahead of the face [42], [43], [44]. Additionally, the assessment and interpretation of displacement characteristics is based on the expected “normal behavior”. The determination of the normal behavior is one of the main aims of the present work given by the designer.

The model is assembled through multiple sources of data e.g. existing literature, field survey, surface and subsurface exploration and in-situ and laboratory testing among others. Throughout the model assembling, participation of multiple engineering disciplines is needed to achieve an appropriate model. An illustrative example is shown in Fig. 6. The figure firstly shows different components of a geotechnical model and, secondly, displays the direct dependence between the geotechnical model, an appropriate ground behavior assessment and a subsequent system behavior.

Although model assembling takes place at the design phase, continuous update throughout the different stages of the project is needed in order to cover and reduce uncertainties that necessarily arise due to limited time, financial resources for investigations and limited sampling; especially in subsurface explorations and laboratory testing, data are acquired only point wise [45]. Proper tools for displacement interpretation, in connection with the ground features (e.g. discontinuities, weakness planes, faulted material, etc.), is needed for this purpose.

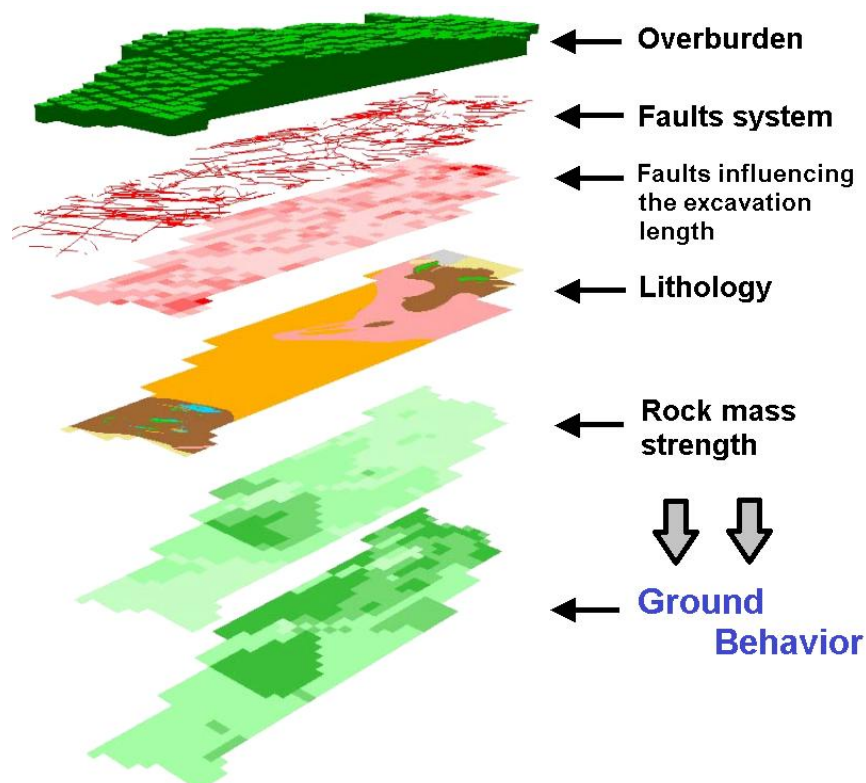


Fig. 6: Geotechnical model engineering parameters [46]

2.3. Modeling Methods

Multiple modeling methods can be found in the literature, a complete revision of the available numerical modeling techniques for rock mechanics and rock engineering is presented by Jing & Hudson [47]. The authors highlight the importance of modeling, advantages and disadvantages of multiple methods and made an analysis on how, through numerical methods, it is possible to study the fundamental processes occurring in the rock mass, in order to anticipate the performance of structures built in the rock mass.

Fig. 7 summarizes the different techniques into eight different modeling or design methods placed in the main central box, based on the four main modeling methods and 2 different levels; level 1 includes methods in which there is an attempt to achieve one-to-one models and level 2 are the methods which are not totally direct e.g. rock mass classifications.

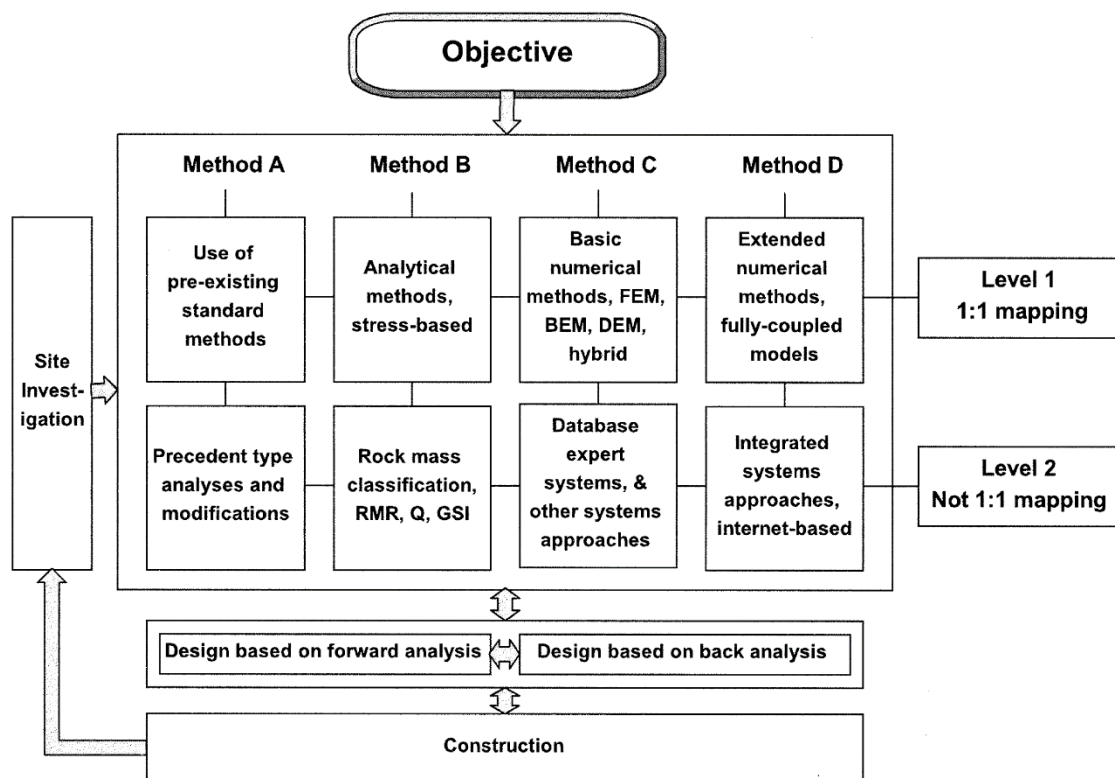


Fig. 7: Methods for rock mechanics modeling [47]

2.3.1. Simplified models

Simplified models include closed form or analytical solutions which are based on simplified geometries and/or restrictive boundary conditions and, in most cases, empirically based rock mass classification. This section centers on different approaches that include jointed materials into the models.

2.3.1.1. Rock mass classification

One of the first references found in literature to a rock mass classification, considering the presence or discontinuities, is made by Rziha [48]. The author's classification focuses on support requirements and excavation sequence depending on the cross section and geological situation.

Fig. 8 is presented as an example of the author's work; the figure displays an implicit understanding of the ground behavior and influence of discontinuities on the stability of the excavation. Selection of support requirements and excavation sequences is made based on the possibility of kinematic movement of "single components in the ground" (layers).

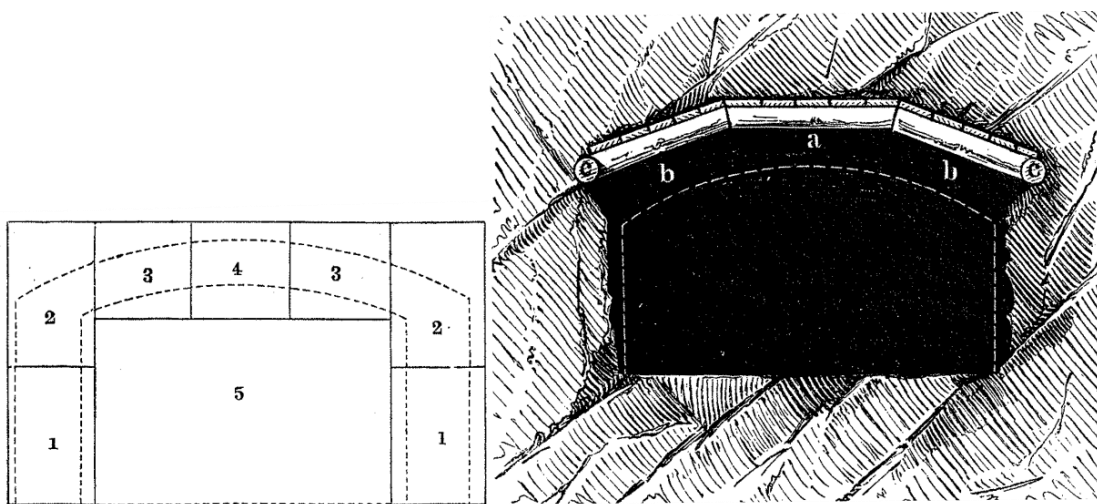


Fig. 8: Excavation sequence and support system after Rziha [48]

Terzaghi in 1946 presented a classification diagram which includes steel support requirements for "moderate jointed rocks" [49]. The failure mechanism for jointed rocks is described as spalling and a vague reference is made on the influence of discontinuity orientation. According to the author higher side pressure is to be expected and subsequent additional support is recommended, if joints are "inclined". However, no details are given on the inclination value or the increment of side pressure.

Stini introduced a qualitative classification based on rock load and behavior during excavation [50]. It is worth highlighting the introduction of the so called "joint index" which, according to Stini's classification, has a negative effect on the excavation rate, resulting in higher support requirements.

Classification systems, still in use, include Coates' [51] which qualitatively include the influence of discontinuities on the excavation stability. The author proposed different support requirements for blocky and layered rock masses. Wickham et al. [52] gathered experience from multiple tunnels and developed the Rock Structure Rating (RSR), an empirical quasi-quantitative classification system which quantifies the influence of discontinuities through the so called "B Parameter". The parameter displays an important feature as it relates the effect of discontinuity pattern with respect to the direction of the tunnel drive.

The influence of discontinuities is quantified in the RSR depending on joint spacing, strike to axis (parallel or perpendicular), dip (flat, dipping or vertical) and direction of excavation. The “B parameter” considerably decreases for joint spacing below 30cm, implying higher support requirements. However, there is neither reference nor inclusion of joint properties into the quantification.

The Q system proposed by Barton et al. [53] was developed as an empirical approach based on the analysis of, allegedly, more than 200 case histories in Scandinavia. The system quantifies the joint effect based on number of sets and roughness/alteration of the discontinuity, however there is no consideration of discontinuities orientation.

Bieniawski [54] presented an engineering classification for jointed rock masses which forms part of the Rock Mass Rating (RMR) [55], published in 1976. The author suggests an adjustment to the rating depending on the orientation of the discontinuities, decreasing the final RMR value by 0 to 12 points (maximum RMR value = 100) depending on the “favorability” of the orientation with respect to the excavation direction (based on Wickham et al. [52]).

The Rock Mass Index Rmi proposed by Palmström [56], embedded the discontinuities into the classification through properties such as roughness, alteration and continuity of the joints. A further development from the Rmi involving support estimates was presented by the author in 2000 [57]. In the publication Palmström includes the so called “rock support adjustment factors” involving the orientation of the joints and its effect on the roof and wall stability separately.

	Joint Orientation		Joint Strength	
	Factor	Rating	Factor	Rating
RSR	B parameter	9 to 40	No consideration	
RMR	Adjustment of Joint orientation	0 to -12	Condition of Joints: Roughness, separation, filling	0 to 30
Q system	No Consideration		Joint Roughness Joint Alteration	Jr/Ja
Rmi	Orientation adjustment factors*		Joint Parameter: Roughness, Alteration, continuity	JP

* Only included for support estimation, not in the basic classification

Table 1: Discontinuities consideration in rock mass classification systems

Rock mass classifications have been widely used for support estimation. Although there is a clear influence of discontinuities on the rock behavior, and therefore on the required support, classification systems make a rather qualitative inclusion of the effect and propose support requirements accordingly. However, classifications are unable to accurately display the effect of discontinuities on the failure mechanism, mainly due to their empirical nature and the loss of important information due to simplifications made in the classification procedure.

2.3.1.2. Analytical methods

The method (Method B, level 1 in Fig. 7) consists on simplifying a problem into analytical equations, also known as closed-form expressions [58]. Such expressions have successfully been applied for the following tunneling problems:

- evaluation of stresses and strains around an excavation for simple geometries,
- determination of the extent and distribution of stresses within plastic zones. For circular/elliptical openings under axisymmetric and also for anisotropic stress field and conditions,
- support can be modeled only by applying internal pressure and/or modification of rock mass parameters [59] and
- quick parametric studies.

Although this method is widely used, analytical solutions are subject to multiple assumptions and simplification, especially concerning geometry aspects and boundary condition, leading to simplification on the assessment of the ground behavior. Consequently, the result delivered by closed form solutions are difficult to extrapolate to field conditions and considerable experience is required for meaningful application of the results.

Closed form solutions involving discontinuities are not common to find in literature. Section 2.2.2 addressed some of the approaches, it is worth highlighting the summary presented by Brady & Brown [34] with the mathematical handling of “planes of weakness” and its effect on stress distribution; the authors determined the possibility of separation and slip of the joint based on the Kirsch equation, the inclination of the plane and the lateral pressure coefficient ($K_0 = \sigma_h/\sigma_v$).

The approach presented by Brady & Brown offers a practical guideline for the type of analysis to be carried out. If slip and/or separation is expected, a continuum approach should only be used if the zones of “inelastic response” (plastic zone) is small in relation to the excavation area. The last statement has special relevance on this study as the ubiquitous joint model delivers proper results as long as no separation between the layers takes place (section 2.3.2).

Closed form solutions are able to deliver a good approximation on the rock mass behavior, limited to idealized interface problems. However, the complexity of the structures (non-axisymmetric), materials behavior and of boundary conditions (non-hydrostatic in-situ stress conditions) among other reason, have progressively led to the predominance of numerical models.

2.3.2. Numerical methods

This section focuses on the available numerical methods for jointed rocks simulations (Method C, level 1 in Fig. 7). The figure summarizes the most commonly applied numerical methods in rock mechanics including: continuum methods, discrete methods and hybrid methods.

The choice of an appropriate method depends on the specific project, expected behavior of the ground and system, and mainly on the fracture system geometry. The continuum approach is limited for problems where fracture opening and block detachment is not a significant factor [47]. However, if the mentioned factors play an important role in the ground behavior, a discrete approach is more suitable to deliver realistic results at higher computational costs. The so called “hybrid” methods were developed to avoid some of the disadvantages by combining continuum-discrete models.

Discrete systems are commonly referred to as Discrete Element Method (DEM) which includes all numerical methods handling the problems domain as an assemblage of independent units. The method is mainly applied for problems involving fractured rock and granular media, in which the analysis is based on the contacts between individual members (block/particles) [60]. The theoretical basis of the method is the formulation and solution of motion for rigid/deformable bodies and rotation motion equations.

Shen & Barton in [61] studied the disturbed zone around tunnels in jointed rock masses, a brief reference is made on the influence of different joint orientation on the disturbed zones around an opening. Using the 2D DEM explicit computational code UDEC the authors vary the dip angle and encounter that for a friction angle ϕ equal to 35° the largest shear zone is developed for joints dipping 60° , in agreement with the Mohr-Coulomb strength criteria for which the analytical solution yields the weakest plane dipping 62.5° .

Goricki et al. studied the relative orientation of the discontinuities to the tunnel axis in [1] and compared monitored data with the numerical results obtained from discrete simulation (UDEC). From the discrete analysis the authors highlight that the largest displacements occur normal to the joint strike and shear tends to occur in the vicinity of the excavation perimeter where the discontinuities intersect the excavated area in an acute angle. The result from the numerical model showed a good agreement with displacement data coming from the Strengen tunnel in western Austria. The 2D nature of the analysis was not able to capture the displacement development as the distance to the tunnel face increases.

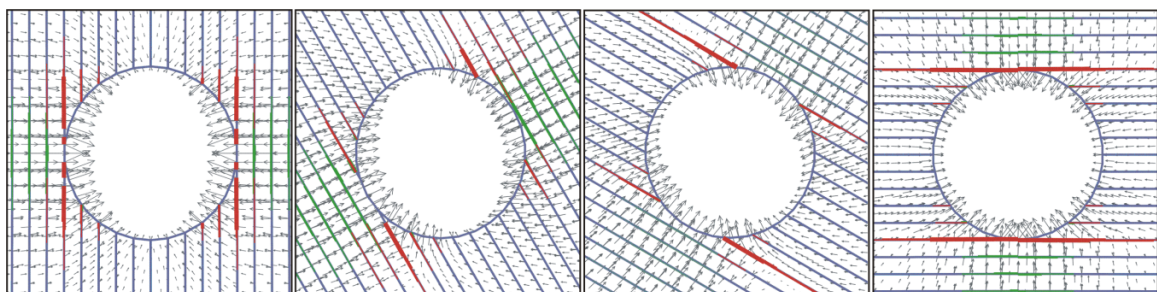


Fig. 9: UDEC simulation results, joint dip 90° , 60° , 30° , 00° . [1]

In a second stage the researchers implemented a continuum 3D analysis with the ubiquitous joint model from FLAC 3D (Itasca consulting group). The continuum 3D simulation was aimed to assess the development of displacements behind the face (pre-displacements). The results showed that for DD090/90 (discontinuities

parallel to the tunnel axis) a high percentage of displacements takes place behind the face in comparison to DD000/90 (discontinuities perpendicular to the tunnel axis).

A similar approach was made by Button et al. [62] who gathered the experiences of tunnels in Austria constructed in foliated rocks over the last years. The researchers made a complete identification of the basic characteristic behavior of tunnels excavated in such rock masses, mainly based on monitored data. Their study was complemented by a 2D discrete numerical model (UDEC) and continuum 3D model (Flac3D). Their study shows that as the rock mass quality decreases (the presence of a secondary structure is not considered), the characteristic displacement pattern remains similar, however, there is a variation on the displacement magnitude. The researchers established that a continuum approach is able to capture trends observed for jointed rock mass structures; however the model is not suitable for the study of more complex rock mass geometries.



Fig. 10: Foliated rocks mass _ Button et al. [62]

Literature provides numerous comparisons between continuum and discrete approaches, an example of these comparisons can be found in the work from Ferrero et al. [63]. The authors presented as a conclusion of their work that the continuum models underestimate plastic areas, however the comparison is only valid for the specific boundary conditions and the materials properties presented in the publication.

Goricki et al. [1] and Button et al. [62] made use of a continuum approach in their research. This approach is perhaps the most frequently applied numerical method in engineering fields. Continuum computational software implements numerical

techniques such as Finite Difference Method (FDM) or Finite Element Method (FEM). The approach is to approximate the solution of Partial Differential Equations (PDEs) by discretizing the spatial dimension to convert the PDEs into Ordinary Differential Equation (ODEs) [64].

The FDM presents the most direct and intuitive technique for the solution of PDEs. Unlike FEM, in FDM there is no need for a global system of equation in matrix form and no interpolation to approximate the PDE in the neighbor points is needed [47].

The standard FDM was suitable only for simplified rock mechanic problems, due to its inflexibility in dealing with fractures and complex boundary conditions (mesh geometry). However, the inclusion of finite volume technics (FVM) allow the conventional FDM to deal with irregular and complex geometries, making it as flexible as FEM. Explicit representation of fractures cannot be performed in the standard FED/FVM due to the fact that there is need for continuity of the function in the neighboring grid points. Nevertheless it has been shown that the techniques included in FDM could be successfully implemented to study failure mechanisms.

The FEM is the most widely used numerical method in engineering fields. Since its origin in the early 1960s the method has been oriented to solve rock mechanics problems because it presented the first numerical method with enough flexibility for complex geometries, material heterogeneity and non-linear deformability among other advantages.

The behavior of jointed rock masses is simulated in continuum models (FDM and FEM) mainly by implementing three different techniques: by including joint/interface elements, by including anisotropy into the stress conditions and by modifying rock mass properties [65]. The anisotropic stress conditions depend on the orientation of the isotropy plane. Anisotropic rock mass properties are considered according to the orientation of the isotropy plane where there is only one joint set.

One of the first applications towards simulation of fractures was presented by Goodman [27]. The author introduced the "Goodman joint element" which was implemented in multiple FEM codes for constitutive models. However, the zero thickness of the Goodman joint element caused "numerical ill-conditions" due to the large ratio length/thickness [47]. In addition to the computational problems the Goodman's edge-to-edge approach is unable to represent complex failure mechanisms [66].

The mentioned shortcomings of Goodman's approach led to the development of new approaches in order for FEM to simulate cracks and discontinuities. A summary of FEM approaches is presented by Tzamtzis in [67] including:

- *The discrete approach*: unlike Goodman's edge-to-edge contact approach, the cracks are represented as separate nodes requiring great computational effort as continuous update of the global finite element mesh is needed, the updating takes place as the stress or strain at the node exceeds a stress or strain threshold value.

- *Smear crack approach*: joints are modeled by modifying the material properties at certain integration points of a regular finite element. Yielding criterion is based on conservation of strain energy (strain energy released).
- *Interface smear crack approach*: Discontinuities are limited to element boundary, if the crack opening criterion is reached at the boundary, local element displacement is modified until stresses perpendicular to the interface are brought as close as possible to zero.

Witke [68] implemented a basic continuum equivalent approach to study the effect of anisotropy due to weakness planes in an opening (approximately 75m²) under 50m overburden. The study was conducted for the following cases A. DD000/Dip00, B. DD090Dip90, C. DD090Dip60 and D. DD000/Dip90. The cases are summarized in Fig. 11.

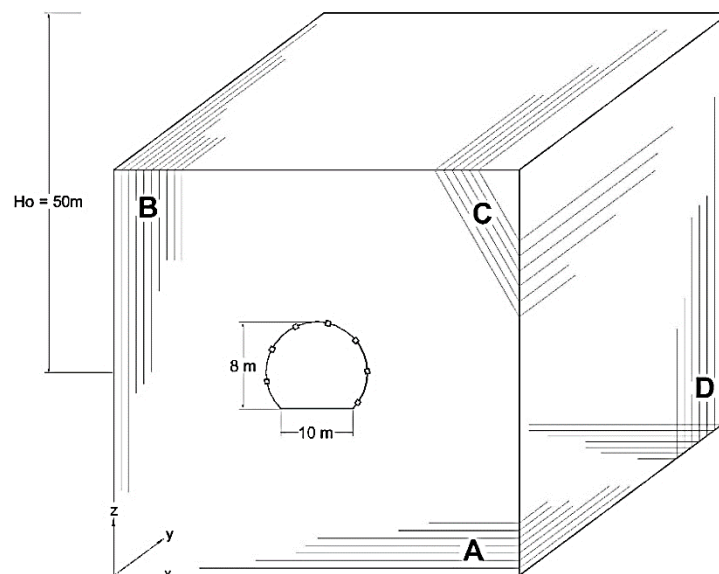


Fig. 11: Cases studied by Witke [68]

Some of the conclusions delivered by Witke's research are presented in Fig. 12. Normal and shear stresses in a section parallel to the schistosity are shown on the left side of the figure representing the direction in which the shear and tensile strength is reduced. The combination of a high shear stress with low normal stress represents an unfavorable situation; the described situation is met above and immediately below the tunnel for case A (DD000 Dip00). The same situation, in a larger area, was registered for case B (DD090Dip90), where the affected area also extends to the side-wall. For case B it is also important to note that the areas of tensile stress occur above the roof and beneath the invert. Regarding case C (DD090Dip60) shear stress concentrations are found along the schistosity leading to tensile stress perpendicular to the weakness plane orientation.

The influence of a weakness plane on the opening deformation is identified in Fig. 12. On the one hand, it is evident that for case C (inclined plane) the deformation is asymmetric and on the other hand the largest roof settlement occurs for case A.

It is worth mentioning that the last conclusion is highly dependent on boundary condition (stress conditions) and joints and rock mass properties.

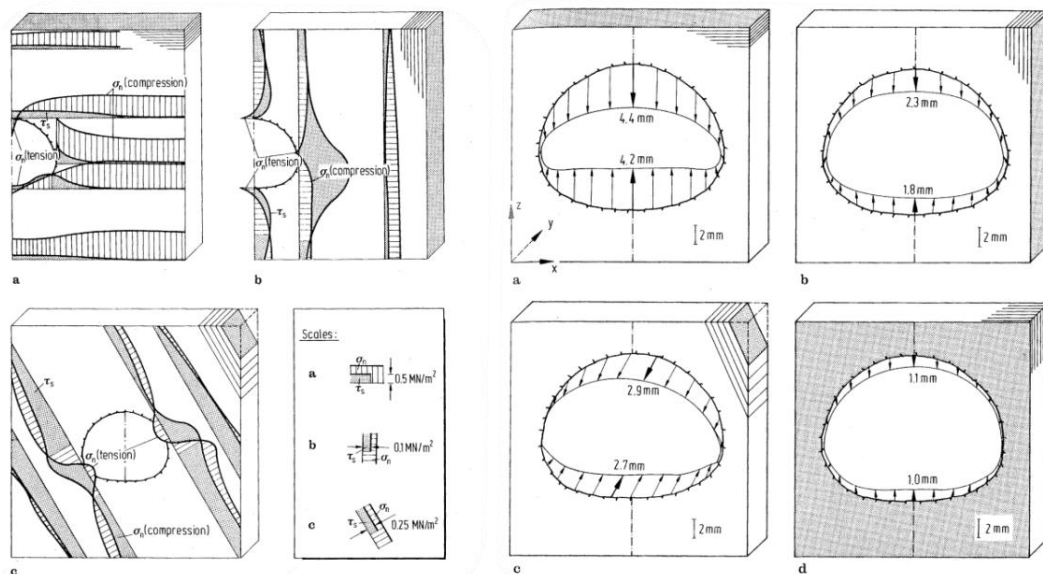


Fig. 12: Shear and normal stress parallel to the schistosity (left) and deformation of the opening (right), after Wittke [68]

Hammah et al. [69] studied the distribution of principal stresses around a circular opening with different diameters (1m, 5m and 10m) taking into consideration a constant initial principal stress. Using a FE continuum model and representing discontinuities through interface joint elements, the researchers concluded that the presence of joints reduced the mean major principal stress and that the distribution of stress was independent of the size of the excavation. This is one of the main weaknesses of continuum-based theories, since by constant stress environments the stability of an excavation is independent of opening size. In reality this is not the case due to the stress redistribution effect caused by the discontinuities.

The displacement development in multiple tunnels in Slovenia was studied by Klopčič [70]. His research was carried out in different geological and geotechnical conditions including foliated rock masses. With the help of 2D and 3D FEM numerical simulations, the author was able to identify the influence of the discontinuities orientation on pre-displacements (displacement ahead of the face). The author concludes that the displacement portion developing ahead of the excavation is lower for tunneling against dipping orientation, which presents a more unfavorable situation as a higher load is transferred to the tunnel support. This pattern remains independent of rock mass and discontinuity properties. Although the displacement magnitude was not well predicted by the numerical model in Klopčič's study, displacement characteristics well fitted the monitored data.

As previously addressed, FDM is not able to explicitly include fractures since continuity of the function in the neighboring grid points has to be maintained. An alternative approach is the inclusion of an orientation of weakness into a continuum, generally called ubiquitous joint. The ubiquitous approach is the one

used in the present work to study and analyze displacement behavior in jointed rock masses. The approach to some extent is suitable for foliated rock masses, shear planes and for constant joint parameters between discontinuities. It has a clear advantage against discrete models since the computational effort needed for calculation is drastically reduced; however there are shortcomings that have to be taken into account to validate the results of the model.

In the ubiquitous model, planes remain “unnoticed” until the shear stress acting exceeds the strength [71]. Therefore, unlike other constitutive models, anisotropy is not included in the calculation of initial stresses (isotropic elastic constitutive law), thus only the plastic deformation contributes to the anisotropic behavior. Goricki et al. [1] state that the failure mechanisms would be controlled by the discontinuities (weakness planes) rather than by the intact rock, a statement complemented by Singh et al. in [72] who describes displacements in jointed rocks as highly anisotropic not due to the rock anisotropy but rather to the anisotropy induced by the discontinuities itself.

Probably the main drawback of the ubiquitous joint approach is the inclusion of only one shear component in the calculation leading to displacements overestimation as the bending component is reduced to zero if the shear strength limit is reached [2] (Fig. 13). Therefore results have to be filtered based on the shear stress acting on the ubiquitous joints, a process that can be included in the implementation code of the numerical software.

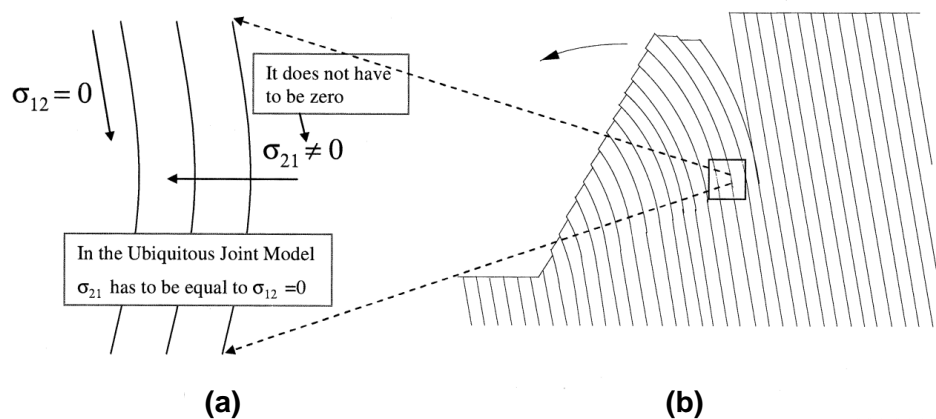


Fig. 13: Schematic showing (a) erroneous shear that may arise in the ubiquitous joint model and (b) flexural toppling failure [2]

2.4. Monitoring Data Evaluation

Some of the available tools to help the assessment of the ground behavior (Fig. 1) were reviewed. The study of the behavior constitutes the main goal of the present work, however, there is an inherent application during construction, taking into account that the ground behavior is the basis for determining the excavation and support systems and it assists in evaluating and interpreting of monitored data during construction [73].

Independent of the construction method a well-defined monitoring program shall be implemented in order to conduct a safe and economical underground project [74]. Through displacement monitoring site engineers are able to evaluate the system behavior and assure stability.

Improved techniques such as the usage of total stations and reflective targets have replaced relative measurement methods used for the past four decades. New techniques [75] permit the usage of data visualization tools such as deflection curve diagrams, trend lines and vector plots (Fig. 14), complementing the traditional evaluation/visualization methods like Time-Displacement curves [76].

3D monitoring (global coordinates) present a clear advantage when comparing with conventional relative tape measurements or extensometer measurements. It allows independent (point by point) displacement monitoring along the cross section, being a requirement in order to observe anisotropic displacement exhibited by jointed rock masses [72]. Such behavior cannot be displayed through traditional relative displacement monitoring.

Different segments of the cross section will yield different orientations and magnitudes of displacements [76]. The described effect becomes predominant for jointed rock masses due to the fact that displacements (displacement pattern - magnitude) are strongly related to the structures' relative orientation to the tunnel axis.

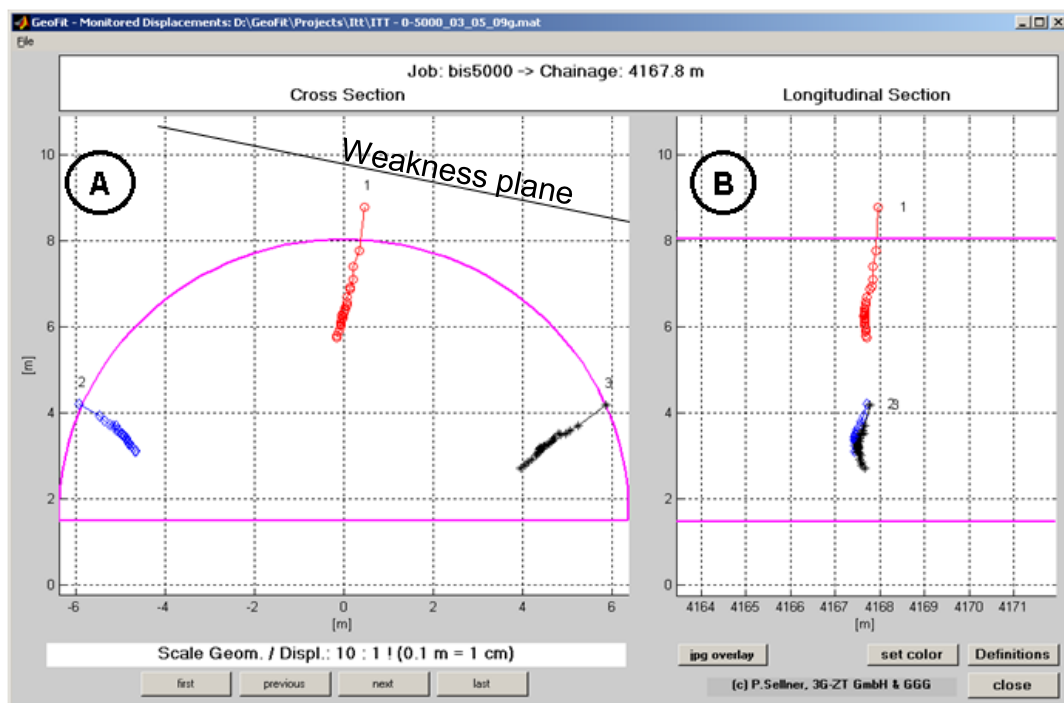


Fig. 14: Displacement vector plot a) cross section (b) longitudinal section. Geofit®

Tunnel monitoring systems involve measurement of displacements, surface settlements, vibration, hydraulic conditions, temperature and lining strains among others. This work will mainly focus on displacement monitoring. Two approaches are implemented to identify the behavior characteristics of a cross section, firstly

by using displacement vectors complemented by overlaid geological conditions and secondly by monitoring displacement development vectors with time and face position [62].

Displacement measurements constitute a convenient tool to validate numerical models as seen in [1], [12], [18], [62] and [70]. Reasonable fitting when comparing monitored displacements to numerical results is a reliable benchmark to validate, not only the numerical model itself but also the geotechnical model assembled to frame the conditions influencing the underground structure. The geotechnical model has to be constantly evaluated and adjusted if initial assumptions do not fulfill the observed behavior. For the specific case of jointed rock masses design assumption of joint properties and, up to a certain extent, relative orientation of discontinuities exhibit a rather high degree of uncertainty that can only be reduced during construction [77] [78] through correct implementation of the monitoring program and a proper data interpretation.

3. FLAC3D NUMERICAL MODEL

The Flac3D ubiquitous joint model accounts for the presence of an orientation of weakness (weak plane set) in a Mohr Coulomb based model. The failure criterion on the weakness orientation consists of a composite Mohr Coulomb envelope with tension cut off [79] in combination with the given plane orientation. The ubiquitous numerical model firstly inspects the general failure based on a standard Mohr Coulomb failure criterion (no ubiquitous plane is included), relevant plastic corrections are applied and a failure analysis, induced by the new/corrected stresses ($\sigma_{3'3'}$), on the weakness plane (weakness plane) is performed. Fig. 15 exhibits the weak plane failure criterion for the ubiquitous medium in Flac3D, the failure envelope is defined between points A-B by the Mohr Coulomb failure criterion described by the following expression:

$$f^s = \tau + \sigma_{3'3'} \cdot \tan\phi_j - c_j \quad \text{Eqn. 6}$$

The segment BC is defined by the tension cutoff expressed by

$$f^t = \sigma_{3'3'} - \sigma_j^t = 0, \quad \text{Eqn. 7}$$

where ϕ_j , c_j and σ_j^t is the friction, cohesion and tensile strength of the weakness plane respectively.

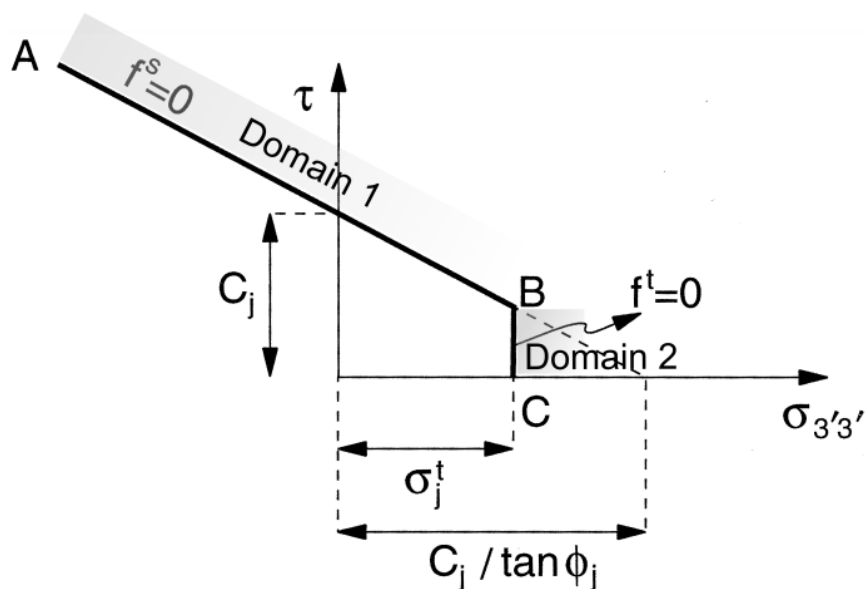


Fig. 15: Flac3D weakness plane failure criterion [79]

The maximum value of the tensile strength is given by the following expression:

$$\sigma_{jmax}^t = \frac{c_j}{\tan\varphi_j} \quad \text{Eqn. 8}$$

Any stress point could be described in the $\sigma_3'_{3'} vs \tau$ plane. Shear failure takes place if the stress point is placed on the curve $f^s = 0$ (domain 1). Tensile failure takes place in domain 2 and the stress point would be located on the $f^t = 0$ curve. Failure detection is followed by the needed plastic correction before starting a new calculation.

There are several advantages from the constitutive model including easy implementation and low computational effort. Disadvantages are that slip and separation along a plane cannot be measured, only one set of discontinuities (weakness plane) can be simulated and that only one shear component is included in the model, neglecting the bending rigidity [80] (see section 2.3.2).

3.1. Numerical Model Geometry

The model implemented in Flac3D has dimensions of 100x100x120m (Fig. 16) following the recommendations of the German Society of Geotechnics [81]. The excavation cross section of 63 m² (Fig. 17) was selected based on the standard double track top heading excavation; the selection was made foreseeing the needed calibration to validate the results.

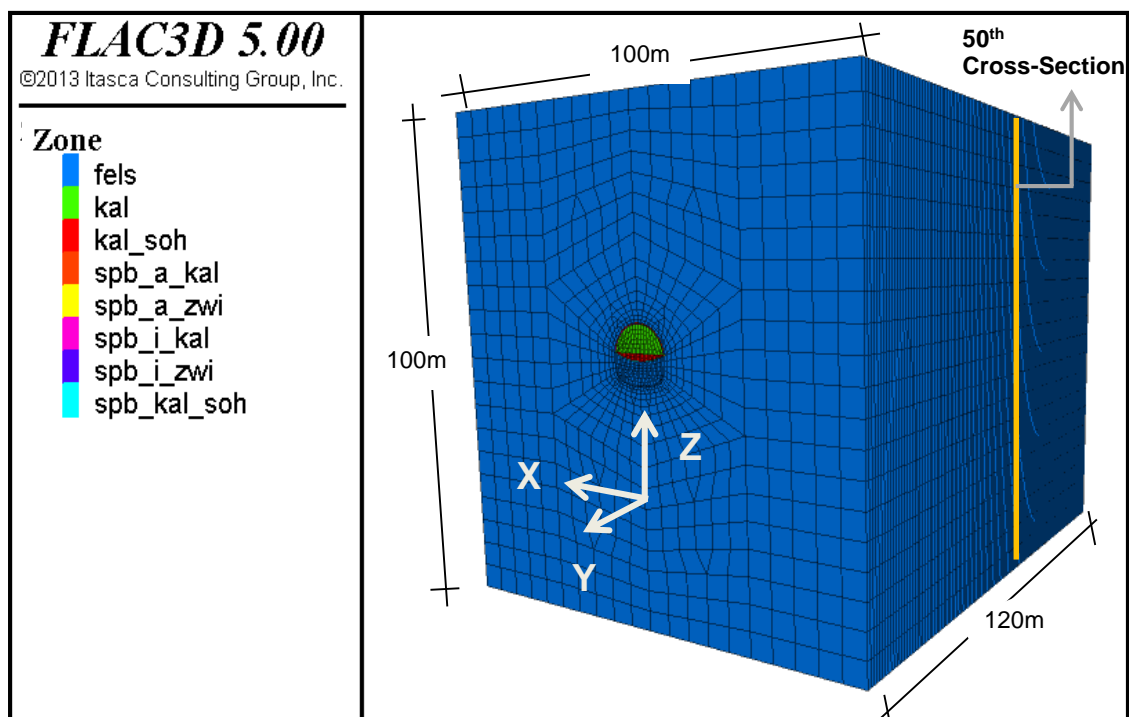


Fig. 16: Flac3D model geometry

The mesh consists of approximately 137.500 hexagonal elements (Brick/Wedge type zone) and it was assembled in order to perform a minimum round length of 1m. Although there is a certain complexity in the implementation of hexagonal elements, its usage ensures minimum computational cost and high accuracy for stress prediction [79].

Taking into account the shortcoming of a FDM software regarding its limitation dealing with complex geometries, the mesh had to be previously prepared considering two scenarios: firstly the main objective of this work (analysis of system behavior) and secondly, for calibration purposes. A closer look to Fig. 16 allows one to detect the inclusion of an additional excavation area (cross section area approximately 120 m²) as well as an additional layer surrounding the excavation. The total area and additional layer will later be used in order to simulate an executed excavation sequence and the implemented support during construction.

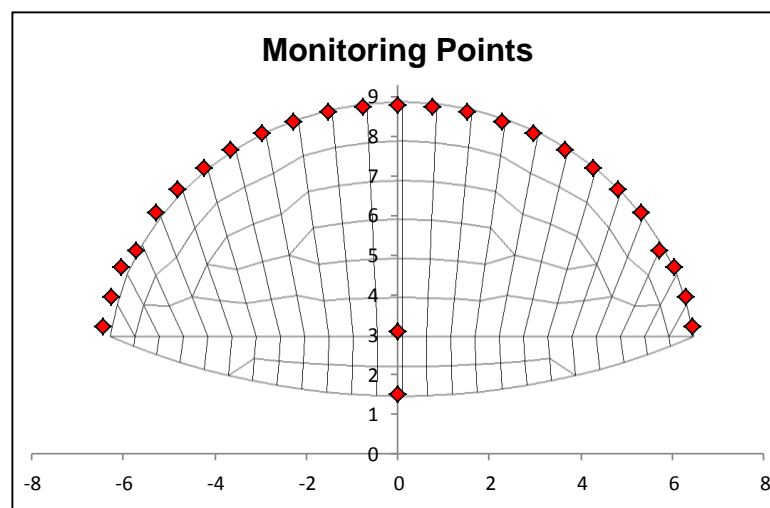


Fig. 17: Flac3D model geometry, excavation geometry

3.2. Model Implementation

The mesh and model remains unchanged throughout the process, however its implementation was divided for two different cases:

- Case 1 is the numerical model implementation for the assessment of ground behavior and
- Case 2 refers to the implementation aim to validate the numerical model.

The programming language FISH embedded in Flac3D [79], was used for the implementation of the model and recording of displacement data, different codes were written for each case.

There is a straight forward model implementation for the main purpose of this work (Case 1) due to the fact that the ground behavior focuses on the failure mechanisms induced by a full face excavation (neither support nor sequence of

excavation is considered). On the other hand, the implementation aimed to validate result (Case 2) must consider the system behavior (excavation sequences and support), which are implicit in the displacement monitoring data used for comparison. The Flow chart from Fig. 18 summarizes the numerical model implementation.

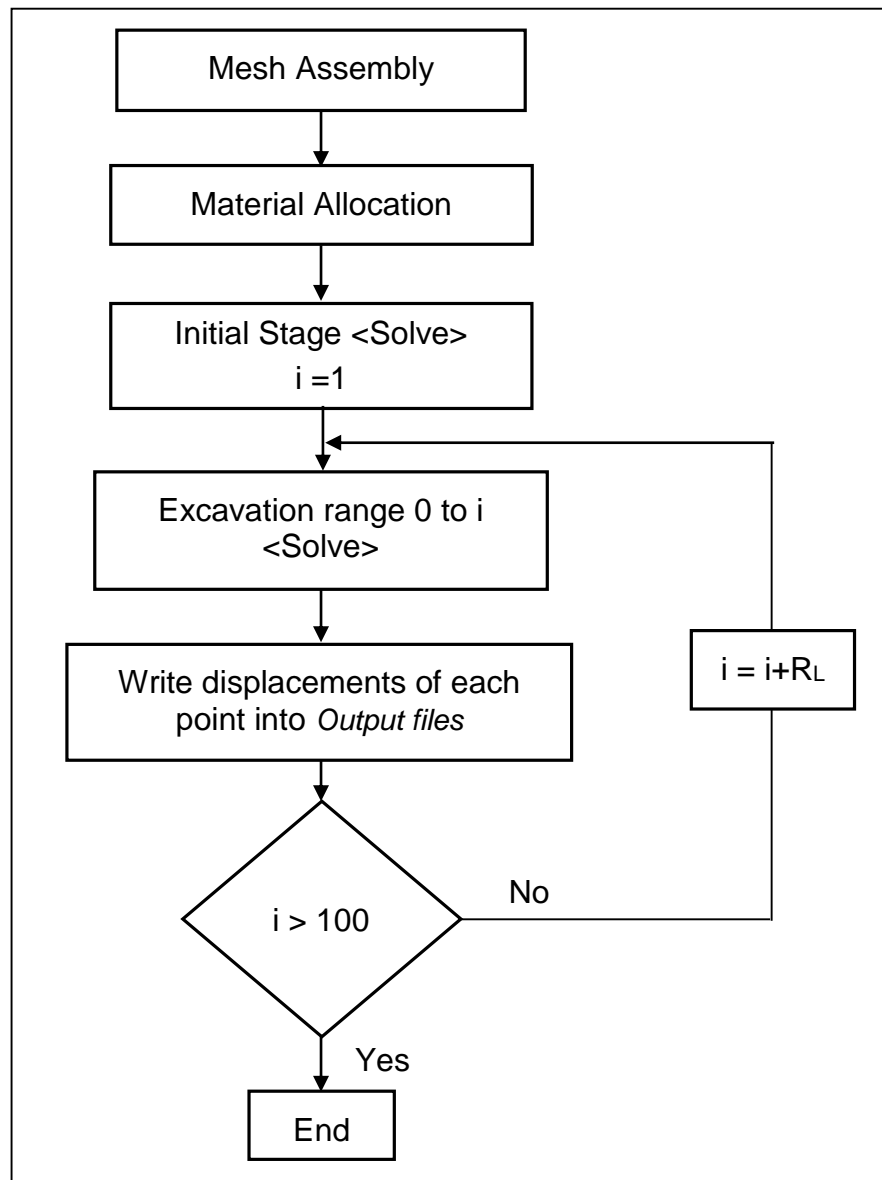


Fig. 18: Model implementation flow chart

Material allocation refers to the implementation of the constitutive model and implicit material properties to be used during calculation. The procedure continues with the calculation of the primary stress conditions (initial stage), followed by the loop that simulates the excavation. The loop starts with the simulation of the round length distance (R_L), which for Case 1 is set to 1m. The results, in term of displacements, are recorded into a text file which is later used for post-processing, the loop continues until the simulation reaches a 100m threshold. The particularities of the numerical model for validation (Case 2) are further explained in the next chapter.

Before implementing the ubiquitous model a first approach was made assigning homogeneous Mohr Coulomb material properties (Table 2), as a reference mark for further simulations. Table 2 summarizes the needed input properties for the constitutive model implementation; note that the right part of the table shows the basic properties needed for a Mohr Coulomb implementation and the left part of the table shows the complementary properties which define the weakness plane behavior and its orientation.

UBIQUITOUS-JOINT MODEL			
Mohr Coulomb Model			
Property	Keyword	Property	Keyword
Matrix		Weakness plane (WP)	
Elastic bulk modulus	Bulk	Joint cohesion	Jcohesion
Cohesion of matrix	Cohesion	Joint dilatancy	Jdilatation
Dilatation of matrix	Dilatation	Joint friction angle	Jfriction
Fric angle of matrix	Friction	Joint tension limit	Jtension
Elastic shear modulus	Shear	Orientation:	
Tension limit of matrix	Tension	WP. Dip Direction	Jddirection
		WP. Dip	Jdip

Table 2: Input parameters

3.3. Displacement Data Post-Processing

Results, regarding displacements for each monitoring point, are recorded in a text file (Fig. 18). Using visual basic tools, data is imported into an Excel worksheet for post-processing.

The first step is the introduction of a local coordinate system and conventions for each monitoring point. Conventions and system coordinates used in this work are partially taken from Grossauer's work [76].

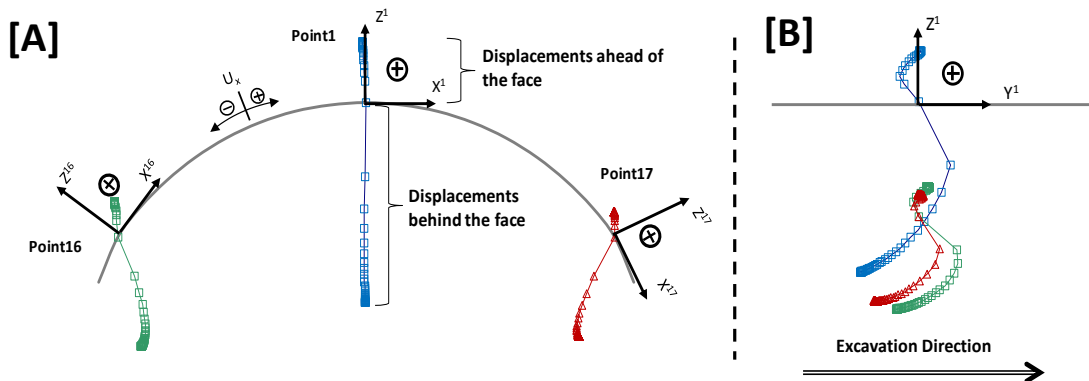


Fig. 19: Local coordinate system and conventions
 [A]. Cross Section, [B] Longitudinal Cross Section

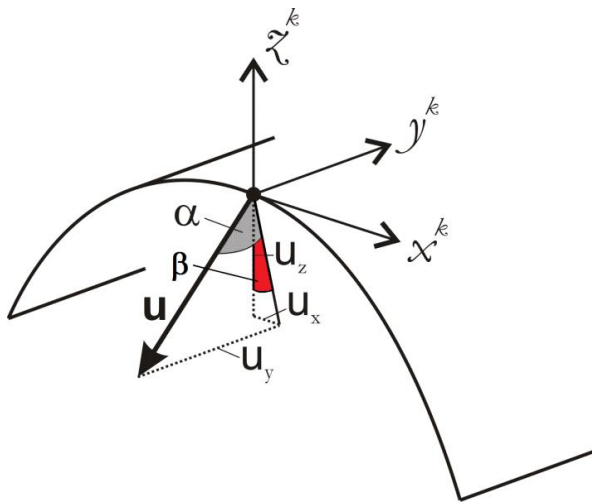


Fig. 20: Conventions summary

(Radial displacement 'Uz', tangential displacement 'Ux' and longitudinal displacement 'Uy'. 3D displacement vector 'alpha' in gray and inclination of displacement vector 'beta' in red)

The last convention used in the present work (not used by Grossauer) is the inclination of the displacement vector, which is the orientation vector in 2D on a X-Z plane, closely related to tangential displacements (Fig. 21).

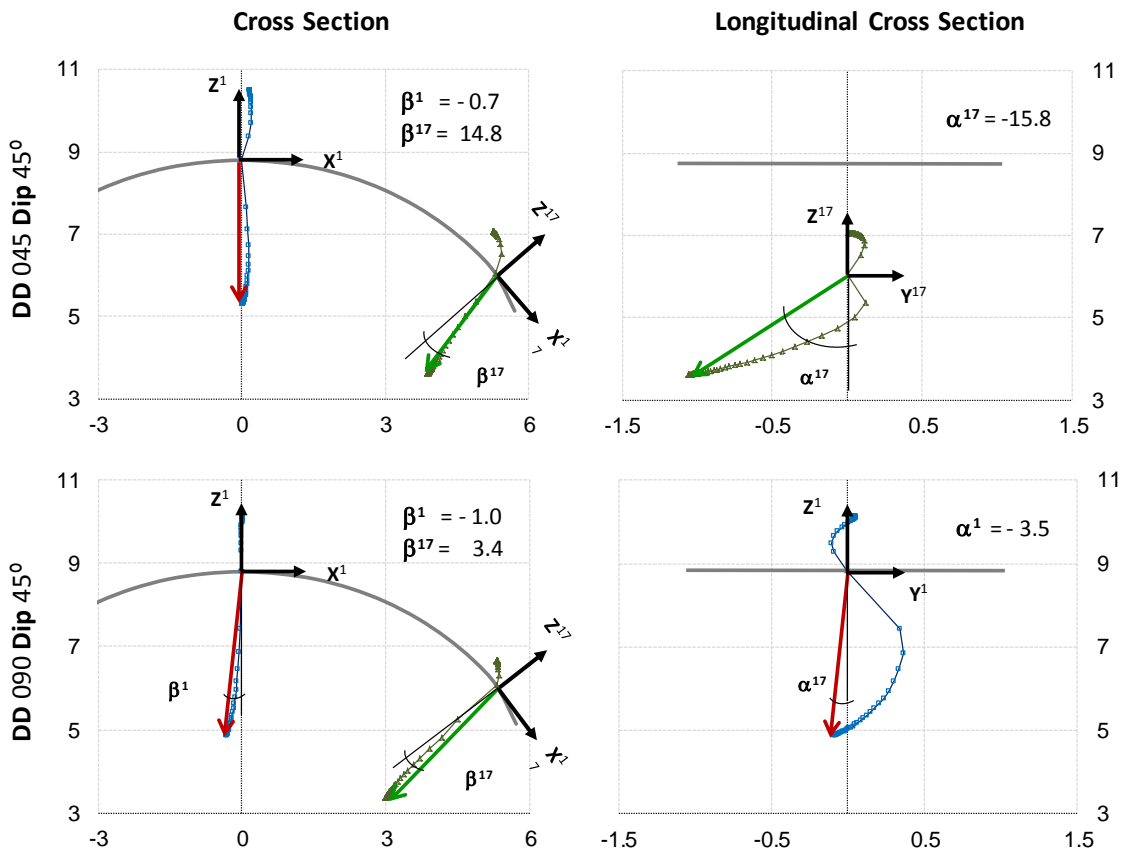


Fig. 21: Conventions summary examples, displacement scale 1:100

After local coordinates and conventions are set, the next step is to calculate radial and tangential angles, alpha (α) and beta (β). Fig. 21 shows some examples of

the conventions used for the present work. The cross section (X-Z plane) is used to illustrate the angle beta, negative values are reached if clockwise rotation, with respect to the local coordinates, takes place. The longitudinal section it is possible to detect changes in angle alpha which, with respect to the local coordinates, reaches positive value rotating towards the excavation.

The simulation results for each set of dip angle and dip direction are summarized into a worksheet (Fig. 22) displaying material properties, weakness planes graphical representation, displacement development (P1 crown point), displacement plot in the Z-X plane (cross section) and displacement plot in the Z-Y plane (longitudinal section).

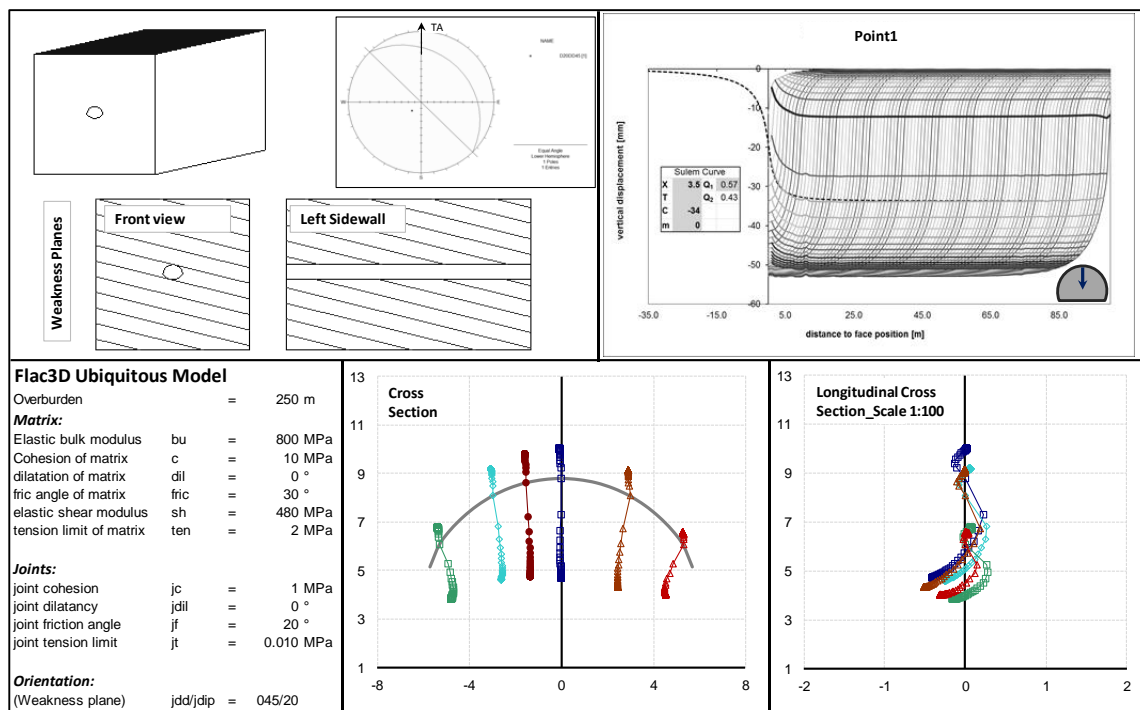


Fig. 22: Results for DD=045, dip angle=20°

There is a great amount of data, which need proper graphical representation to facilitate the recognition of trends and behavior changes depending on the relative orientation of the weakness planes. Considering this, the following plots were prepared for each dip direction:

- [1]. Tangential displacements v_s . Arc length
- [2]. Radial displacements v_s . Arc length
- [3]. Beta (β) v_s . Arc length (2D)
- [4]. Alpha (α) v_s . Arc length (3D)

An example of each plot comparing the homogeneous model and a ubiquitous joint model (weakness plane dip direction 090 and dip angle equal to 45°) is shown in Fig. 23, to understand the cross section and the longitudinal section plots. The figure clearly displays variations on the displacement characteristics, caused by

the presence of a weakness plane. The cross section shows changes in the tangential, radial displacements magnitude and rotation of beta and additionally, the longitudinal section is used to display rotation of alpha.

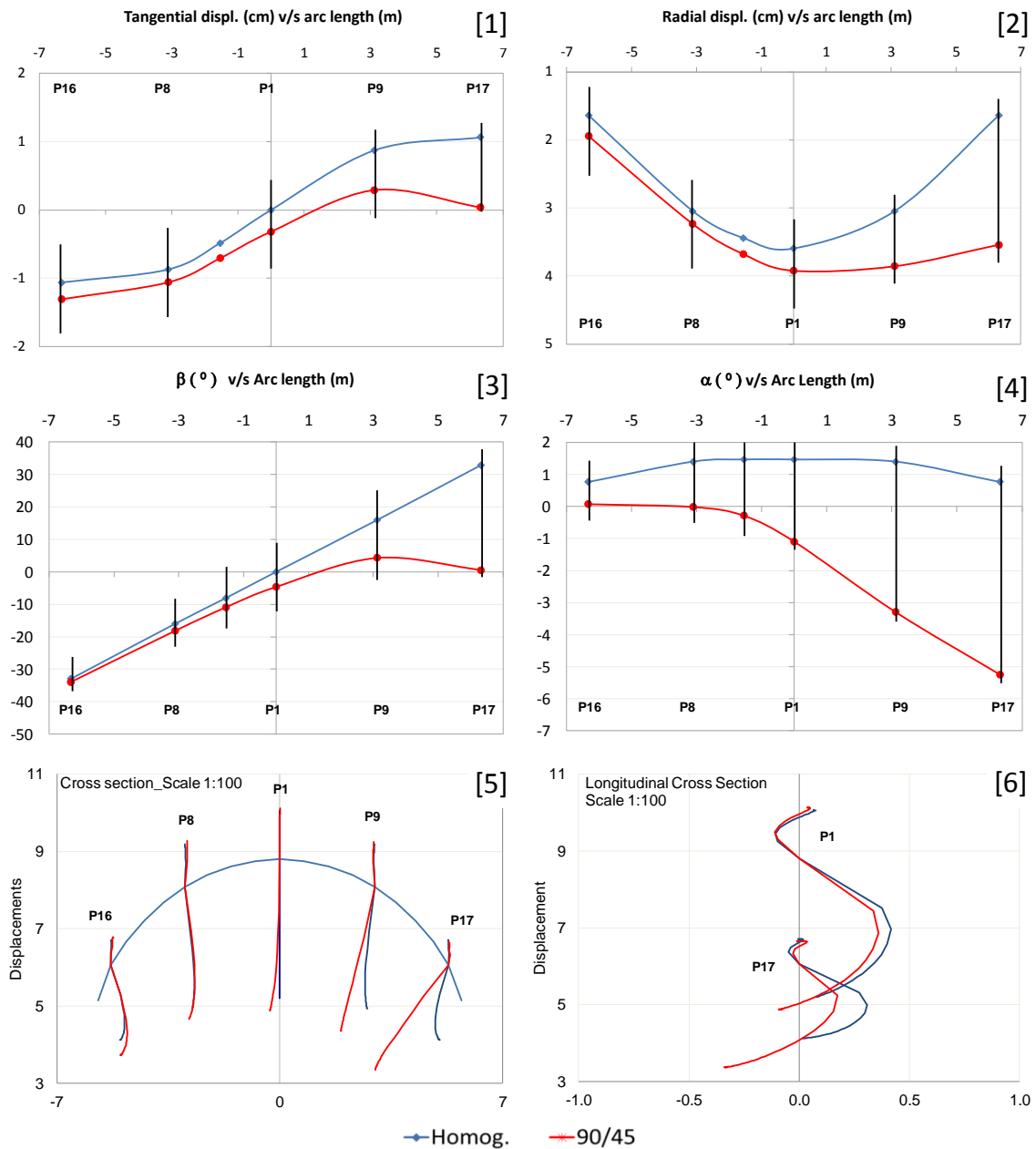


Fig. 23: Results graphical representation, homogeneous model vs. DD90D45

3.4. Numerical Model Validation

In order to validate the results, a verification of the numerical model was implemented. Numerical simulations are one of the most widely used methods in tunnel engineering. However, a proper validation allowing the engineer to assess the capability of a model to simulate a ground behavior is seldom performed. The

capability and accuracy of results do not only depend on the constitutive model but also on the numerical model dimensions and mesh discretization.

There are different calibration procedures where the basic idea is to compare the output results, of a given numerical model, with measured data originated from either experimental tests and/or construction site monitoring.

The present work makes use of displacement monitoring data coming from the Galgenberg tunnel in Austria in order to calibrate the ubiquitous joint model from Flac3D. This project was selected based on:

- A rather wide sector of the tunnel was excavated in layered rock mass (phyllites).
- Enough data from the implemented 3D displacements monitoring system are available.
- Geological characteristics for each cross section were recorded (geological face mapping).
- Documentation regarding excavation sequences and implemented support is available.

The displacement monitoring data collected during the Galgenberg tunnel construction allow the calibration of the numerical model in 3 dimensions. Fig. 24 displays the implemented numerical model for the Galgenberg tunnel and the monitoring point locations, which match the on-site installed and monitored reflective target. Displacement data recorded for each point are used to compare the results from the numerical model and monitored data.

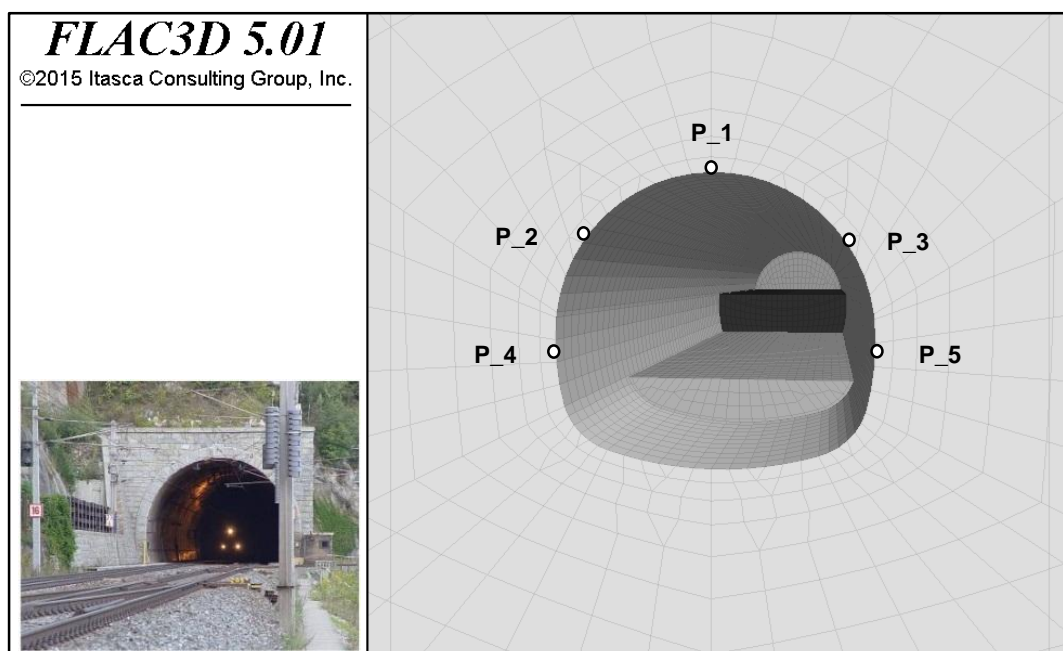


Fig. 24: Numerical model and monitoring points used for calibration at the Galgenberg tunnel project

In contrast to the implementation presented in the section 3.2 (assessment of ground behavior), the numerical model assembled for calibration purposes evaluates the system behavior, including excavation sequences and support considerations. The excavation sequence for the analyzed cross sections was divided into Top Heading (TH), Bench (B) and Invert (I) with a total excavation area of approximately 124m².

The model assembled to evaluate the capability of the numerical model is based on a back analysis. Important parameters such as in-situ stresses calculated based on the overburden for a particular cross section, geological features obtained from geological mapping, excavation sequence represented in excavation areas and round length and the implemented support are taken as “fixed” input parameters remaining unchanged throughout the calibration process.

Considering that there is insufficient available information regarding rock mass and joint properties from the studied area and only few general considerations regarding global stress conditions and its orientation, the FISH code includes such parameters as “variable” input parameters which allow the calibration of the numerical model.

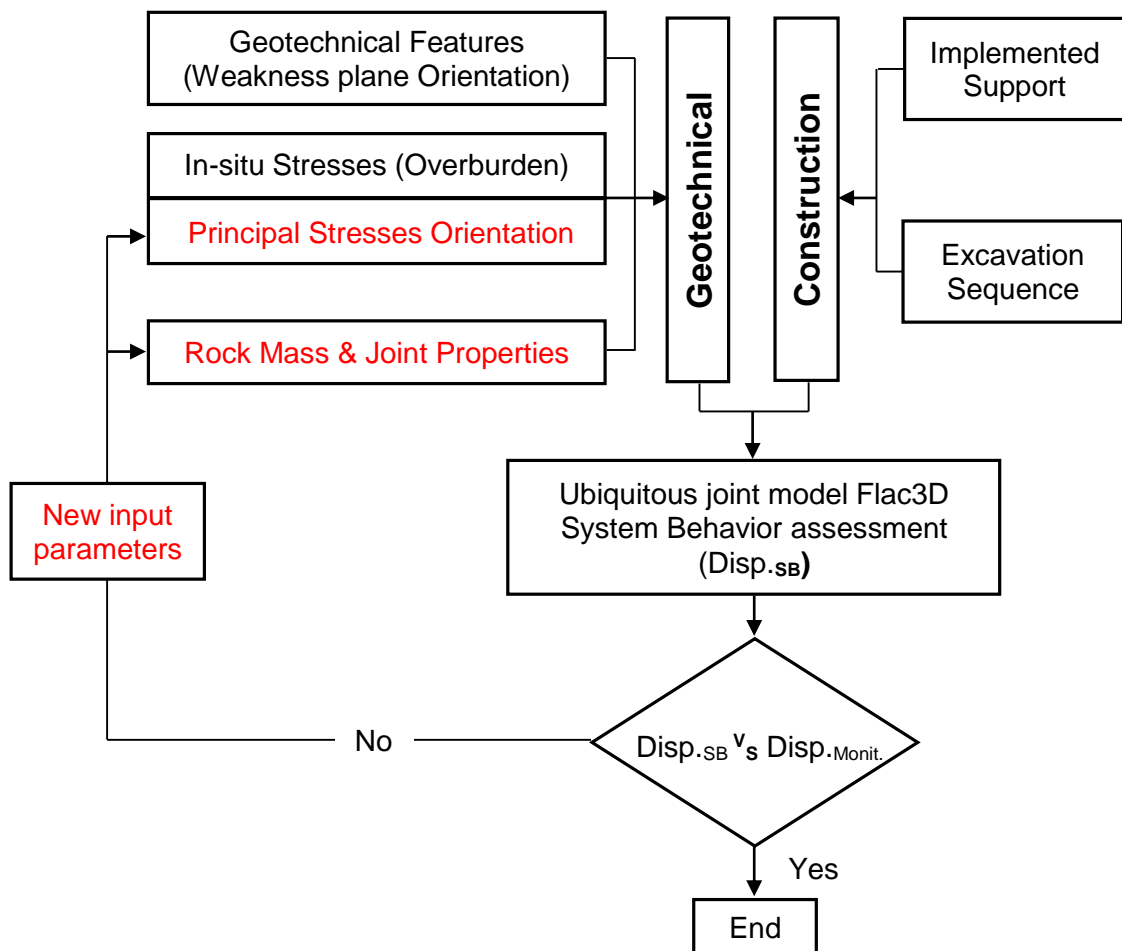


Fig. 25: Flow chart for the numerical model calibration

The calibration is mainly done through multiple numerical simulations varying the “variable” input parameters to match the monitored displacements, in terms of displacement development, magnitude and orientation. The final calibrated numerical model should display, not perfectly match, the behavior shown by the implemented system (geotechnical model + construction concept) as the excavation took place.

The final results of each numerical simulation are great in number. However, the main focus of the calibration is the development, magnitude and orientation of displacements, exhibited by a given System Behavior (SB). Such displacements are named “Disp.SB” (Fig. 25) and are later compared with the monitored displacement data referred as “Disp.Monit.”. A new numerical simulation, with a new set of input parameters takes place if the magnitude of tangential and radial displacements, beta and alpha values do not fulfill the criteria set for the comparison.

3.4.1. Implemented structural elements

The support measures installed during construction included, wire mesh reinforced shotcrete, steel arches, and rock bolts. The following tables present the properties used for the different structural elements.

Shotcrete was simulated through SHELL elements with isotropic behavior and considering a rigid bond between the rock mass and the structural element. This condition is appropriate taking into account that the studied section exhibits rather small displacements; it is important to keep in mind the Flac3D ubiquitous joint model limitations dealing with large displacements (section 2.3.2).

SHOTCRETE			
Structural element type Flac3D: (Sell SHELL)			
Property			
Elastic Modulus	emodul	16	GPa
Poisson's ratio	nu	0.2	
Thickness	thick	varies	m

Table 3: Shotcrete input parameters

The rheological behavior of the shotcrete is important in order to reach realistic results [82]. To model such behavior, a characteristic elasticity

curve was implemented with the reduction values shown in Table 4 and Fig. 26. The factor is also applied to the elastic modulus shown in Table 3 based on excavated meter recorded during construction.

Even though a time dependent constitutive model for the shotcrete was not implemented, the inclusion of the mentioned strength reduction factor is a proper approximation, considering the scope of the numerical model calibration.

Days	1	3	7	28
Strength reduction due to rheological behavior (%)	80	45	25	0

Table 4: Strength factor_shotcrete

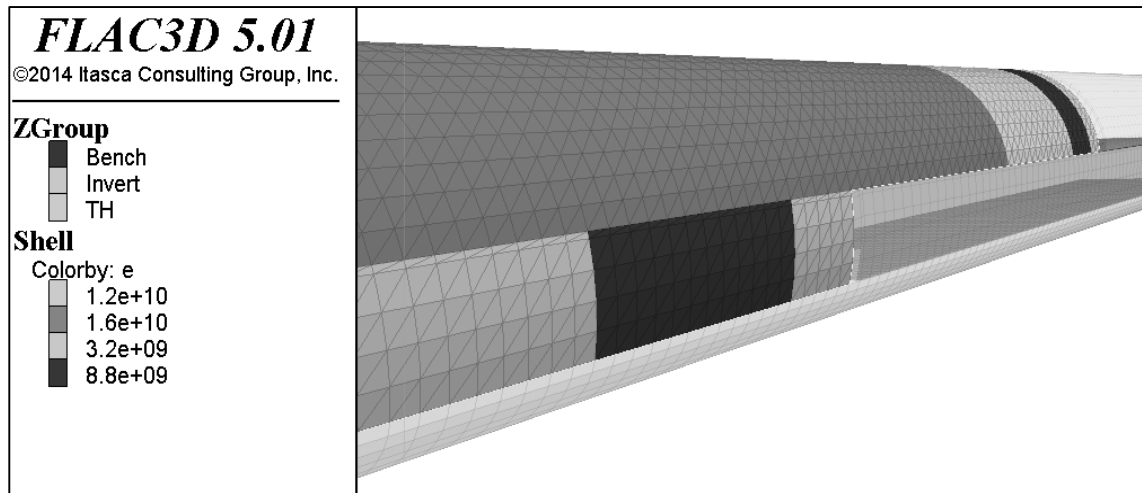


Fig. 26: Shell elements E-modulus strength increment

Steel rock bolts are simulated in Flac3D with CABLE structural elements. CABLE elements simulate a perfectly elastic material that yield in tension and compression, but cannot resist bending moments, contrary to the PILE elements where bending behavior is considered.

The CABLE elements are mainly governed by an axial component defined by the implemented steel bar and a shear behavior governed by the definition of a grouting material surrounding the steel bar. Table 5 displays the implemented input parameters.

ROCK BOLTS (SN Type)			
Structural element type Flac3D (Sel CABLE)			
Property			
Elastic Modulus	emodul	200	GPa
Cross Section Area	xcarea	2.1E-03	m ²
Grouting_Perimeter	gr_per	0.25	m
Tensile Yield Strength	yten	3.5E+05	N
Grouting_Cohesion	gr_coh	1.56E+06	N/m
Grouting_Friction	gr_fric	0	°
Grouting_Stiffness*	gr_k	8.0E+10	N ·m/m

Table 5: Rock bolts input parameters

The simulation of the steel arches was done through PILE structural elements. Such elements allow the inclusion of springs with a given stiffness into the calculation allowing the simulation of the pile-shotcrete interface. Note that the values presented in Table 6 assume that the steel arch is embedded into the shotcrete.

STEEL ARCHES (HEB 100)			
Structural element type Flac3D:		(Sel PILE)	
Property			
Elastic Modulus	emodul	200	GPa
Cross Section Area	xcarea	2.6E-03	m ²
Second moment with respect to the Y axis	xciy	4.5E-06	m ⁴
Second moment with respect to the Z axis	xciz	1.7E-06	m ⁴
Polar Moment of Inertia	xcj	6.2E-06	m ⁴
Cohesion_Normal coupling spring	cs_ncoh	1.0E+20	N/m
Friction_Normal coupling spring	cs_nfric	0	°
Stiffness_Normal coupling spring	cs_nk	1.20E+11	N · m/m
Cohesion_Shear coupling spring	cs_scoh	5.7E+05	N/m
Friction_Shear coupling spring	cs_sfric	0	°
Stiffness_Shear coupling spring	cs_sk	6.00E+09	N · m/m

Table 6: Steel arches (HEB100) input parameters

3.4.2. Calibrated cross sections Galgenberg tunnel.

The calibration procedure was done for two cross sections of the Galgenberg tunnel project from the Jassing east drift (phyllites): 1st. km. 0 + 296 and 2nd. km. 0 + 340.

A brief description regarding geological conditions, implemented construction concept and attainment of the initial material parameters is presented in the following sections, framed by the compatibility of the on-site conditions with the used constitutive model.

3.4.2.1. Geological conditions

The geological conditions in the studied cross sections fulfill the needed requirements presented in the chapter 3 for a ubiquitous joint model simulation. The excavated material is mainly composed by quartz phyllites and described as: “Laminated rock formation of gray to dark gray phyllites, changing in quartz content, partly graphitic. The foliation surface often carries feeble clayish material varying in color from light grey to black” [83].

The strike of the tunnel is approximately N 45° E and was excavated in the described rock mass with predominant weakness/foliation planes exhibiting a NE-SW orientation. The weakness planes and specific geological features for each cross section are assumed to control the overall displacement behavior of the excavation. The following figures display the geological face mapping done during construction for each cross section.

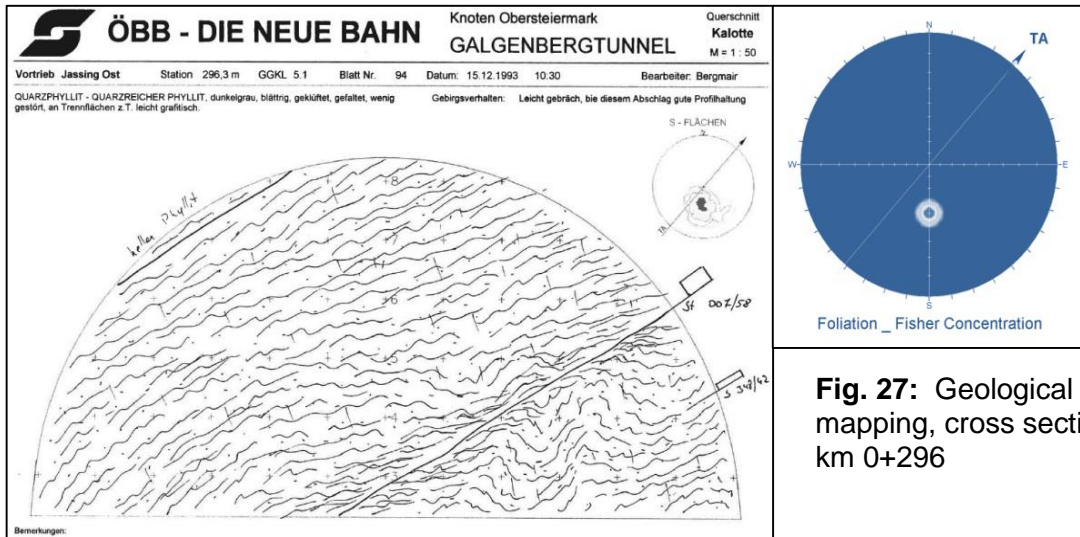


Fig. 27: Geological mapping, cross section: km 0+296

Fig. 27 and Fig. 28 include the so called Fisher concentration contour plot for the weakness plane (foliation) found on the geological documentation. The plot summarizes multiple orientation measurements of dip and dip direction into a stereographic projection. The values shown in the plot will later be implemented into the numerical model as weakness plane orientation.

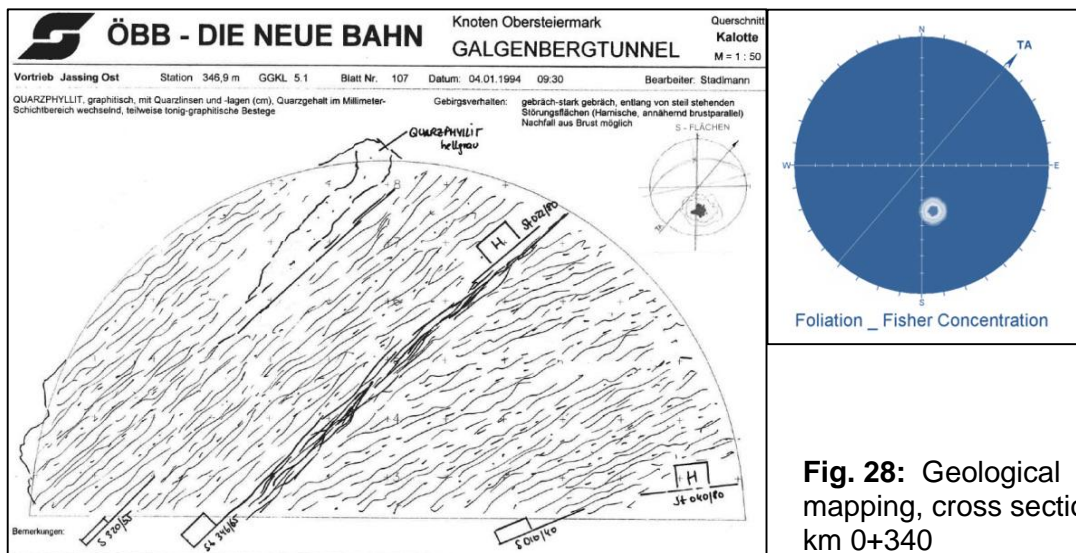


Fig. 28: Geological mapping, cross section: km 0+340

3.4.2.2. Numerical model input parameters

The input parameters for the calibration were initially determined with the help of an analytical solution [31]. A further step, which allowed the inclusion of the installed support as well as discontinuities, was taken with the implementation of a Phase2 2D FEM numerical model (Fig. 29). Both approaches considered total displacements as comparative/reference values to set the initial parameters for the Flac3D numerical model.

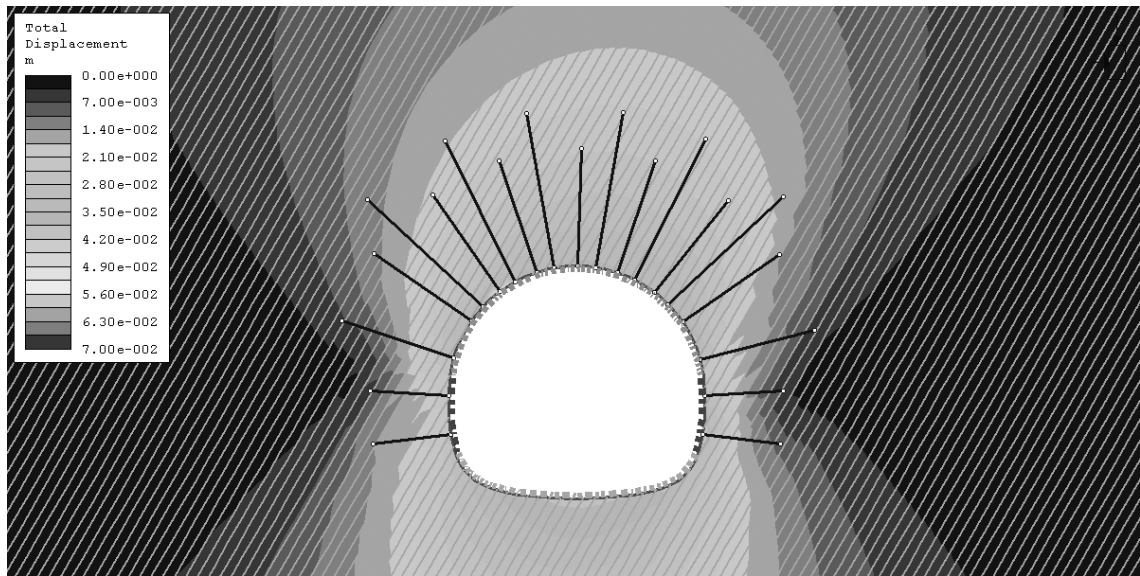


Fig. 29: 2D Numerical model, cross section: km 0 + 296

The mentioned approaches yielded the values presented in Table 7 for rock mass and weakness plane parameters. The shown final displacement values are the ones registered during the monitoring campaign on cross section. Total displacements were calculated by combining the analytical solutions for displacement presented by Hoek et al. [84] and Carranza & Fairhurst [85] and the conclusion presented by Klopčič [70] regarding influence of discontinuities on displacements ahead of the face.

Jassing Ost _ km 0 + 296				Jassing Ost _ km 0 + 340							
Geofit Cross Section k 0+302.3				Geofit Cross Section k 0+339.7							
Geological Documentation k 0+296.3				Geological Documentation k 0+346.9							
Final Displacement:	26.1 mm	Sigma1	4.05 Mpa	Final Displacement:	20.1 mm	Sigma1	4.86 Mpa				
%Predisplacement:	35%	Sigma2/3	2.03 MPa	%Predisplacement:	31%	Sigma2/3	2.43 MPa				
Total Displacement:	40.2 mm	Ko	0.5	Total Displacement:	28.9 mm	Ko	0.5				
OverBurden:	150 m			OverBurden:	180 m						
Orientation T. Axis:	41 NE-SW			Orientation T. Axis:	41 NE-SW						
PROPERTIES				PROPERTIES							
Matrix	E	1300 MPa	Joints	Jc	0.35 MPa	Matrix	E	2800 MPa			
	Bulk	1083.3 MPa		Jphi	19 °		Matrix	Bulk	2333.3 MPa		
	Shear	500.0 MPa		DD	319 °			Matrix	Shear	1076.9 MPa	
	C	0.85 MPa		Dip	55 °				Matrix	C	1.5 MPa
	Phi	19 °		Poison	0.3					Matrix	Phi
				Matrix	Poison	0.3					

Table 7: Initial material properties and boundary conditions

Boundary conditions are calculated in terms of total stresses as no presence of water was registered in the geological documentation. The initial vertical stress value is set based on material density and overburden. Magnitudes of horizontal stresses are initially set considering a lateral pressure coefficient k0 of 0.5. These values are later adjusted as part of the calibration process (Fig. 25).

3.4.2.3. Construction concept

Prior to assessing the System Behavior the numerical model has to accurately simulate the construction concept carried out during the construction of the Galgenberg tunnel.

The tunnel was excavated with the conventional method (drill and blast). Fig. 30 and Fig. 31 display excavation and support sequence, support elements and the Flac3D numerical model for the cross section km 0+290 and km 0+340, respectively. It is worth mentioning that the shown values for distance between excavation sections are limited to 50 meters. Although actual distances between top heading-bench and bench-invert distance are larger, this assumption has no effect on the final displacement behavior.

For the cross section km 0+290 additional bolting was installed, the code written for the implementation of the support takes into account the additional support as well as the distance to the face at the time of installation.

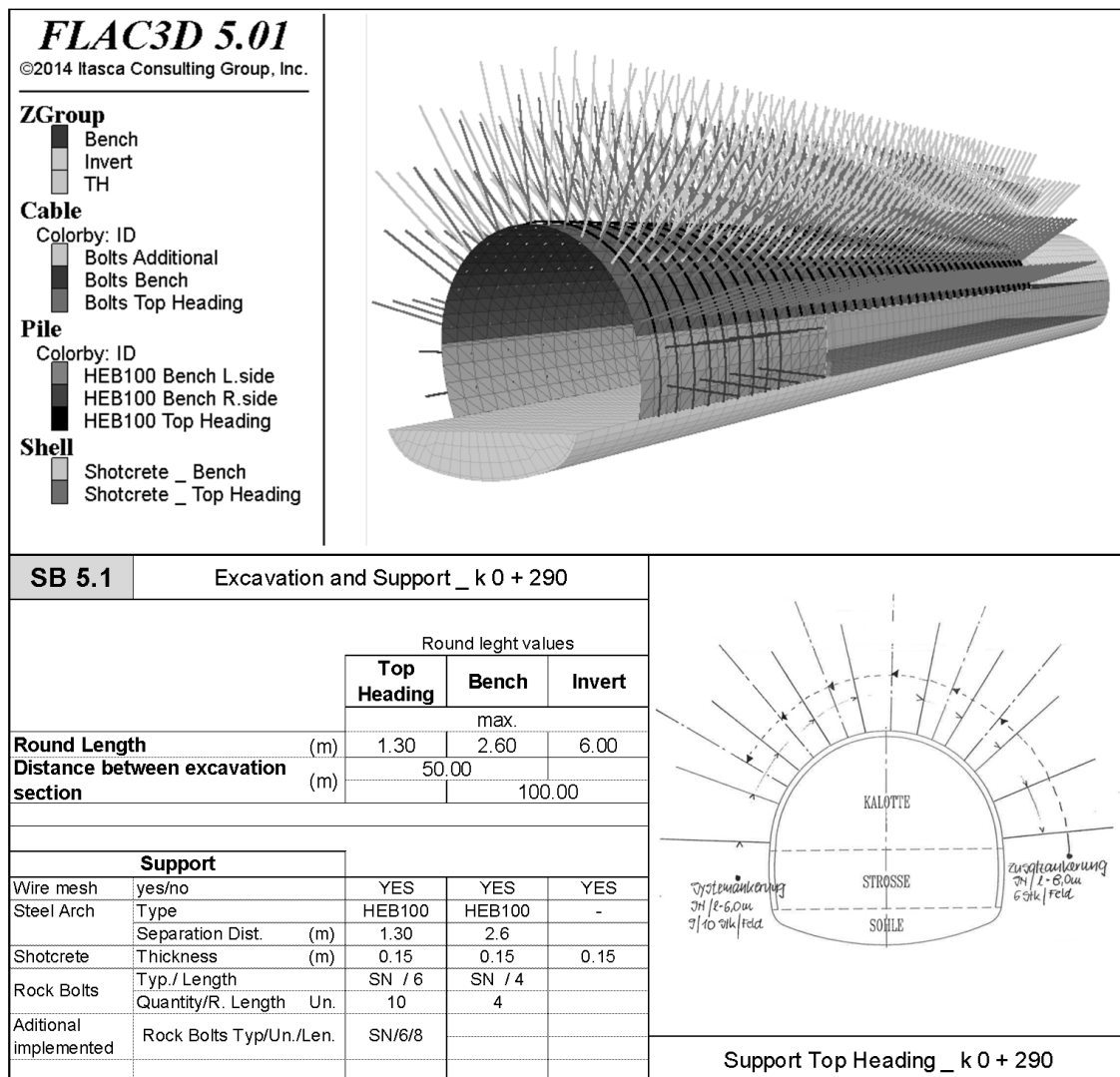


Fig. 30: Numerical model construction concept, cross section: km 0 + 290

The bolt pattern for the next analyzed section had been changed during construction, to account for the discontinuities influence (Fig. 31). A denser pattern was applied from the crown and towards the left side-wall, complying with the area where discontinuities perpendicularly intersect the excavation, as shown in the geological mapping (Fig. 28).

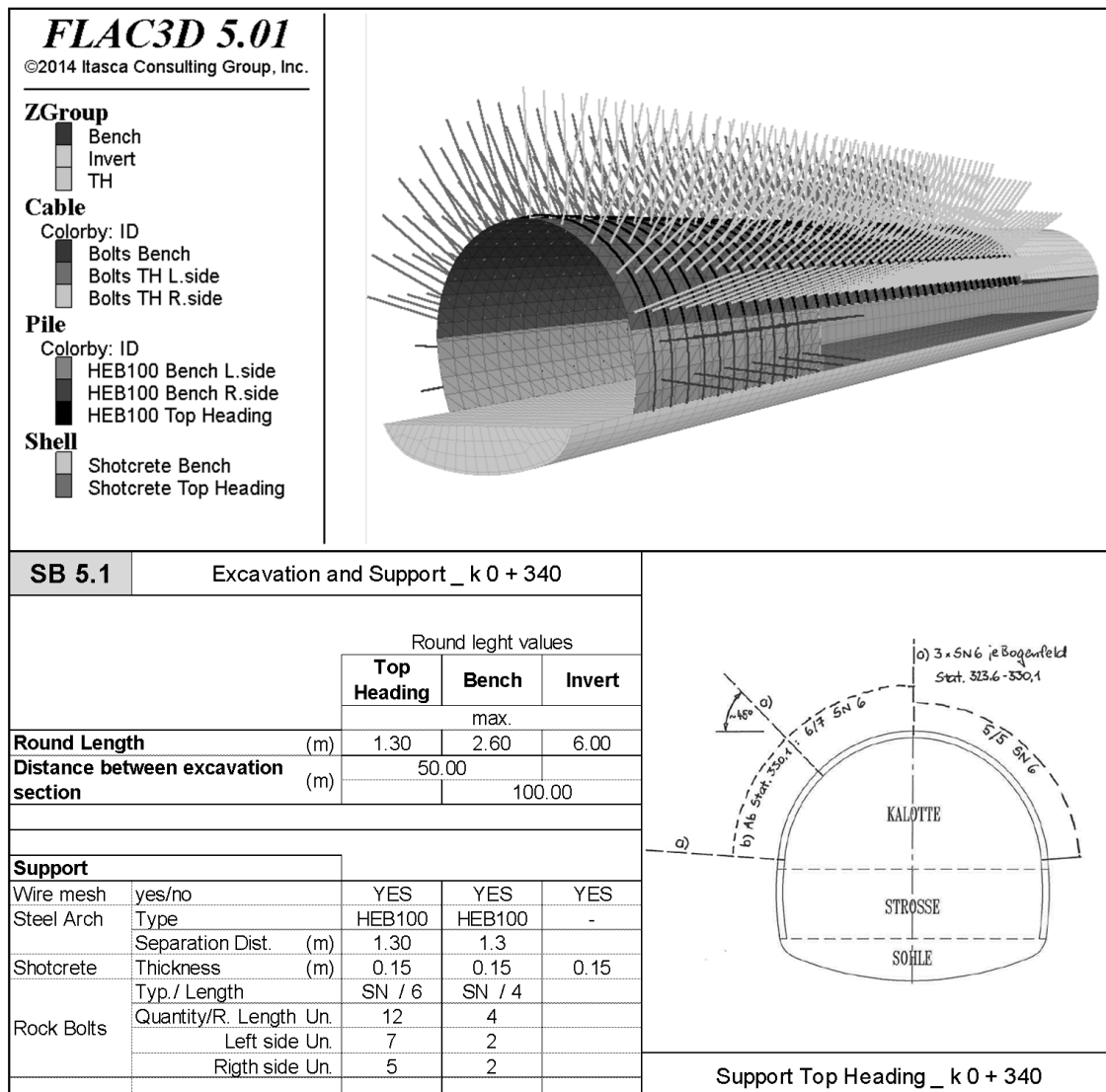


Fig. 31: Numerical model construction concept, cross section: km 0 + 340

3.4.3. Results validation

The calibration loop stops once the numerical model is able to simulate the displacements behavior recorded during construction (Fig. 25). The ubiquitous joint constitutive model was capable of displaying the observed behavior during construction, after 9 simulations for the cross section km 0+296 and 7 for the cross section km 0+340.

Adjusted rock mass and weakness plane parameters, as well as boundary conditions are summarized in Table 8. In comparison with the initial implemented parameters displayed in Table 7, there are significant changes in terms of strength, elastic properties and distribution of primary stresses. During the calibration process the need of including an extra parameter “Blast Influence” was observed. The parameter quantifies the influence of the first blast, after the installation of the monitoring reflective targets (first reading), on the displacements. This influence is inversely proportional to the distance between the monitoring point and face position at the moment of the first reading, e.g. a distance between target-face equal to 0 m yields a 100% influence, however, if the distance is greater than the round length the parameters “blast influence” will be set to 0%.

Jassing Ost _ km 0 + 296 (Calibrated)				Jassing Ost _ km 0 + 340 (Calibrated)							
Geofit Cross Section k 0+302.3				Geofit Cross Section k 0+339.7							
Geological Documentation k 0+296.3				Geological Documentation k 0+346.9							
Final Displacement:	26.1 mm	Sigma1	4.05 MPa	Final Displacement:	20.1 mm	Sigma1	4.86 MPa				
%Predisplacement:	35%	Sigma2/3	3.65 MPa	%Predisplacement:	31%	Sigma2/3	4.13 MPa				
Total Displacement:	40.2 mm	K0	0.9	Total Displacement:	28.9 mm	K0	0.85				
OverBurden:	150 m			OverBurden:	180 m						
Orientation T. Axis:	41 NE-SW			Orientation T. Axis:	41 NE-SW						
			Influence				Influence				
TopHeading Face pos._first reading	0.3 m		77%	TopHeading Face pos._first reading	0.54 m		58%				
Bench Face pos._first reading	153.5 m		0%	Bench Face pos._first reading	133.4 m		0%				
UBIQUITOUS JOINT MODEL				UBIQUITOUS JOINT MODEL							
Mohr Coulomb Model				Mohr Coulomb Model							
PROPERTIES				PROPERTIES							
Matrix	E	1050 MPa	Joints	Jc	0.20 MPa	Matrix	E	1400 MPa	Joints	Jc	0.3 MPa
	Bulk	875.0 MPa		Jphi	17 °		Bulk	1166.7 MPa		Jphi	20 °
	Shear	403.8 MPa		DD	319 °		Shear	538.5 MPa		DD	305 °
	C	0.8 MPa		Dip	55 °		C	1.2 MPa		Dip	40 °
	Phi	26 °		Poison	0.3		Phi	27 °		Poison	0.3

Table 8: Calibrated material properties and boundary conditions

A comparison from the results was initially done through the computational software Geofit® form 3G. The software was mainly used to allow the calculation of parameters Q1 & Q2, referred in Sellner’s work as pre-face and post-face portion of the total displacement magnitude respectively [86]. The values were used and later summarized in order to compare and quantify the fitting of the Flac3D calculated displacements development and those monitored on site.

Simulations with the Mohr Coulomb constitutive model were conducted for each cross section, having as input parameters those shown in Table 8 (calibrated parameters). The simulation results are also included in the comparison aiming to highlight some advantages of a smeared discontinuous model.

Fig. 32 and Fig. 33 are presented as an example of the calibration final results. Plotted in the figures is the displacement development from the monitored data as well as the one calculated through the homogeneous and ubiquitous joint model.

Such comparisons were done for the 5 available monitoring targets in X, Y and Z direction.

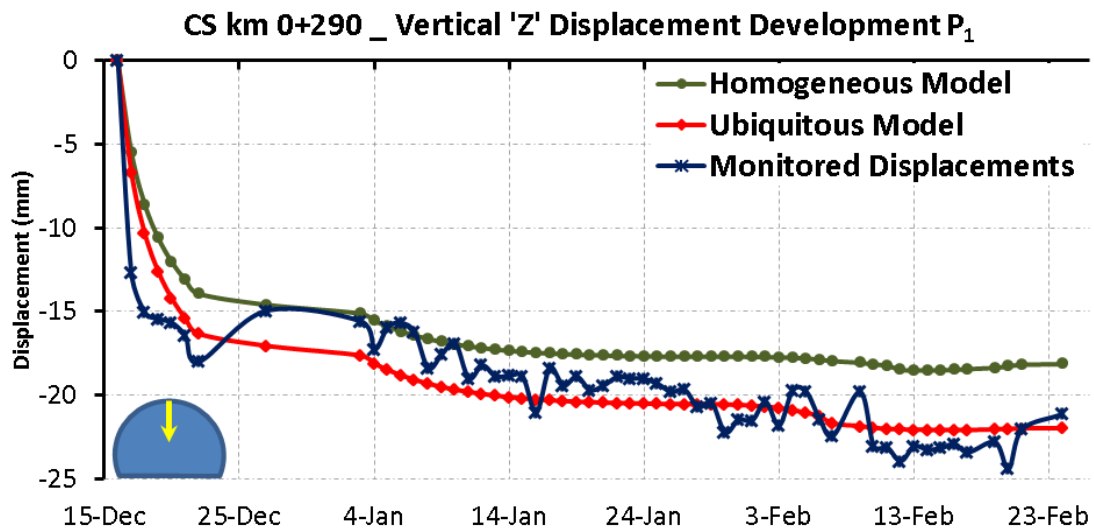


Fig. 32: Galgenberg tunnel vertical displacements, cross section: km 0+290

Fig. 32 displays the “Z” (vertical/radial) displacements development for P1 (cross section km 0+290) which constitutes the tunnel crown monitoring target, a better fit was reached by the ubiquitous joint model in comparison to the homogeneous model. In this case, the influence of the weakness plane, for vertical displacement development, is mainly seen in displacements magnitude, rather than its orientation, this observation will be further explained and studied in the next chapter.

A longitudinal section, such as the one seen in Fig. 33, clearly displays an advantage of incorporating the weakness plane into the numerical model. Plotted in the figure is the “Y” (longitudinal) displacements development for P2 (cross section km 0+340) which constitutes the top heading’s left side-wall monitoring point. The studied cross section exhibit a weakness planes’ dip and dip direction, which influences the right side-wall by re-orienting the displacements towards the excavation face, the opposite behavior is observed on the left side-wall where displacement tend to be orientated against the excavation direction (Fig. 35 and Fig. 37). Such asymmetric behavior cannot be numerically assessed without the inclusion of the weakness plane.

Contrary to the failure criterion implemented in the ubiquitous joint model, the Mohr Coulomb model does not incorporate plastic corrections and stress re-orientation based on the dip and dip direction of the weakness plane. This shortcoming becomes evident in the calibrated cross section were the weakness plane plays a major role in the displacement behavior.

The results from the numerical model display the capability of the model to simulate the observed behavior during excavation. The results presented in the following figures make usage of the conventions summary presented in Fig. 20.

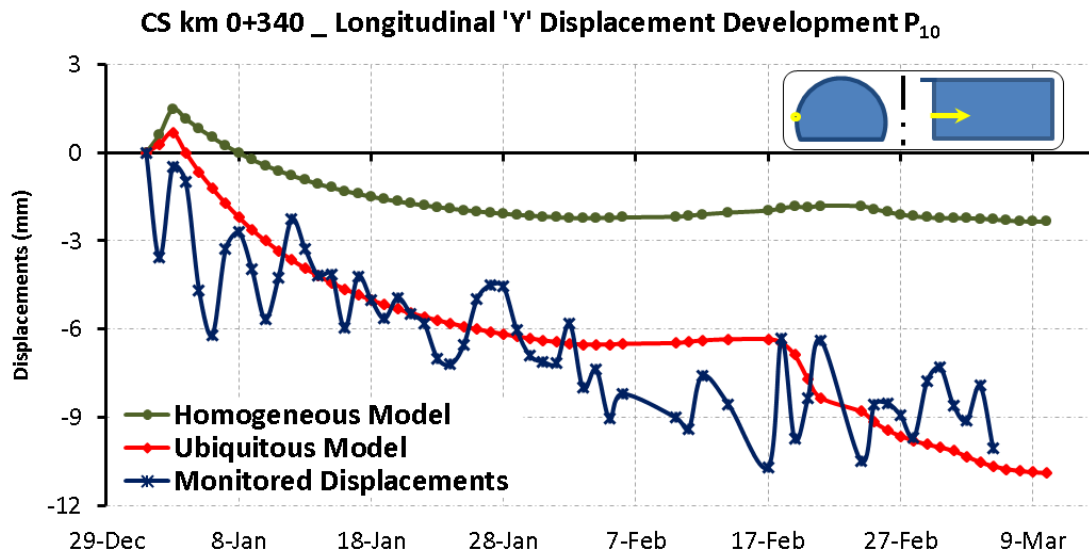


Fig. 33: Galgenberg tunnel longitudinal displacements, cross section: km 0+340

A broad summary of the results shows that for both cross sections and all monitoring points: 1st. Deviations between 0 – 20% were reached for final displacements values, 2nd. Angle beta deviation is lower than 15° and 3rd. Angle alpha deviation is lower than 20°. It should be highlighted that alpha entails an accumulative deviation as its rotation directly depends on beta and the magnitudes of displacements (Fig. 20).

The summary presented at the end of Fig. 34 and Fig. 36 display acceptable deviations, it highlights in red positive values and in yellow negative values allowing one to quickly inspect if the observed behavior is properly simulated by the numerical model. Displacements simulated through the ubiquitous joint model are more in agreement with those measured than displacements simulated with the Mohr Coulomb model. A general overview of the results is adequate with the exception of the 3D displacement angle alpha for P5 (bench right wall target), where the observed orientation of the vector could not be simulated by the numerical model.

A noticeable out of trend behavior is observed for the crown point P1 of the CS km 0+340, where monitored displacements exhibit a strong orientation towards the left side-wall. The behavior is associated with the geological features found on this cross section. The geological face mapping (Fig. 28) recorded a slickenside with a dip direction 036 and dip 80 intersecting the tunnel's top heading in the crown and extending towards the left side-wall; such surface constitutes an additional weakness plane where strength parameters are exceeded causing slip to take place along the slickenside.

The influence of the slickenside is notable in Fig. 37 where an overlay of the monitored displacements and the geological face mapping is presented.

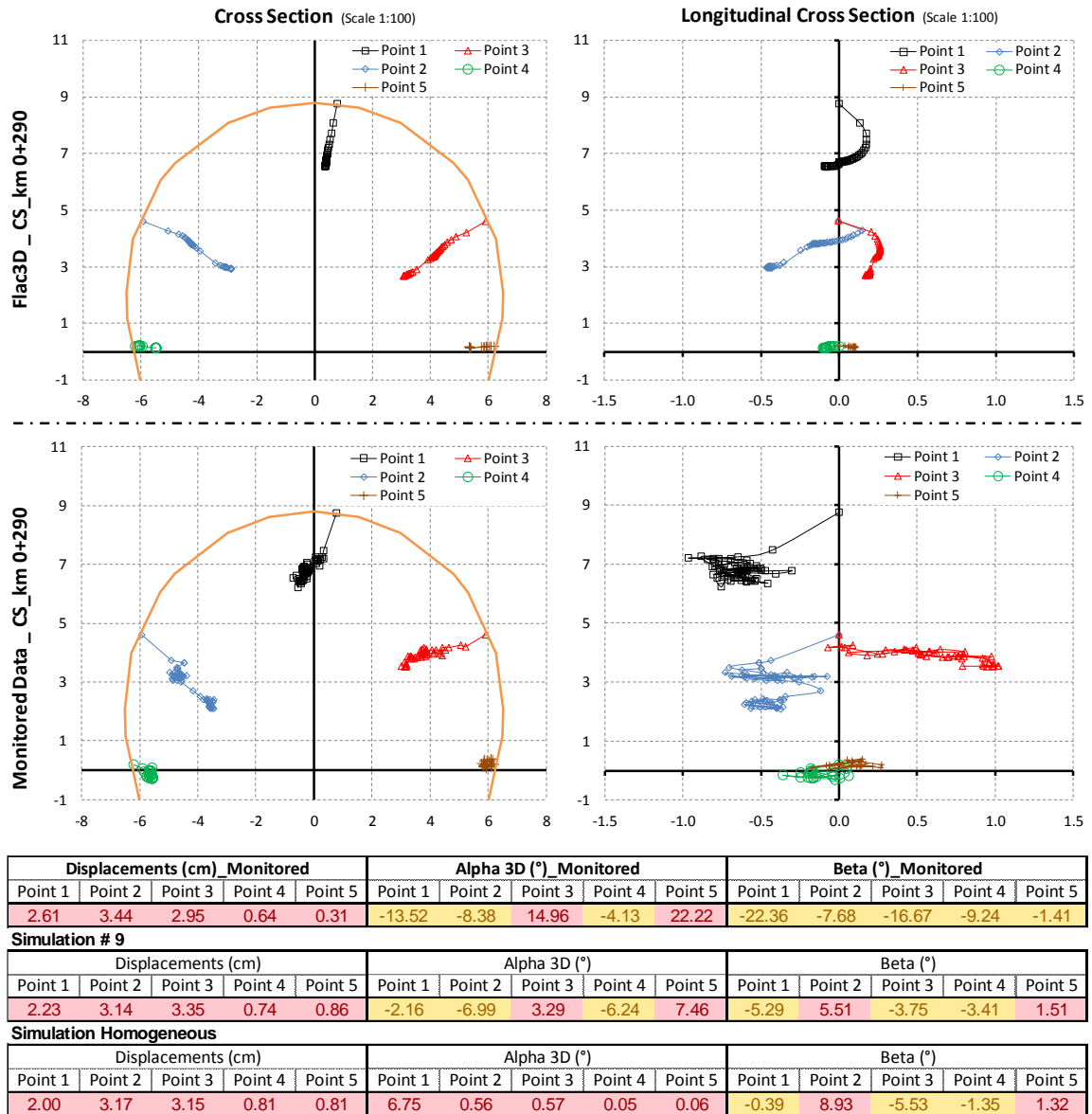


Fig. 34: Comparison monitored data vs. numerical model results, cross section: km 0+290

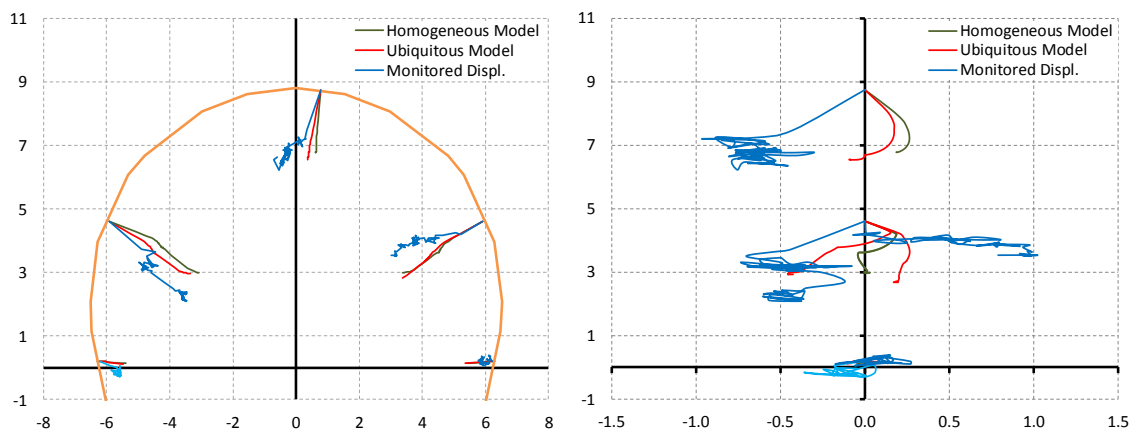


Fig. 35: Galgenberg tunnel displacements, cross section: km 0+290

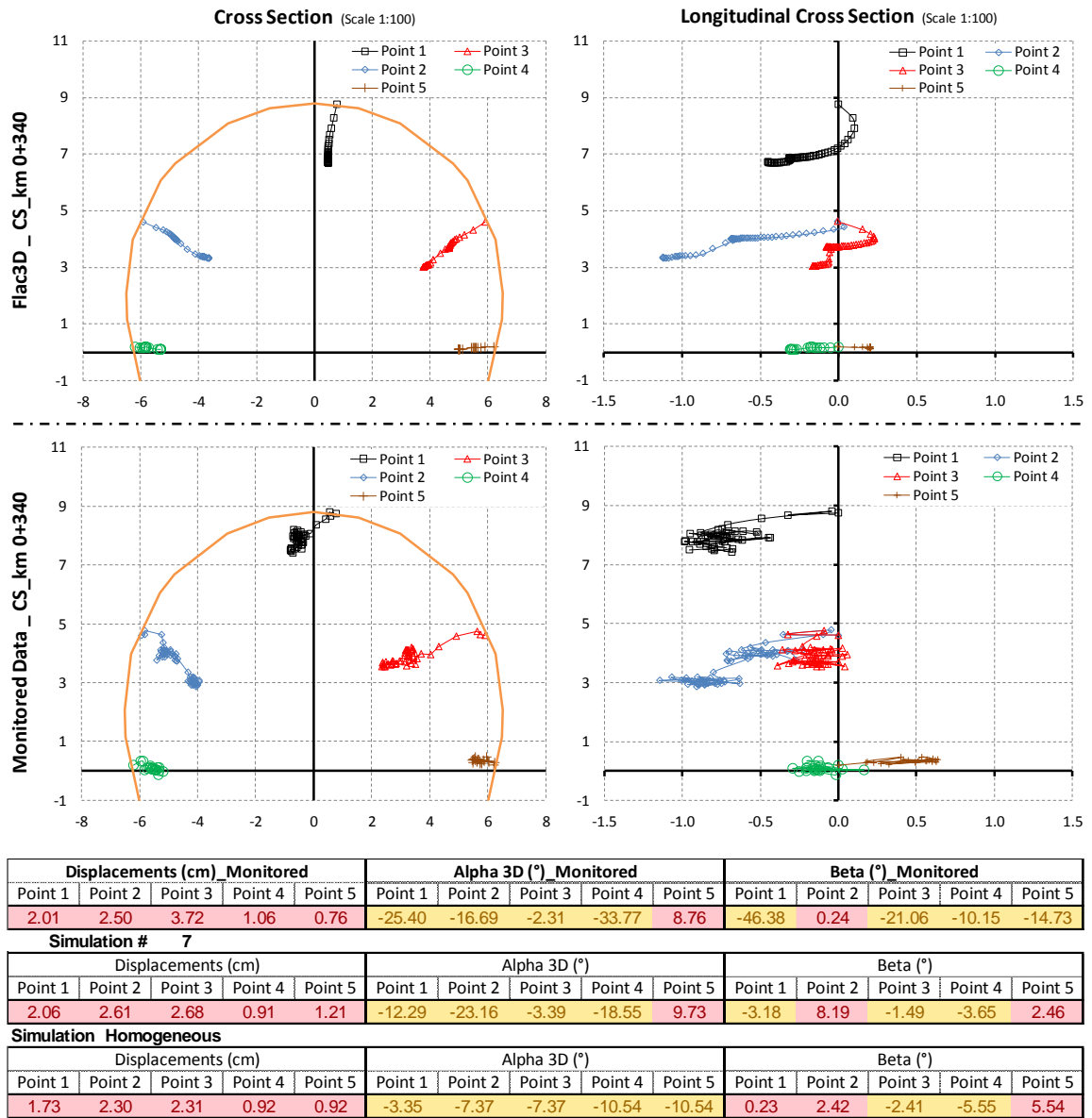


Fig. 36: Comparison monitored data vs. numerical model results, cross section: km 0+340

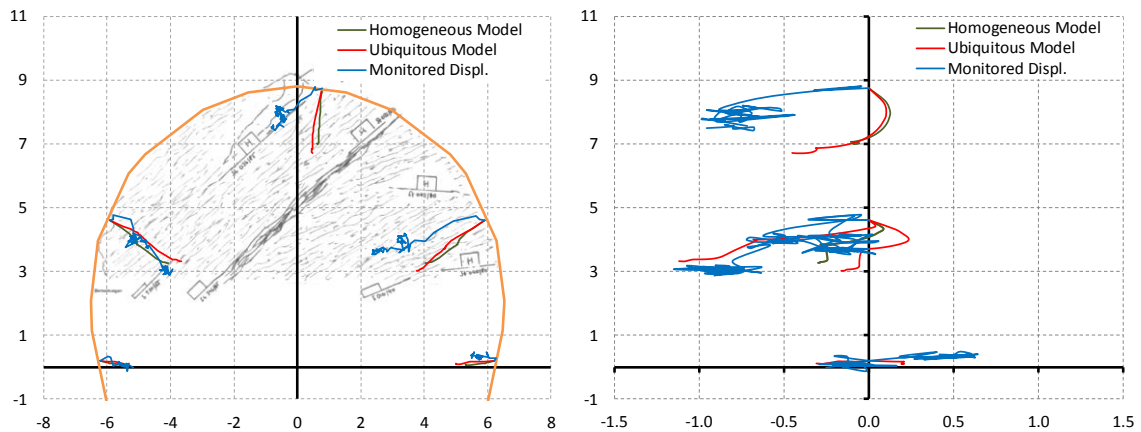


Fig. 37: Galgenberg tunnel displacements, cross section: km 0+340

The aim of the validation was to assess the capability of the numerical model in terms of constitutive model, dimensions and mesh configuration. This was successfully reached after verifying 2 different cross sections of the Galgenberg tunnel in which, excavation sequences, implemented support, and geological features for the cross sections were carefully recorded during construction. The displacements were systematically recorded, in a global coordinate system, allowing the calibration to take place. The studied cross sections comply with the requirements of the constitutive model described in section 2.3.2 in terms of material properties, boundary conditions and a single weakness plane influencing the ground behavior.

4. NUMERICAL MODEL RESULTS

The last section has shown the capability of the numerical model to represent, under certain conditions, the ground behavior of rock masses influenced by weakness planes.

According to the flow chart presented in Fig. 18 the implementation starts with the numerical model assembly followed by the definition of the weakness plane (weakness plane) orientation through a dip and dip direction. The implementation is completed with the allocation of material parameters (rock mass and weakness plane) and the simulation of the excavation. The numerical model meshing and geometry remain unchanged throughout the process, whereas weakness planes orientation, as well as material properties vary depending on the addressed subject.

More than 400 simulations were performed during this study. It is important to keep in mind that 10-15% of the simulations are not included into the final result as the output results do not comply with the ubiquitous joint model restriction presented in chapter 3.

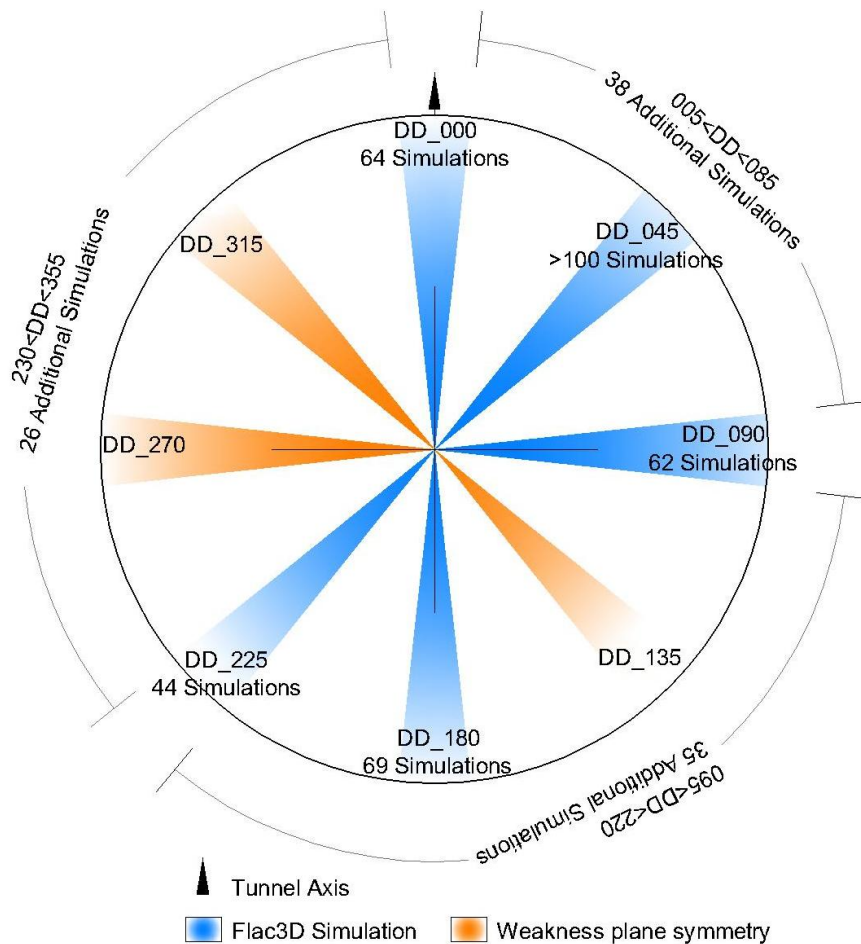


Fig. 38: Performed simulations summary

Fig. 38 summarizes the performed simulations in a coordinate system. Note that the figure only illustrates the weakness plane dip direction (it does not include dip angles). The tunnel axis for all simulation is orientated to the north with a trend of 000 and plunged 00.

Through the figure it is possible to visualize the performed simulation as well as assumption made based on the analysis of the results. On the one hand the blue highlighted areas indicate the weakness plane dip direction used as an input value for the Flac3D simulations. On the other hand, the orange areas indicate dip directions for which results can be indirectly evaluated based on the weakness plane symmetry of the blue highlighted areas. Such behaviors as well as areas in between are further studied, corrected and/or confirmed through multiple simulations performed in the orange areas and between the blue and orange areas.

Results are presented in two parts: The first part of the study deals with the weakness plane orientation, in terms of dip and dip direction, and the influence that different orientations and dip angles have on the ground behavior (section 4.1) and the second part focusses on trend determination and the variation of ground behavior due to changes in material properties, initially the influence of the rock mass properties is assessed, followed by the influence of varying weakness plane's properties (section 4.2).

Although results are divided into sections there is a coherent interaction between material parameters and weakness place orientation that is addressed throughout the results. The three sections present an analysis and comparison of results, later summarized and extended in chapter 5.

The two sections (section 4.1 and 4.2) make use of the reference values shown in Table 9. The values were chosen based on properties from laboratory results for foliated rock masses (phyllites as intact rock) where the weakness plane controls the rock mass behavior. In the first section the values are fixed while the weakness planes' orientation and dip angle vary and on the second section the orientation and/or dip angle remain fixed while the properties of the matrix and weakness plane vary within certain ranges.

REFERENCE VALUES UBIQUITOUS-JOINT MODEL			
Matrix property	Value	Weakness plane (WP) property	Value
Elastic bulk modulus	800 MPa	Joint cohesion	1 MPa
Cohesion of matrix	10 MPa	Joint dilatancy	0 °
Dilatation of matrix	0 °	Joint friction angle	20 °
Fric angle of matrix	30 °	Joint tension limit	0.001 MPa
Elastic shear modulus	480 MPa	Orientation:	
Tension limit of matrix	2 MPa	WP. Dip Direction	varies
		WP. Dip	varies

Table 9: Input parameters

4.1. Variation of Weakness Plane Orientation

The results are divided into three parts: 1st the variation on radial and tangential displacements and beta angle is assessed. For this purpose it is use a cross-section towards the excavation (plane Z-X plane), 2nd In order to evaluate the alpha angle variation, displacement are plotted and analyzed in a longitudinal section (plane Z-Y) and 3rd the assessment of displacements ahead of the face (pre-displacements) and displacement development. All planes and conventions are summarized in Fig. 20.

The variation on dip direction is made in order to cover all possible areas where weakness planes could influence the displacement behavior. The variation is based on the stereographic projection of a plane by varying the dip direction, which dictates the direction of the plane, in 45 degrees increments. As previously mentioned, the starting point is dip direction 000, symmetry for weakness planes is assumed and simulation in between were conducted in order to confirm or reevaluate observed trends.

Approximately 40% of the simulation displayed in Fig. 38 were conducted aiming to evaluate the influence of the weakness plane orientation, a combination of material and joint properties were set as fixed (Table 9) and a variation of the mentioned angles was performed.

4.1.1. Dip direction 000

The orientation of the weakness plane is dipping in the direction of the excavation (dip direction 000, as shown on left hand-side of Fig. 39). The following dip angles were studied for this specific dip direction: 20°, 30°, 45°, 60°, 75° and 90°.

Initially two different stress conditions were studied ($\sigma_1=6.25\text{MPa}$ and $\sigma_1=12.5\text{MPa}$) in which no significant variations, regarding trends, were detected on the displacement behavior for a fix value of lateral pressure coefficient k_0 equal to 0.5.

Changes in the radial displacement magnitude are the only noticeable parameter in the cross section (Z-X plane). Displacements magnitude is inversely proportional to the dip angle. The highest displacements values (including displacements ahead of the face) are reached for a dip angle of 0° and the lowest values were detected for a dip angle of 90°, which displacements tend to be equal to the homogenous model.

Plasticity state plots show multiple elements reaching shear and tensile envelope (plastic state), mainly on the tunnel crown, for a weakness plane dipping 20°. The stress magnitude decreases to a minimum for a dip of 90°. The described behavior is also detected in the stress increment plot where high concentration of stresses can be seen at the tunnel's crown.

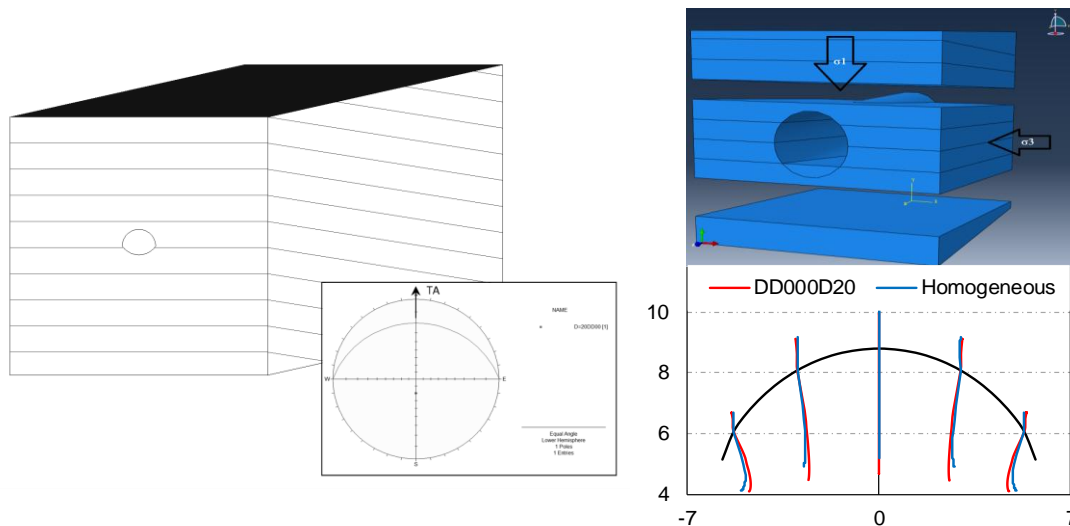


Fig. 39: Example DD000/Dip20 (left) and beta vs. homogenous models results (right)

As expected, in the cross section (Z-X plane) minor variation on the beta angle can be detected when compared with the homogeneous model. As the weakness plane dips in the same direction of the excavation, beta displays some counter-clockwise rotation (in comparison with the homogenous model) for the left side-wall and clockwise for the right side-wall (right hand-side of Fig. 39). Comparing the stress plots for the two studied stress conditions it was observed that this behavior is controlled by σ_3 on the weakness plane.

The longitudinal section (Z-Y plane, displacement plot) is for this case an appropriate plot to display the weakness plane influence on the displacement behavior. The behavior is framed by a remarkable alpha rotation against the excavation to a lowest value for a weakness plane dipping 20° . As the dip angle increases the vector rotates to positive values (towards the excavation direction) up to a maximum rotation between a dip angle of 45° and 60° , depending on the observed monitoring point (e.g. maximum rotation of monitoring point P1 takes place for dip angle equal to 45° , whereas maximum rotation is achieved for point P16 and P17 at a dip angle of 0°). From this dip angle on, the vector rotates back towards the initial values.

The left hand side of Fig. 40 displays the described alpha angle variation for the monitored points along the intrados (stress level $\sigma_1 = 6.25\text{MPa}$). The right hand side of the figure displays the above mentioned behavior for the crown monitoring point (P1). It also shows the displacement development including pre-displacements, of which percentage of the total displacements is lowest for a dip angle of 20° , increases up to a maximum of approximately 40%, for a dip angle equal to 45° and returning to relative low values for a dip angle of 90° , note that not only the percentage but also the development of pre-displacements varies depending on the dip angle inclination as seen in Fig. 42.

The same described behavior remains independent of the stress level. It is evident that there is a difference on alpha rotation when comparing the crown and the side-walls (for DD000) as for the crown vector displays a greater rotation that those register on the side-wall. Such difference decreases as seen in Fig. 41, where it can be seen the flattening of the vector and decrease of its rotation as the stress

level increases for the evaluated stress magnitudes $\sigma_1=12.5\text{MPa}$, $\sigma_1=18.75\text{MPa}$ and $\sigma_1=25\text{MPa}$.

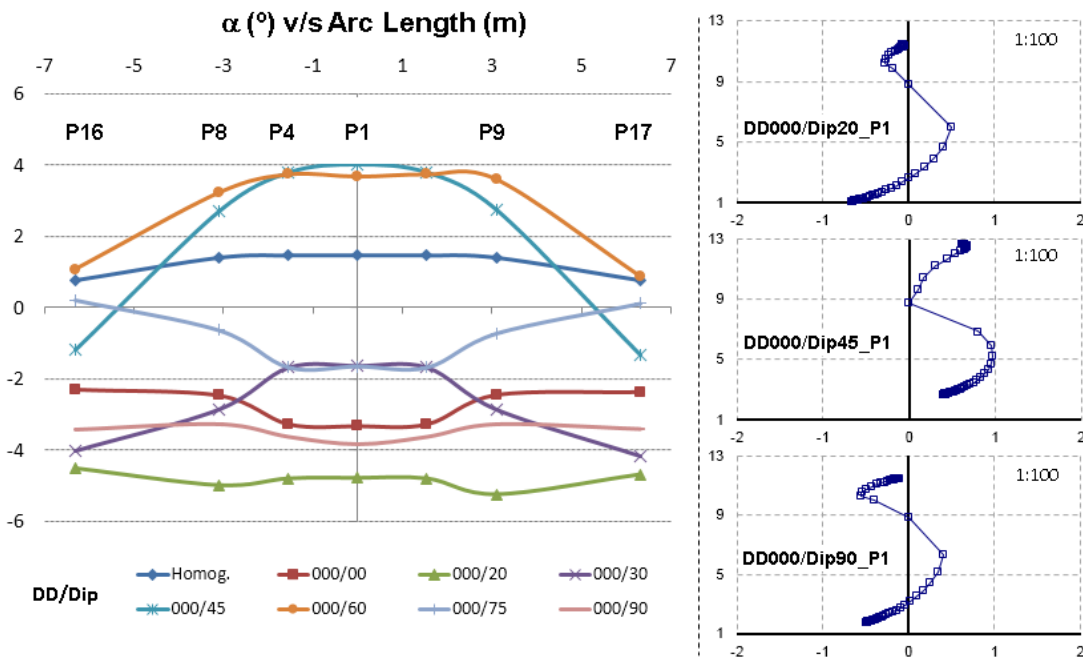


Fig. 40: Alpha results DD000 ($\sigma_1=6.25\text{MPa}$) and longitudinal cross section

Note that a relative large number of results from the highest evaluated stress magnitude σ_1 equal to 25MPa had to be discarded since the results and seen contour plots register large shearing along the weakness plane. The described condition, for the implemented constitutive model, leads to overestimation of displacements (section 2.3.2).

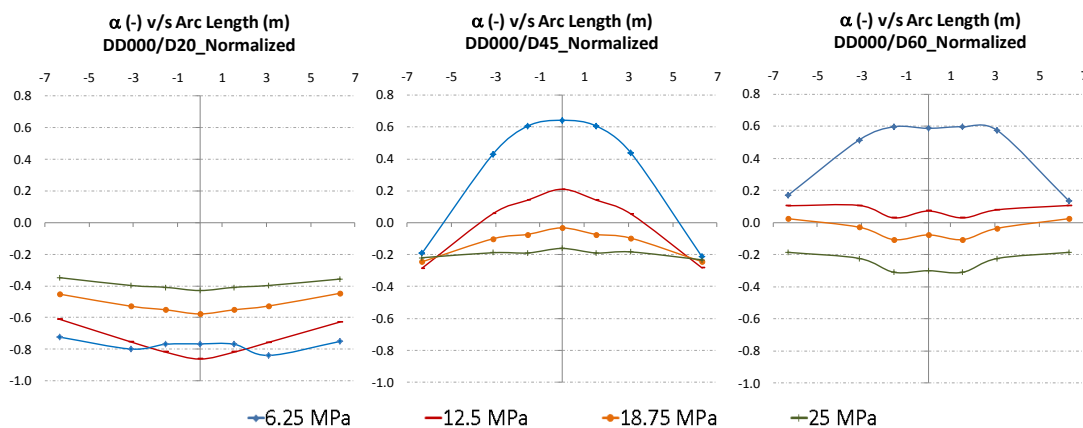


Fig. 41: Alpha results DD000

As previously mention, there is a dependency on the displacement development with the inclination of the weakness plane, the tunnel closure plot (Fig. 42) shows such dependency. The most notable result displayed by the figure, is the increment of pre-displacements with the dip angle to a maximum percentage for a weakness

plane inclination close 45° . From this dip angle on, the percentage ahead of the face decreases.

Note that Fig. 42 contemplates a vertical stress of 12.5MPa. The mentioned dependency is observed for all analyzed stress conditions. However, there is a particularity observed on the side-wall, exhibiting a similar variation to the one shown by alpha where higher stress levels divert the pattern by displacing the higher percentage of displacements ahead of the face to an inclination of the weakness plane close to a dip angle of 60° .

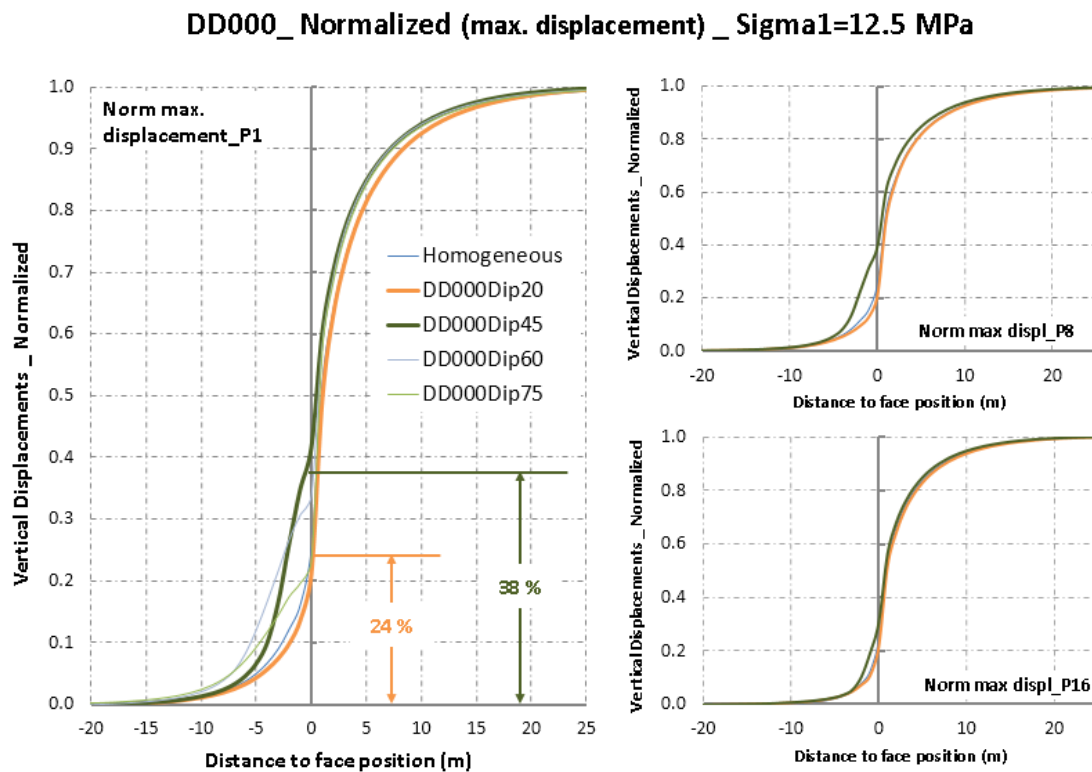


Fig. 42: Normalized tunnel closure vs. distance to the face

4.1.2. Dip direction 180

The orientation of the weakness plane is dipping against the excavation on a straight angle (dip direction of 180), as seen on the left-hand side of Fig. 43.

Weakness planes dipping against the excavation are often labeled as “unfavorable” (section 2.2.3). However, classifications systems usually do not include further details on the cause of the unaffordability or describe its effect on the ground behavior. The studied dip angles were aimed to assess the source and critical angles where the ground behavior is strongly influenced by the weakness plane. Studied dip angles are 00° , 20° , 30° , 45° , 60° , 75° and 90° .

As previously implemented for a DD000, a total of 4 stress conditions were studied (vertical stress σ_1 equal to: 6.25MPa, 12.5MPa, 18.75MPa and 25MPa) with a fixed lateral pressure coefficient k_0 of 0.5.

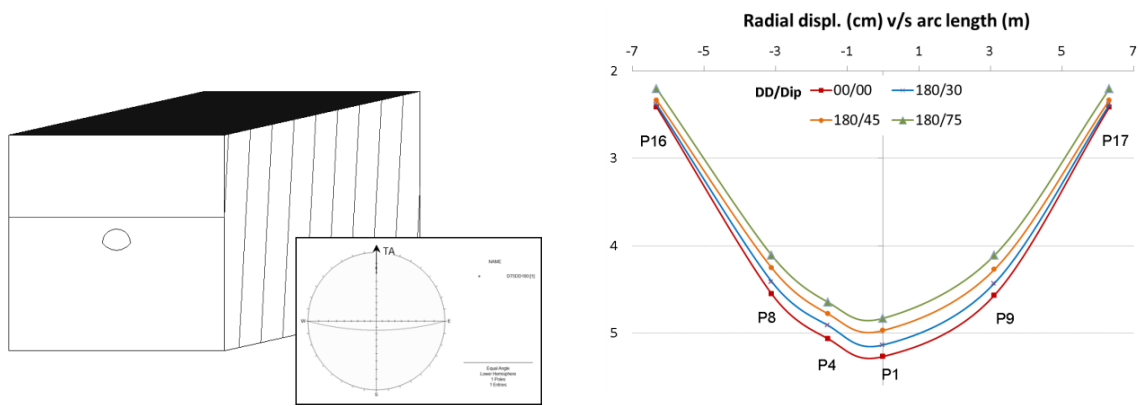


Fig. 43: Example DD180/Dip70 (left) and radial displacements DD180 (right)

Changes in radial displacement magnitude for DD180 show a similar behavior as the one displayed for a DD000, the magnitude is inversely proportional to the dip angle, reaching a maximum value at a dip angle of 20° and decreases for steeper angles to minimum displacement observed at a dip angle of 90°.

Beta rotation follows the same pattern observed for weakness planes dipping towards the excavation. Displacement vector rotates clockwise for the right side-wall and counterclockwise for the left side-wall, showing the behavior plotted in Fig. 39.

The weakness planes influence on the displacement behavior is clearly seen in the longitudinal section presented in Fig. 44 (Z-Y plane). The figure compares 3 different dip angles and allows a proper visualization of the weakness plane influence on alpha.

The vector rotates against the excavation to a lowest value found at a dip angle equal to 20°, value in which maximum displacements take place for DD180, as the dip angle increases the vector rotates to positive values (towards the excavation direction) up to a maximum rotation for an inclination close to 45°, from this dip on, the vector rotates back towards the initial values close to the ones register for a dip angle of 20°, Fig. 44 shows the described behavior for the crown monitoring point (P1) in blue and the right side-wall (P17) in green.

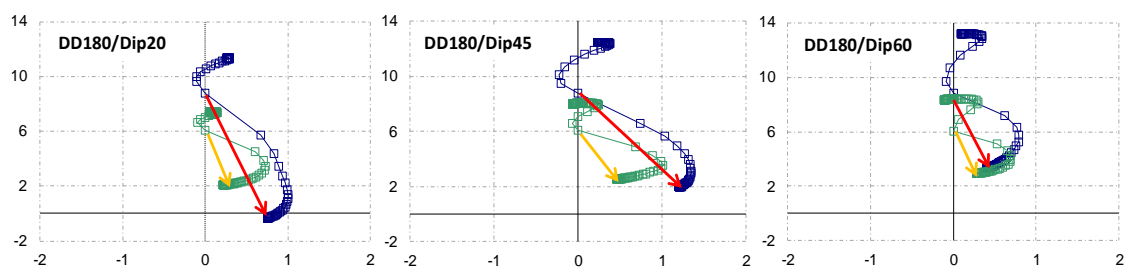


Fig. 44: Alpha results DD180 ($\sigma_1=12.5\text{MPa}$). Longitudinal section, displacements scale 100:1

The vector tends to be orientated towards the excavation, the behavior differs from the one observed for a dip direction 000 in which the vector is orientated against the excavation for low dip angles (Fig. 41). Additionally, the trend shown by this dip direction, unlike the behavior shown for DD000, is steady and does not display a variation in terms of rotation trend for the analyzed stressed levels σ_1 equal to 6.25MPa, 12.5MPa, 18.75MPa and 25 MPa (Fig. 45).

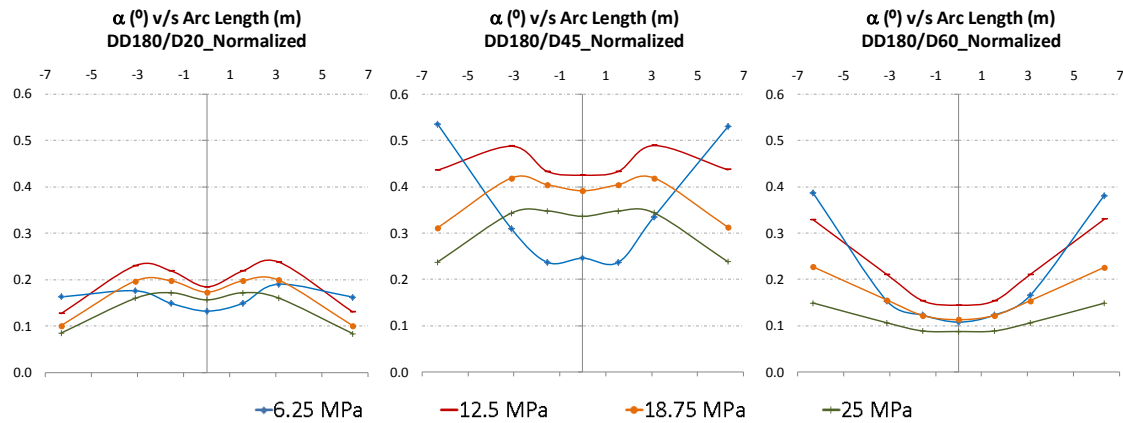


Fig. 45: Alpha results DD180 for σ_1 equal to 6.25MPa, 12.5 MPa, 18.75 MPa and 25 MPa

Fig. 45 shows that, for the studied stress level conditions, weakness planes have a greater influence on the side-wall monitoring points (P8, P9, P16 and P17) with increasing stress magnitude.

Fig. 46 shows the longitudinal stress component (YY) for two different stress conditions. As expected, a larger influenced area is displayed for a stress conditions σ_1 equal to 25MPa, the figure also shows that both cases register high stress concentration on the side-walls close to the face, causing the reorientation of the vector.

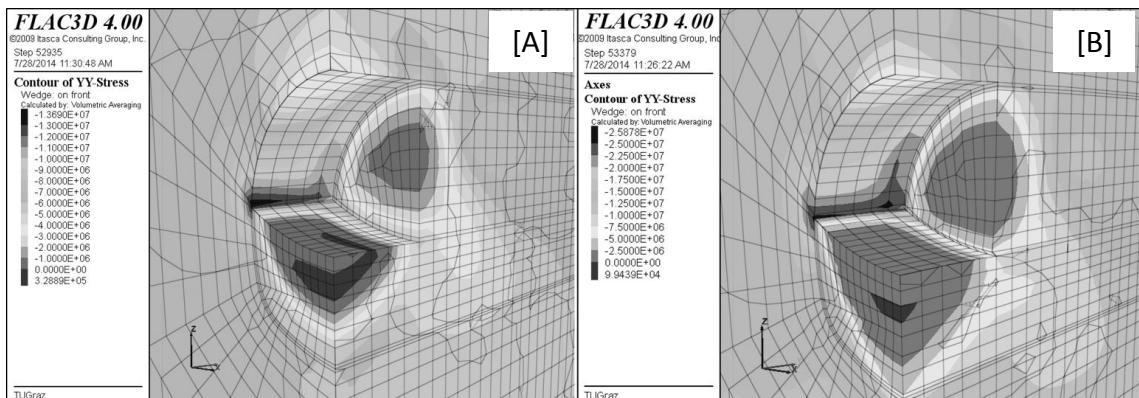


Fig. 46: Stress YY redistribution for DD180Dip60 A) $\sigma_1 = 12.5$ MPa and B) $\sigma_1 = 25$ MPa

Comparing the two cases studied in this section (DD000 and DD180) notable differences of the ground behavior were observed, mainly regarding magnitude of

displacements, alpha angle orientation and behavior of displacements ahead of the face (pre-displacements).

Radial displacements, influenced by weakness planes orientated towards the excavation, are for all monitored points minor than those oriented against the excavation. However, as seen in Fig. 47 the mentioned pattern only applies for dip angles below 45°, steeper deep angles (>45°) display the opposite behavior yielding larger displacements for weakness planes orientated towards the excavation.

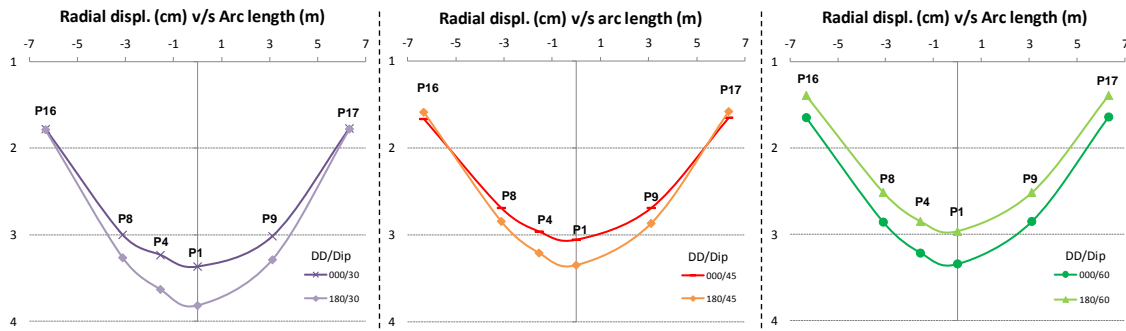


Fig. 47: Radial displacement variation for DD=000 and DD=180

The weakness planes' DD180 influence on the 3D displacement vector (alpha angle and magnitude of displacements) is framed by a clear orientation of the vector towards the excavation (positive values), the trend is steady for all dip angles and stress conditions, whereas for DD000 the vector tends to display negative values, reaching a minimum for a dip angle of 20° (Fig. 48).

Some exception to the previously described pattern was observed for weakness planes orientated towards the excavation (DD000) in combination with a stress condition $\sigma_1=6.25\text{MPa}$ and $\sigma_1=12.5\text{MPa}$. For these cases alpha reaches positive values for plane dipping 45° and 60°. In general terms the angle is reoriented mainly by dilation perpendicular to the weakness planes and, in some cases, by shearing along the planes.

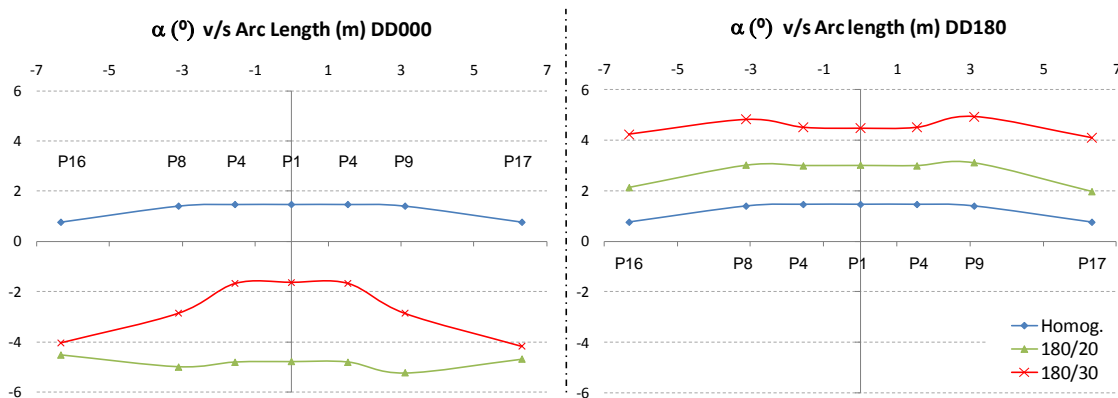


Fig. 48: Alpha variation results for DD=000 and DD=180

Displacements ahead of the face (pre-displacements) highly depend on the orientation of the weakness plane. For DD000 the displacement development curve shows a greater percentage of pre-displacements, than those for DD180. Fig. 49 compares displacement development for tunneling through a rock mass with a weakness plane dipping 45° towards (DD000) and against (DD180) the direction of the excavation; the difference in terms of pre-displacements, for this specific case is close to 10%.

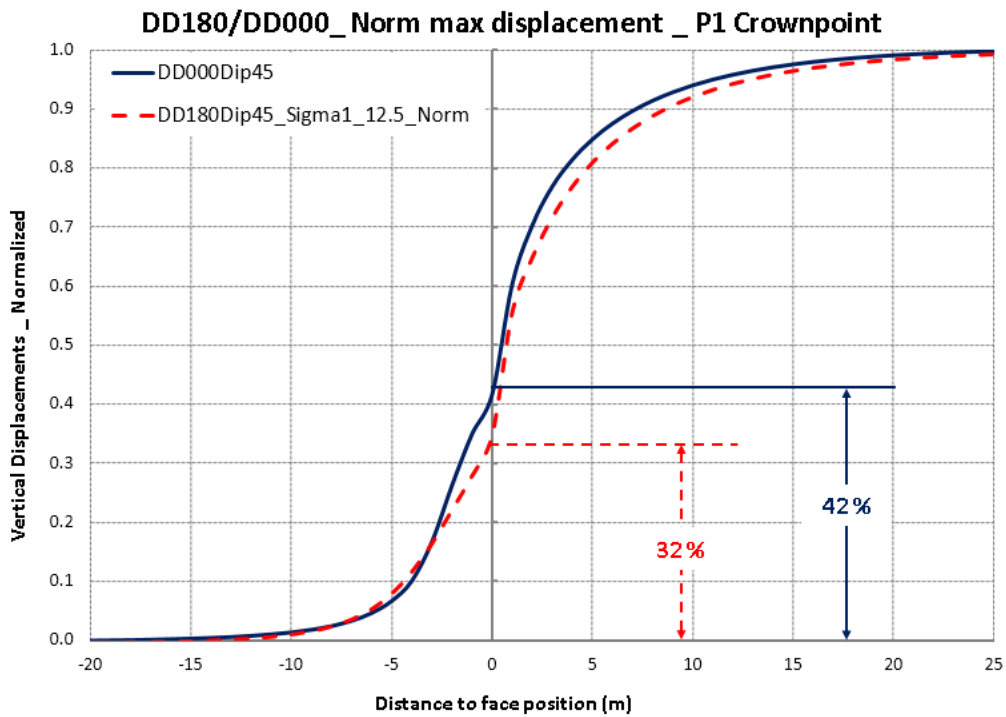


Fig. 49: Displacement development for tunneling towards and against the weakness plane orientation

Flac3D SYY stress plot (Fig. 50), for tunneling against the weakness plane orientation (DD180), displays a substantial stress magnitude variation at the tunnel's crown on the plane parallel to the tunnel axis (plane YZ).

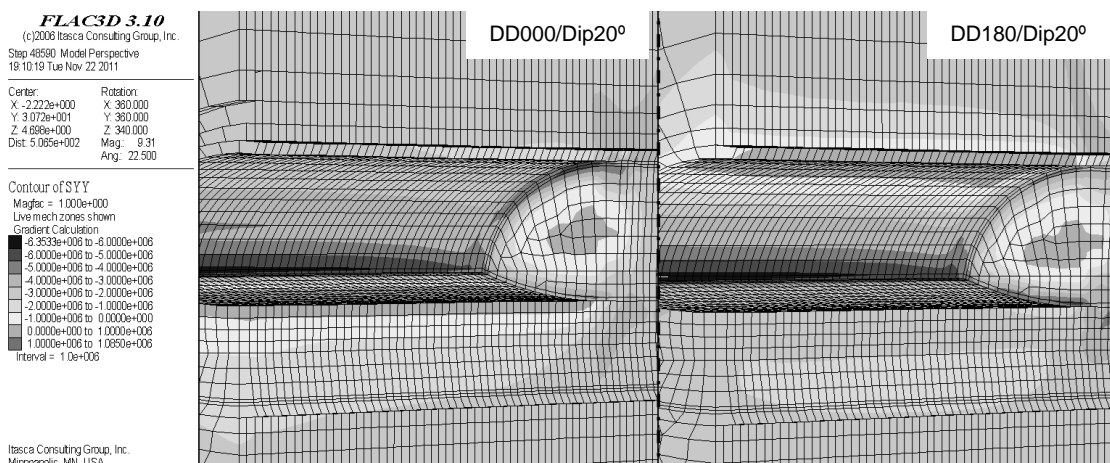


Fig. 50: Flac3D_SYY results for DD000D20 and DD180D20

4.1.3. Dip direction 090

Although the numerical simulations were done for a dip direction of 90° (DD090) symmetry for a weakness plane is expected. Therefore the described results apply for both cases in opposite side-wall, e.g. displacements in the right side-wall for DD090 can be interpreted as displacements in the left side-wall for DD270. As shown in Fig. 38, multiple simulations for the symmetric weakness plane were performed to confirm the symmetrical behavior of the planes.

A perpendicular plane to the tunnel axis (plane Z-X) presents an appropriate overview of the weakness plane influence with dip direction 090 on the displacement behavior. For this case, opposite to the case studied in the last section, discontinuities have an evident stronger influence on the beta angle rotation.

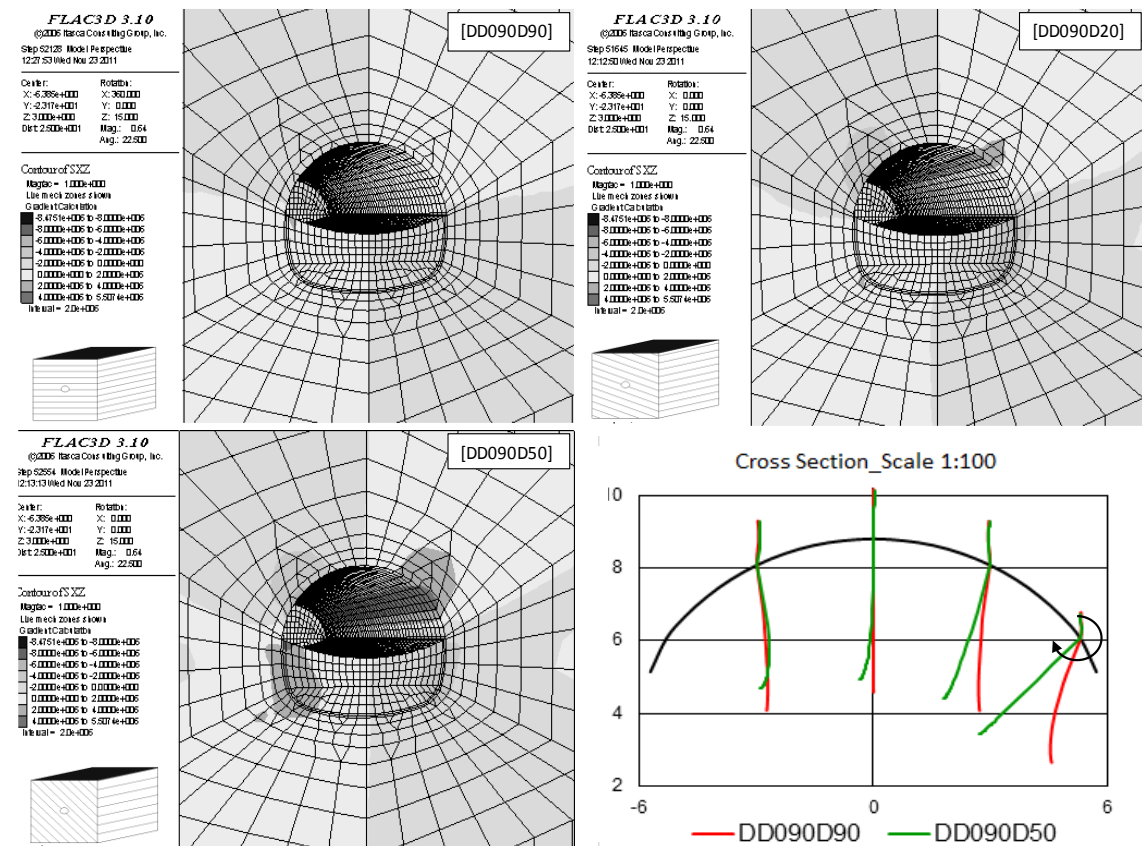


Fig. 51: Flac3D_SXY results for DD090D90, DD090D20 and DD090D50

The displacement vector on the right side-wall tends to rotate clockwise (decreasing tangential displacements) up to a maximum rotation for a weakness plane dipping approximately 50°. As the weakness planes' dip angle increases, the vector rotates to its initial position, similar to the one observed for a dip direction 090 and dip angle of 0°. The left side-wall and intermediate points show similar behavior, but with much lower magnitude. The described behavior can be seen in Fig. 51 and Fig. 52 which present the shear stress plot -SXZ- and the ubiquitous model state plot respectively.

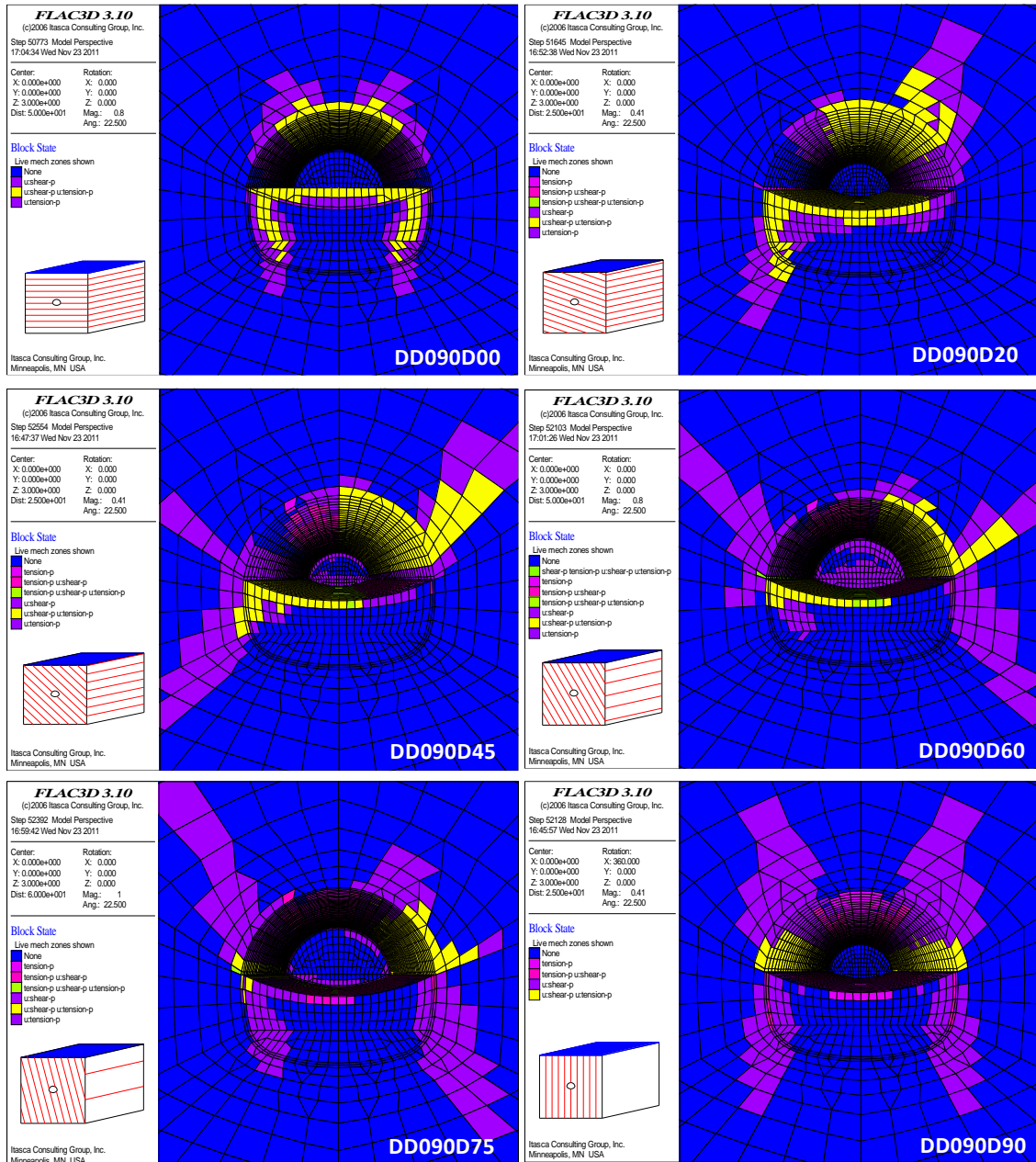


Fig. 52: Flac3D ubiquitous block state plot for DD90

Entailed in Fig. 52 is the failure mechanism of planes orientated parallel to the tunnel axis (DD90), failure is displayed as shearing along the planes (see elements highlighted in yellow). Starting at a dip angle of 20°, shearing of the weakness planes roughly follows the dip angle orientation (see results shown in Fig. 52 for dip direction 45°, 60°, 75° and 90°). Shearing along the weakness planes and consequently the displacements magnitude perpendicular, or along, the plane's surface, strongly depend on the dip angle.

A similar behavior to the one observed for beta in a X-Z plane, was also identified for the angle alpha. Its rotation against the excavation increases from a dip angle of 20° up to a maximum rotation for a dip of 50°; once this threshold angle is reached the vector rotates back towards the excavation to a final value, at a dip angle equal to 90°, similar to the homogeneous model. The described behavior is

displayed in Fig. 53, Note that the lower part of the figure shows the displacement behavior, in the cross section and longitudinal section, for DD090 and dip angles of 20°, 45°, 75° and 90°.

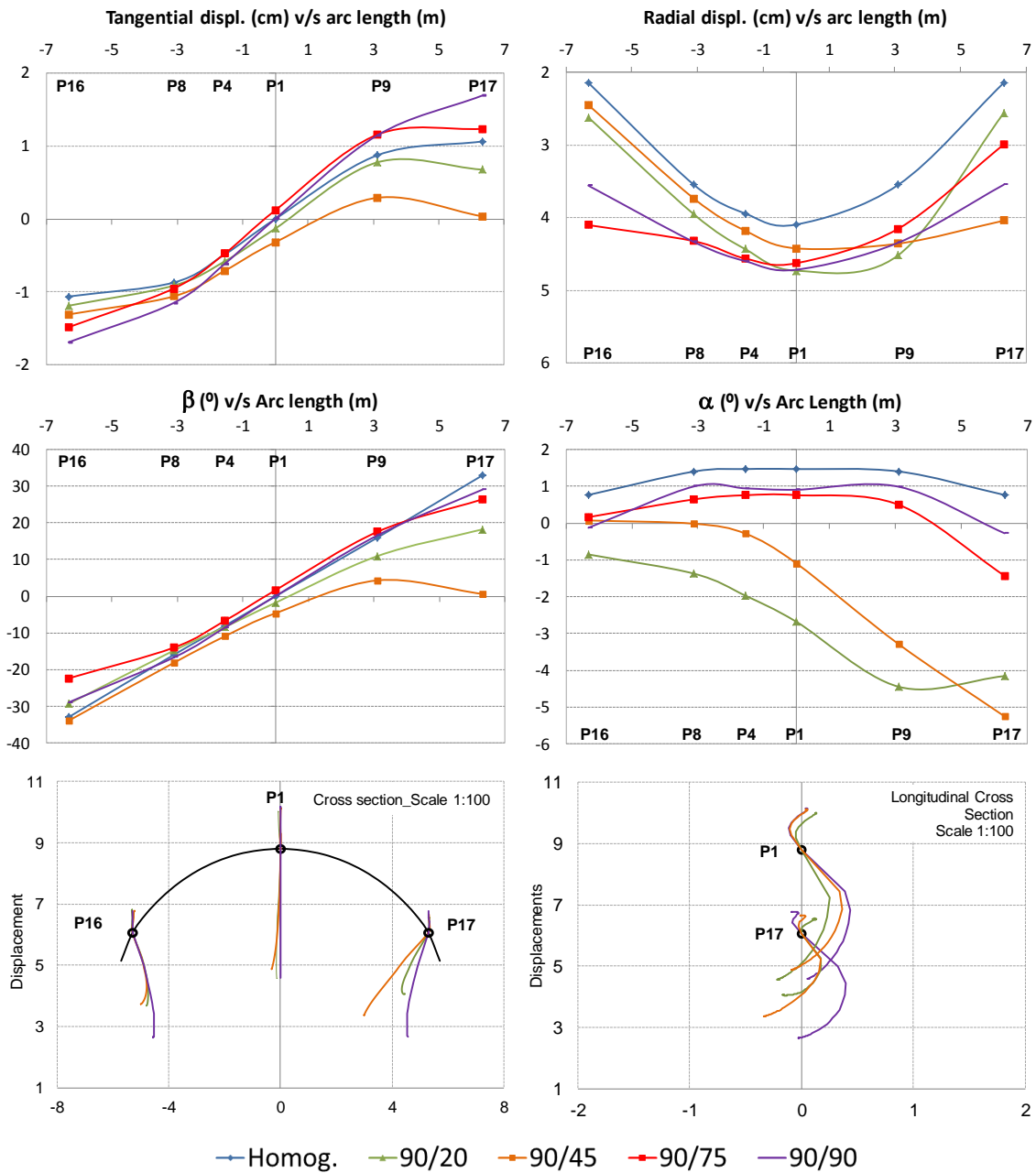


Fig. 53: Alpha and beta results for DD090 ($\sigma_1 = 6.25\text{MPa}$)

The longitudinal section (Y-Z plane) shows the weakness plane influence on alpha. On the left side-wall the vector has a similar behavior to the one exhibited by the homogeneous model, while the monitored points towards the right side-wall show a higher alpha angle influence yielding negative values, in other words, a reorientation against the direction of the excavation.

As previously seen, the presence of weakness planes parallel to the tunnel axis has its main influence on the side-wall where the planes show a quasi-tangential intersection with the excavation. The opposite side displays a weakness plane influence for larger dip angles (approximately $>60^\circ$).

A distinct pre-displacement behavior involving the right side-wall was observed for this deep direction. Fig. 54 presents the percentage of pre-displacements for the crown (Point 1) and the right side-wall (Point 17), the figure includes different dip angles and three different stress conditions. The common denominator for point 17, independent of the stress magnitude, is the low pre-displacement values for discontinuities dipping between 30° and 60° .

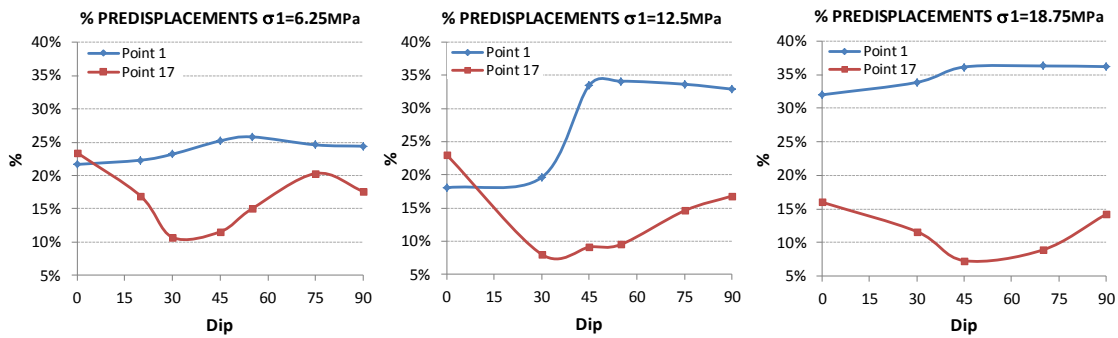


Fig. 54: Percentage of displacement ahead of the face for DD090

The following figure shows the pre-displacements variation along the tunnel’s arch length for a weakness plane dipping 45° . The figure clearly displays a pre-displacements decrement towards the right side-wall.

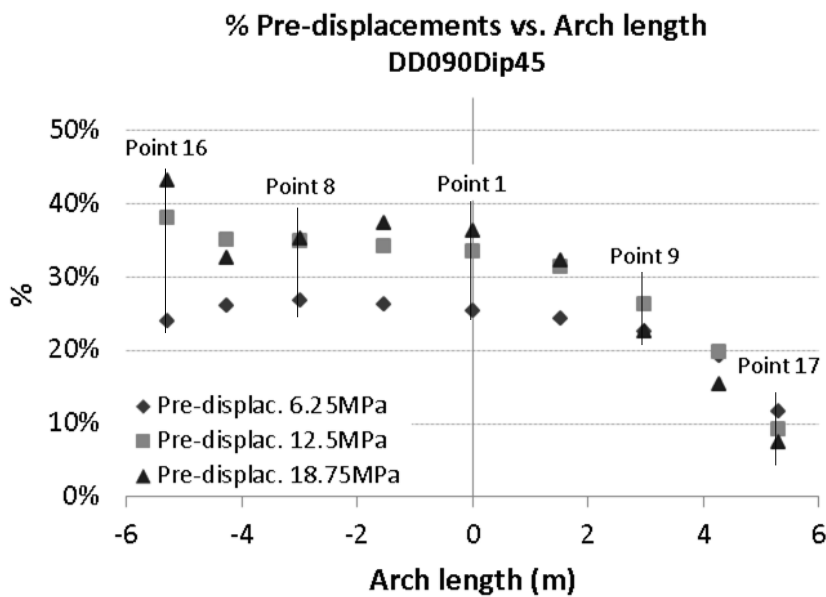


Fig. 55: Variation of displacement ahead of the face for DD090Dip45

4.1.4. Dip direction 045

Numerical simulations were performed for a dip direction equal to 45° (DD045), it is expected that the symmetric plane (DD315) displays the same behavior on the opposite side-wall. Therefore the described results apply for both dip directions (DD045/DD315) on opposite side-wall, e.g. clockwise beta rotation on the right side-wall for DD45 should be interpreted as a counter clockwise rotation on the left side-wall for DD315. Fig. 38 shows the multiple simulations performed in order to confirm the symmetrical behavior of the planes. Multiple dip angles and a total of 4 different stress conditions were evaluated to properly assess the behavior of the excavation.

The displacement behavior seen for DD090 can be roughly observed for DD045. Alpha behavior on the right side-wall for DD045 shows a rotation away from the excavation up to a maximum rotation/angle close to a dip value of 45° , after this peak angle is reached the vector rotates back towards the excavation, the behavior was detected for all monitored points with different magnitude.

The displacement vector directly depends on the longitudinal displacements (plane parallel to the tunnel axis). Fig. 56 shows the variation of longitudinal displacements for a dip direction 045 and different dip angles (sigma1 equal to 12.5MPa). The figure clearly displays the behavior previously described, yielding maximum values for a weakness plane with DD045 and a dip angle equal to 45° .

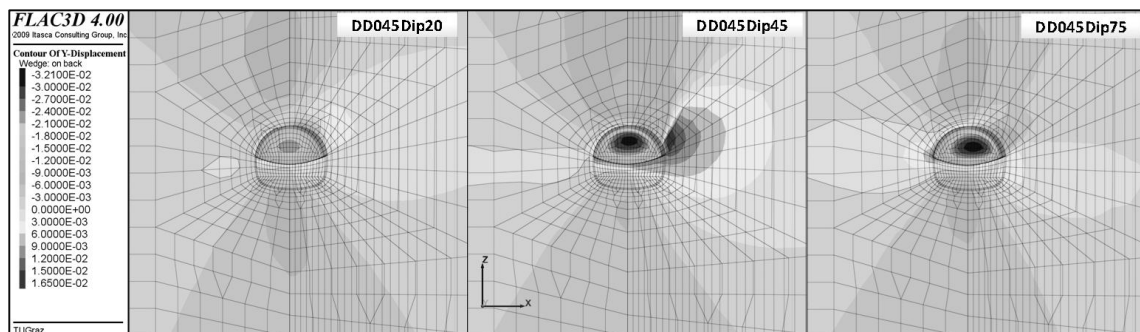


Fig. 56: Longitudinal displacements for DD045

Considering the homogeneous model as a benchmark, there is a notable behavior variation on the side-wall where the weakness plane quasi-tangentially intersects the excavation. It was observed that tangential and radial displacements increase on the right side-wall, similar to the behavior registered for DD090, however, independent of the stress condition, all dip angles display smaller displacements for DD045 than DD090.

The above described behavior can be seen in Fig. 57 which displays radial and tangential displacements along the arch length (intrados), for different dip directions and dip angles. The upper part of the figure shows the radial displacements tendency to increase as the dip direction rotates DD000 to DD090, in relation to the tunnel axis.

The tangential displacement plot, lower part of Fig. 57, shows an increase of tangential displacements, mainly on the right side-wall, as the dip direction rotates from DD000 to DD090.

Note that the maximum tangential displacements are registered for DD090, such displacements are directly related to the rotation of beta, previously described for the right side-wall, and it is in agreement with the previous observation regarding parallel planes yielding maximum displacement values.

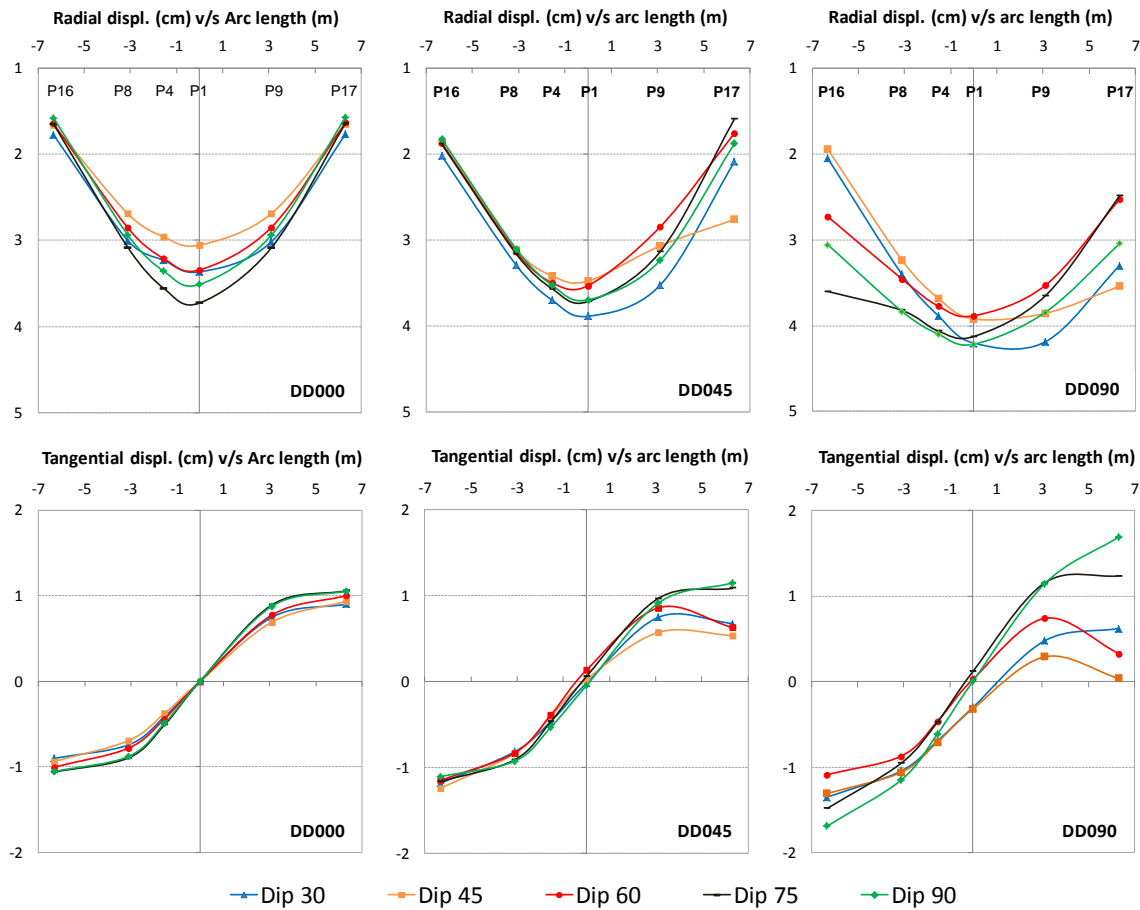


Fig. 57: Radial and tangential displacements for DD000, DD045 and DD090 ($\sigma_1=6.25\text{MPa}$)

No significant alpha rotation was detected on the crown monitoring point. On the other hand DD045 displays an important alpha rotation against the direction of tunneling, on the right sidewall displaying a maximum rotation for a dip angle of 45°

Displacements ahead of the face, for the DD045, displayed a similar behavior to the one observed for DD090 where, in general terms, displacements on the right side-wall are significantly lower than those registered on the crown and left side-wall. This behavior remains constant up to a dip angle between 45° and 50° , steeper dip angles ($>50^\circ$) display the opposite trend with lower percentage of displacements ahead of the face on the left side-wall. This behavior was also observed for dip direction 090; however, the mentioned change of trend takes

place at a steeper dip angle (above 75°) as seen in Fig. 58. This behavior was recorded for all assessed stress conditions.

The previously described change of trend takes place as the weakness plane orientation aligns with an imaginary line between the tunnel center and the monitoring point on the left side-wall (point 16), the alignment occurs at lower dip angle for DD045 than for DD090.

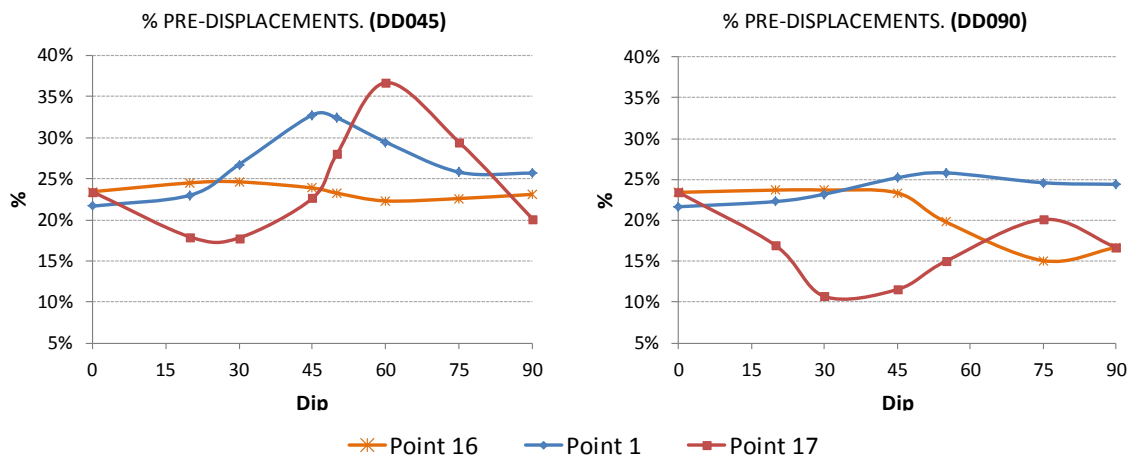


Fig. 58: Percentage of displacements ahead of the face for DD045

4.1.5. Dip direction 225

Numerical simulations were performed for dip direction equal to 225 (DD225), weakness plane symmetry is expected and proved through multiple simulations for DD135, similar to the previous cases; the described results apply for both cases on the opposite side-wall. Fig. 38 shows the number of simulations performed in order to assess the behavior of the weakness planes. The assessment of this dip direction was made for 4 different stress conditions and multiple dip angles (dip: 20° , 30° , 40° , 45° , 50° , 60° , 75° and 90°). The results presented in this section also attempt to compare previously described results aiming for a behavior changes overview for different dip directions.

It was previously seen (Fig. 47) that weakness planes striking against the direction of excavation (DD180) yield higher displacements for dip angles lower than 60° and higher displacements for steeper dip angles ($> 60^\circ$). The same behavior, with a lower magnitude, was observed comparing DD045 (strike direction towards the excavation) and DD225 (strike direction against the excavation).

It is important to keep in mind that this comparison shall not be made straight forward, considering that the reference monitored points to be compared are the ones on opposite walls, e.g. for DD045 the monitoring point 17 should be compared with the monitoring point 16 for DD225 (Fig. 59). Fig. 59 plots the radial and tangential displacements using the X-Z plane for DD045 and DD025, the figure graphically represents the described behavior.

The spatial displacement behavior, represented by alpha, seen on the right side-wall for DD090 and for DD045, as also detected for DD225 on the left side-wall. The angle on the left side-wall for DD225 (the behavior applies for all monitored points with different magnitude) rotates towards the excavation up to a maximum rotation angle at a dip angle close to 45°; as the dip angle becomes steeper (>45°) the vector rotates back against the direction of the excavation. The opposite behavior was observed for DD045, in this case the vector on the right side-wall rotates against the excavation and rotates back after the maximum rotation is reached at the same dip angle (45°).

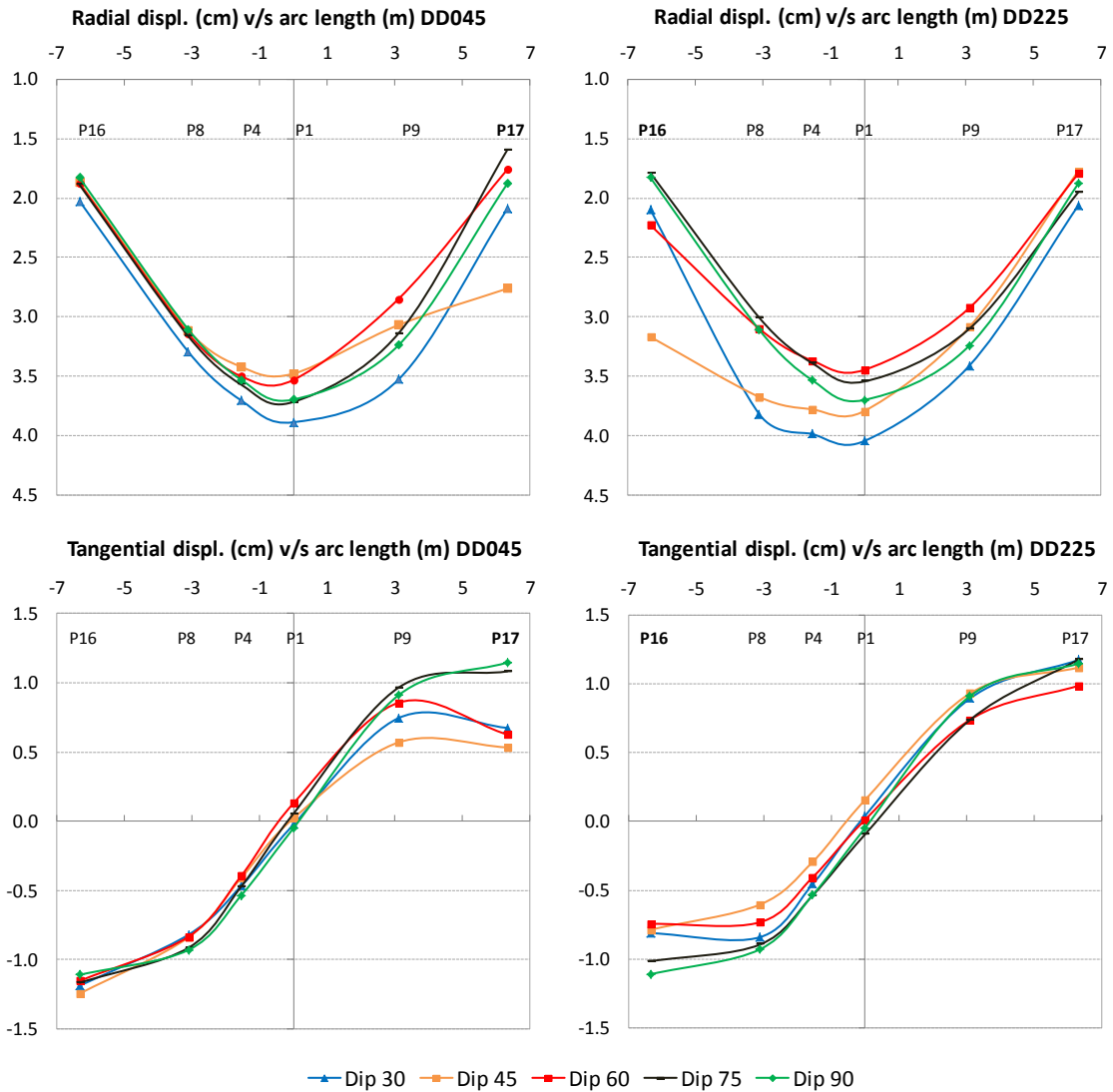


Fig. 59: Radial and tangential displacements for DD045 and DD225

Fig. 60 depicts the variation of alpha for a weakness plane striking in the above mentioned dip directions. The figure shows high weakness plane influence on the left side-wall for DD225, it is also worth highlighting that, although alpha is rotating in opposite directions, there is similar behavior as for DD045 and DD225 with increasing weakness plane influence onto the side-wall where the weakness plane quasi-tangentially intersects the excavation.

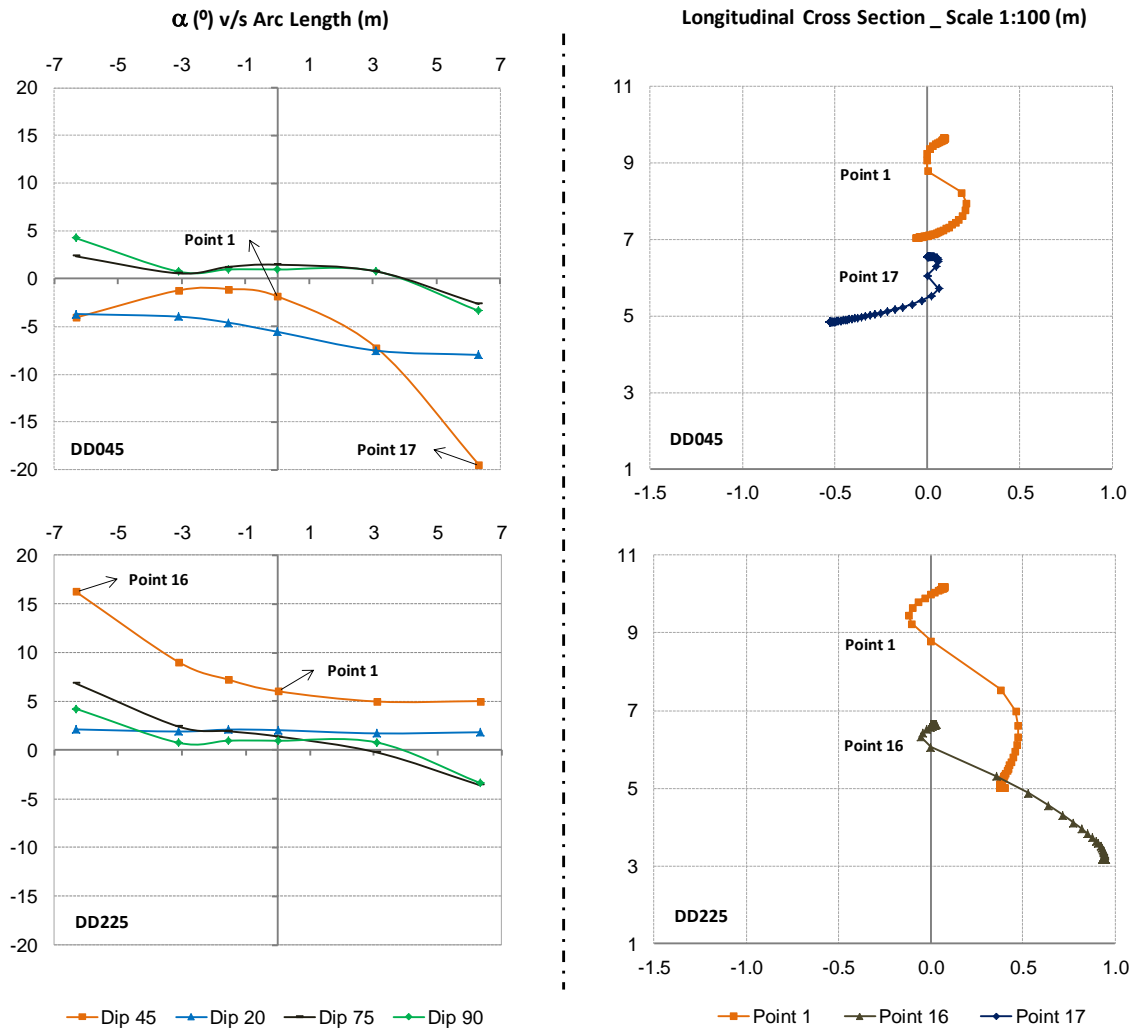


Fig. 60: Alpha results for DD045 and DD225

Comparing the displacement behavior along the excavation intrados for DD045 and DD135 it is possible to clearly detect the weakness plane influence on the right side-wall for the evaluated stress conditions as presented in Fig. 61. The figure shows the comparison between the mentioned dip directions for a weakness plane dipping 45°. It is also worth highlighting from the figure that, in general terms, pre-displacements are lower for DD135 than DD045.

Further stress conditions were also evaluated (18.75MPa and 25MPa); however, some of the results had to be discarded due to the shortcoming of the ubiquitous joint model (see section 2.3.2). Comparing the results of DD045 and DD135 (σ_1 equal to 6.25MPa and 12.5MPa), it was observed that final displacements increase between 6% and 18%, from DD045 to DD135. Stress condition $\sigma_1=25\text{MPa}$ was also evaluated, the results yielding an increase between 90% and 150%, highlighting the numerical model limitation. Section 5.4 takes this case as an example of the model limitations.

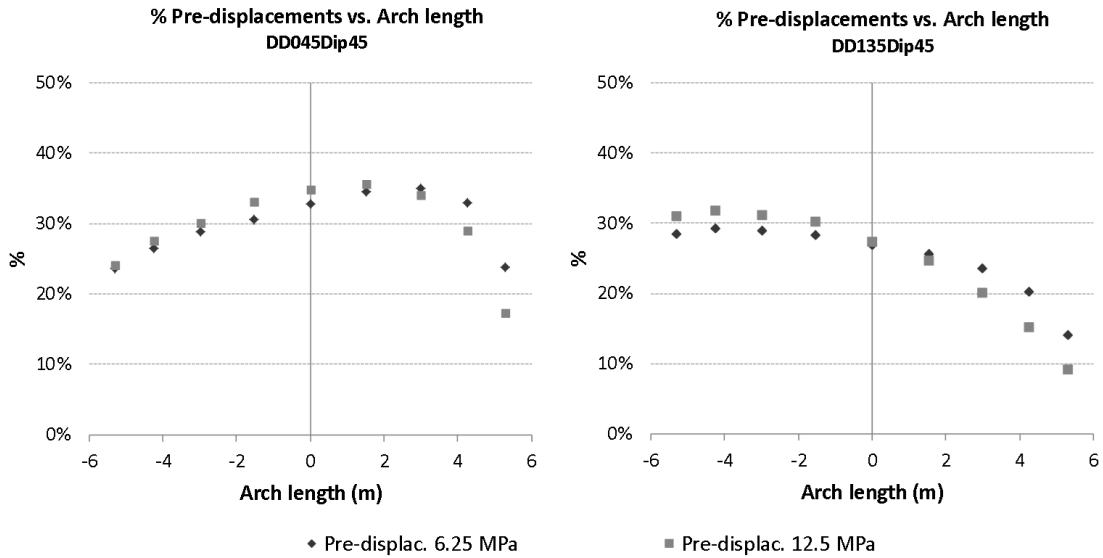


Fig. 61: Variation of displacements ahead of the face for DD045/Dip45 and DD135/Dip45

The displacements development for the weakness planes DD045 and DD225 is shown in Fig. 62. The figure includes the displacements development of the crown point (monitoring point P1) and 2 additional monitoring points on the side-wall where, as previously described, the weakness plane influence is larger (P8 and P16 for DD225 and P9 and P17 for DD045).

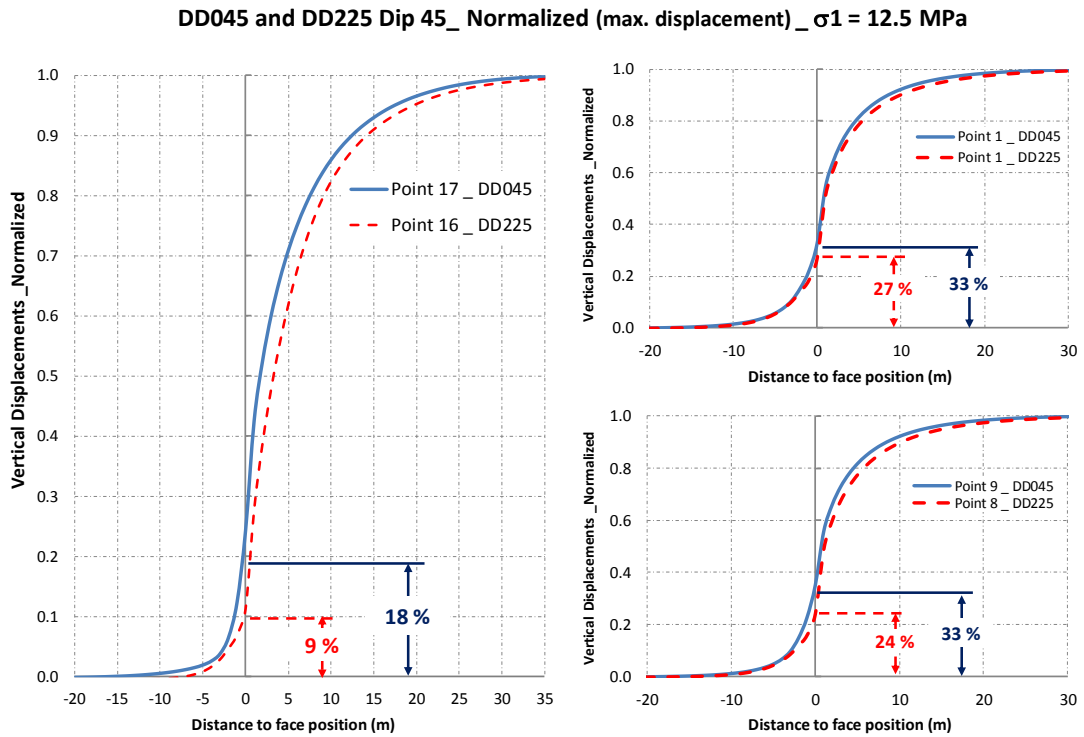


Fig. 62: Displacements development for DD045 and DD225

The figure allows the comparison of a weakness plane striking with an acute angle, between the dip direction and the tunnel axis, towards (DD045) and against

(DD225) the direction of the excavation. The behavior remains similar to the one observed in Fig. 49 (comparison between DD000 and DD180), in which better conditions for tunneling are expected if the excavation takes place in the same direction as the weakness plane's strike, considering that higher displacements ahead of the face entails lower support requirements.

Comparing Fig. 62 (DD045 and DD225) and Fig. 49 (DD000 and DD180) it is also seen that the magnitude of the pre-displacements for DD045 and DD225 exhibits smaller percentage of pre-displacements independent of the monitoring points.

4.2. Material Properties Influence on the Displacement Behavior

The Ubiquitous joint model used in the present work requires multiple input parameters for an accurate ground behavior simulation, with the presence of an orientation of weakness (weak plane in a Mohr Coulomb medium), as seen in chapter 3.

A total of fifteen parameters are needed for the implementation of the model. Considering this high number of variables it is important to establish possible correlation between each input parameter and its influence on the displacements behavior.

This section focuses on the assessment of the displacement vector behavior, due to changes in the material properties (matrix and weakness plane properties); the variation of the vector is summarized in the magnitude and alpha (3D behavior) and beta (2D behavior) angles for the different points along the intrados.

It is worth mentioning that, although there is an inherent inversely proportional relation between material properties and magnitude of displacements (i.e. weaker materials yield higher displacements). The aim of this work is to detect variations and trends on magnitude and angle rotation, as well as detect how and which properties influence the behavior the most.

4.2.1. Scatter plots

Scatter plots is a useful tool to display correlations, if any, between two variables for a set of data. Since there are multiple variables influencing the displacements behavior, the input parameters shown in Table 2 are set as reference values and remain fixed while the assessed property (input parameter) varies within a certain range.

The approach to evaluate the variation on the displacement behavior is assembling the scatter plots for a given set of parameters and stress condition, while varying one material property at the time. The described procedure allows the determination of trends for a given set of parameters and stress (magnitude and orientation). It should be kept in mind that considering the displacement behavior is highly dependent on the stress level and stress distribution, the

observed trends are later verified through simulations for different stress conditions.

The simulated stress condition resembles an overburden of 250 m in which the matrix properties (reference values, Table 9) are still in an elastic range. The analysis of the scatter plots was divided into three different sets, the first one gathers the influence of each property of the matrix is assessed, the second one with the influence of weakness properties and a third group in which the input values regarding weakness plane orientation (also 4.1) are assessed.

Note that the selected weakness plane is defined by dip direction of 045 and dip angle of 45° , trends are determined for the mentioned DD and dip angle and further verified for different weakness plane orientation by means of additional numerical simulations.

Although matrix properties are evaluated, the scope of the present work is to assess the displacement behavior due to the presence of a weakness plane in the rock mass. Therefore, the set of material properties shown in Table 9 aimed to have low influence due to the matrix variation and high influence of the weakness plane properties, in the range in which the used constitutive model, delivers reliable results.

It is worth mentioning that approximately 50 simulations had to be discarded, during the assessment of the material properties on the displacements behavior, due to the shortcoming of the ubiquitous joint model presented in section 2.3.2. The results of the discarded simulations clearly showed an overestimation of displacements due to the weakness plane properties reduction, in combination with the stress conditions. The presented results only include those simulations in which no displacement overestimation was observed.

4.2.1.1. Matrix properties

Tendencies and trends might vary depending on the monitored point, for this reason, the scatter plots are assembled for three monitoring points on the side-wall in which the weakness plane has a greater influence (Fig. 63). For the evaluated dip direction and dip ($045/45^\circ$) the scatter plots are assembled for: two monitoring point on the right side-wall (Point 9 and point 17), which display the highest influence from the weakness plane (4.1.4) and the crown monitoring point (Point 1) which showed the highest displacement values from the overall monitored points.

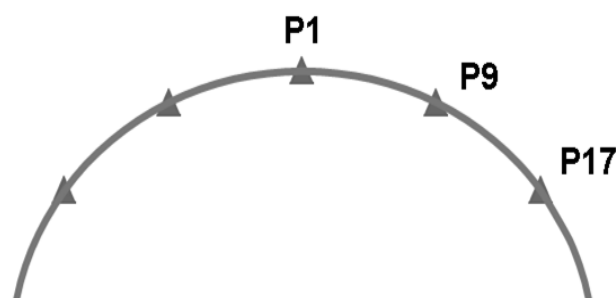


Fig. 63: Scatter plots monitored points

The modulus of elasticity, as expected, is the only matrix property that yields a considerable influence on the displacement magnitude. Its variation is framed by exponentially displacement decrease as the elasticity modulus increases. The scatter plots shown in Fig. 64 also display the low influence on the magnitude due to changes in the strength matrix properties (cohesion, friction angle and tensile strength); an expected result, considering the set of stress conditions and the matrix reference properties.

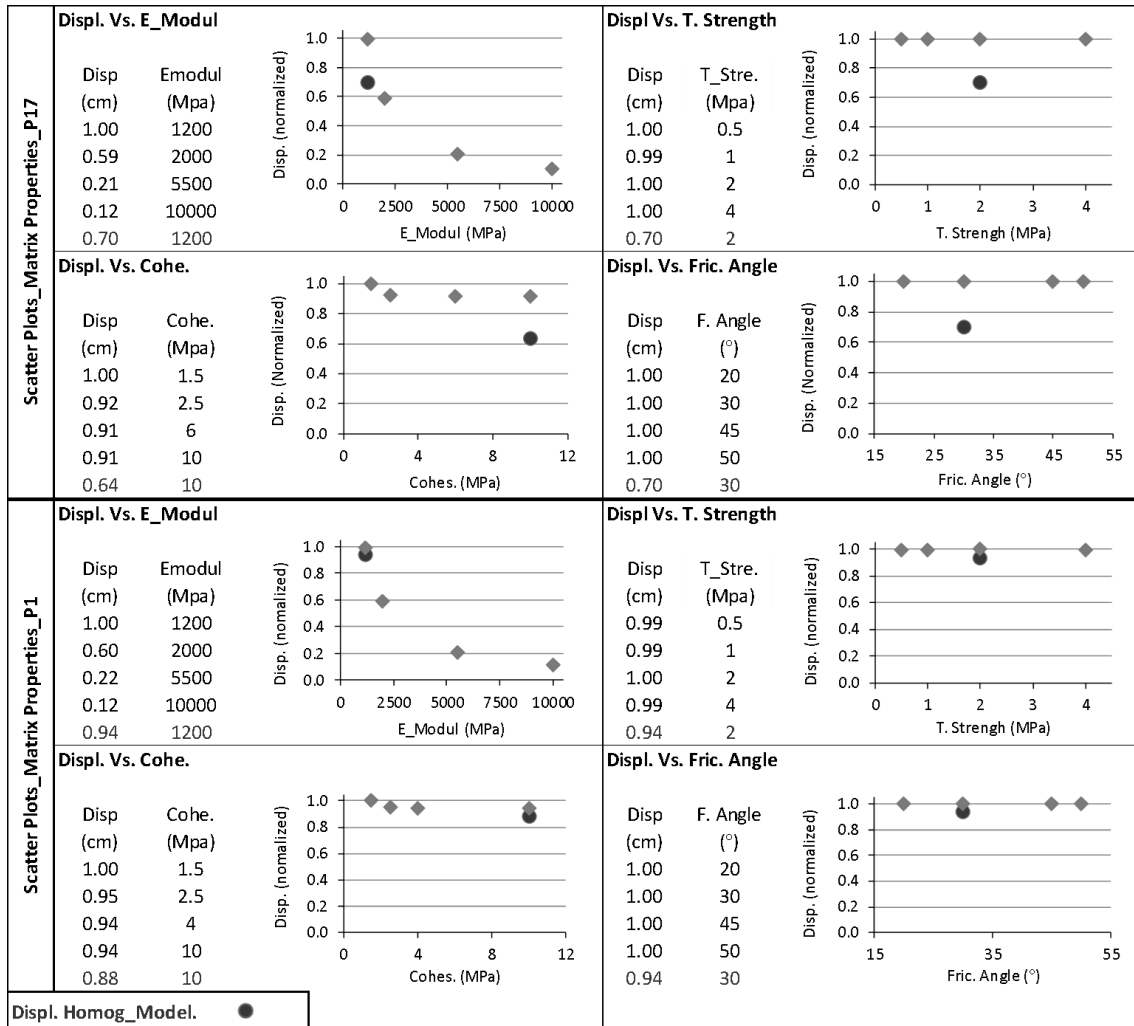


Fig. 64: Scatter plots displacements magnitude (normalized) for monitoring points P1 and P17 vs. Matrix properties variation

Fig. 65 confirms the trends observed in the previous scatter plots. First, the right side of the figure shows a rather wide plastification on the weakness plane and second, the left part of the figure clearly displays very low matrix plastification “shear-n”.

Note in Fig. 65 that the elements colored in yellow are exclusively related to the matrix, elements displayed in light gray result as the combination of matrix and weakness plane plastification. The figure is assembled for DD045 and dip angle equal to 45°, the properties shown in Table 9 and, for this specific case, the matrix friction angle is set to 20°.

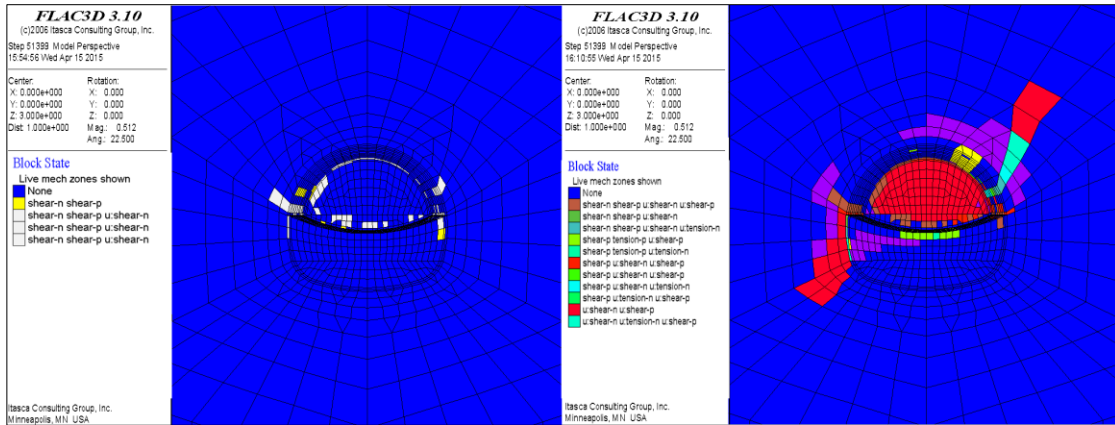


Fig. 65: State plot for matrix (left) and weakness plane (right). Matrix friction angle equal to 20°

The trend showed in Fig. 64 results of the normalization of displacements with the maximum displacement magnitude. For the two remaining characteristic angles (alpha and beta), the trends are plotted as a difference “delta” (Δ) with respect to the value yield by the homogeneous model. This standardization of the characteristic angles is further used during the results implementation in a computation tool (chapter 6).

The behavior from beta and alpha is depicted in Fig. 66 and Fig. 67 respectively. Note that the figures display an increasing weakness plane influence towards the right side-wall. This behavior was already observed for a fixed set of material properties (section 4.1.3); the scatter plots for the mentioned set of parameters, in addition to the results seen in 4.1.3, show no dependency between this behavior, neither with the strength properties nor with the elastic properties.

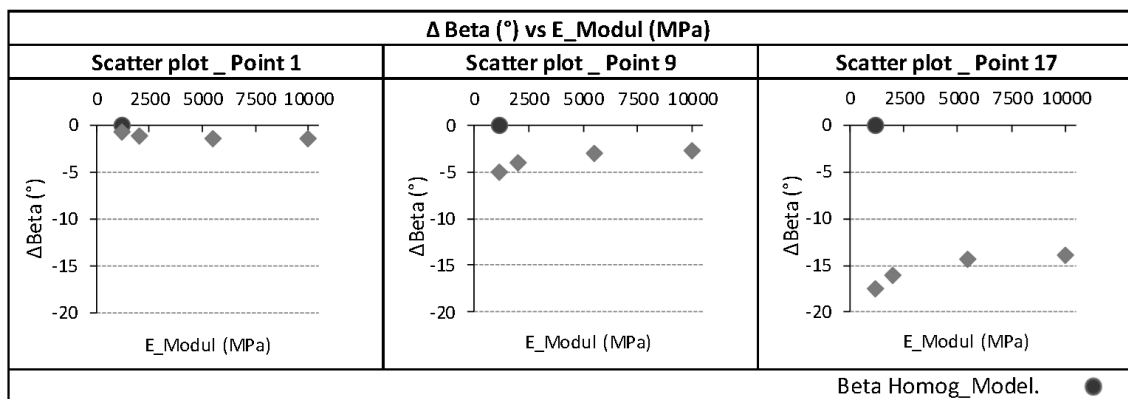


Fig. 66: Scatter plots, Δ beta vs. Elastic modulus

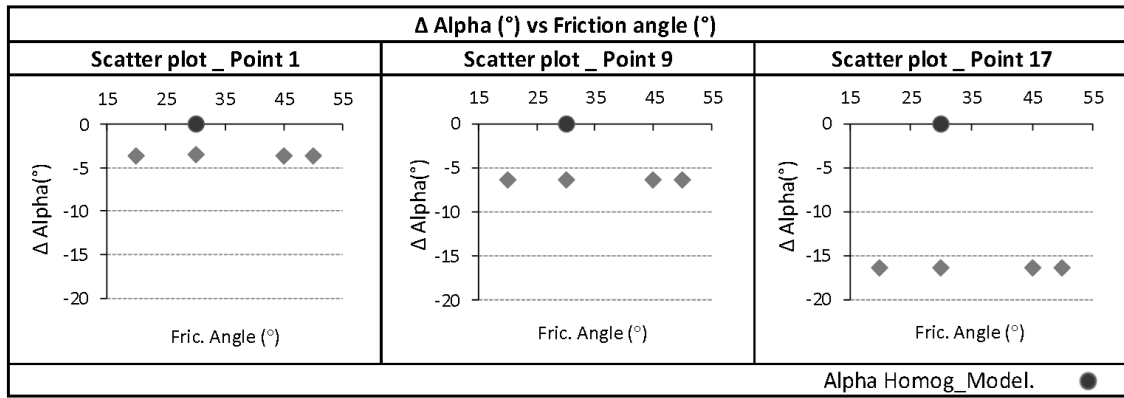


Fig. 67: Scatter plots, Δ alpha vs. Matrix friction angle

The scatter plots of the matrix properties variation, display a rather low influence on the overall behavior. However, it is important to keep in mind that the behavior is yielded for the chosen set of parameters in connection with the restrictions of the implemented constitutive model.

4.2.1.2. Weakness plane properties

The scatter plots in this section were assembled considering variations on the weakness plane cohesion, friction angle, dilatancy and tensile strength. The same monitoring points shown in Fig. 63 were assessed.

The ubiquitous joint model from Flac3D, analyses failure in the weakness plane once the general failure is calculated and plastic corrections are applied [79]. The new recalculated stresses are then used to analyze failure on the weakness plane. Further corrections and updates of the overall condition are assessed considering the weakness plane spatial orientation.

Displacement magnitude shows a strong dependency with the weakness plane cohesion and friction angle, as shown in Fig. 68 and Fig. 69. The scatter plots for display a well-defined exponentially displacement decrement as the weakness plane cohesion increases, this trend amplifies towards the left side-wall (P9-P17).

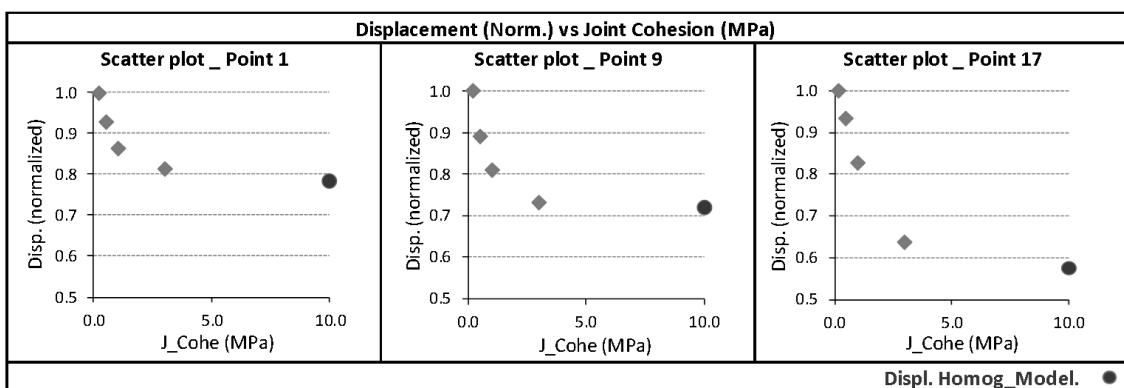


Fig. 68: Scatter plots, Displacement magnitude vs. Weakness plane cohesion

The variation of the joint friction angle yielded, in contrast to the trend observed in Fig. 68, no visible amplification of the trend when comparing monitoring points P1 and P9. Monitoring point P17 displays a rather different trend; it flattens for the lowest evaluated J_{fric} values, implying small influence of this property in the displacements magnitude. This behavior changes as the J_{fric} value comes closer to the value of the matrix friction angle, in this case a high decrease of displacement magnitude is seen with small changes in the J_{fric} . (Fig. 69). Higher J_{fric} should not display a significant variation on displacement magnitude, limited by the value yielded by the homogenous model.

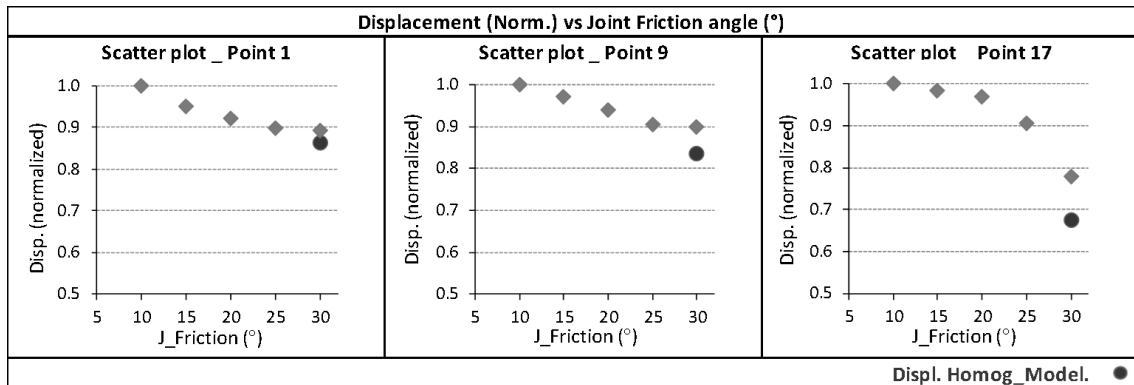


Fig. 69: Scatter plots, Displacement magnitude vs. Weakness plane friction angle

The displacement behavior for a weakness plane with dip direction 045 and a dip angle of 45° (section 4.1.4.), was framed by a beta (β) and alpha (α) angle lower values in comparison to the homogeneous model (monitoring points P1, P9 and P17). Particularly the displacement vector, it is visible that it rotates towards the left side-wall (see beta) and at the same time, it rotates against the excavation direction (see alpha).

Note that the representation of the angles in the scatter plots is done considering the angles yielded by the homogeneous model as a reference value (i.e. a negative value on the scatter plot portraits a lower angle when compared with the homogeneous model, not necessarily a negative value on the local coordinate system (Fig. 19)).

Fig. 70 and Fig. 71 depict the beta and alpha angle behavior, respectively, with the variation on the weakness plane strength properties. The scatter plots for both cases, showed an increment of the weakness plane influence for monitoring points closer to the right side-wall.

The J_{coh} 's scatter plots (Fig. 70) showed a rapid decrease of the influence of this parameter, reaching values yielded by the homogeneous model with a rather low value of the weakness plane cohesion, approximately 25% of the matrix cohesion (see also Fig. 68). It can be seen that the magnitude and angle values, displayed by the homogenous model, are not reached when the J_{fric} is set to a value equal to the matrix' friction angle. The beta value, shown in Fig. 70, indicates a rotation towards the left side-wall, due to the weakness plane orientation. It is important to bear in mind that the mentioned rotation is the value obtained by comparing each result with the angle yielded by the homogeneous model.

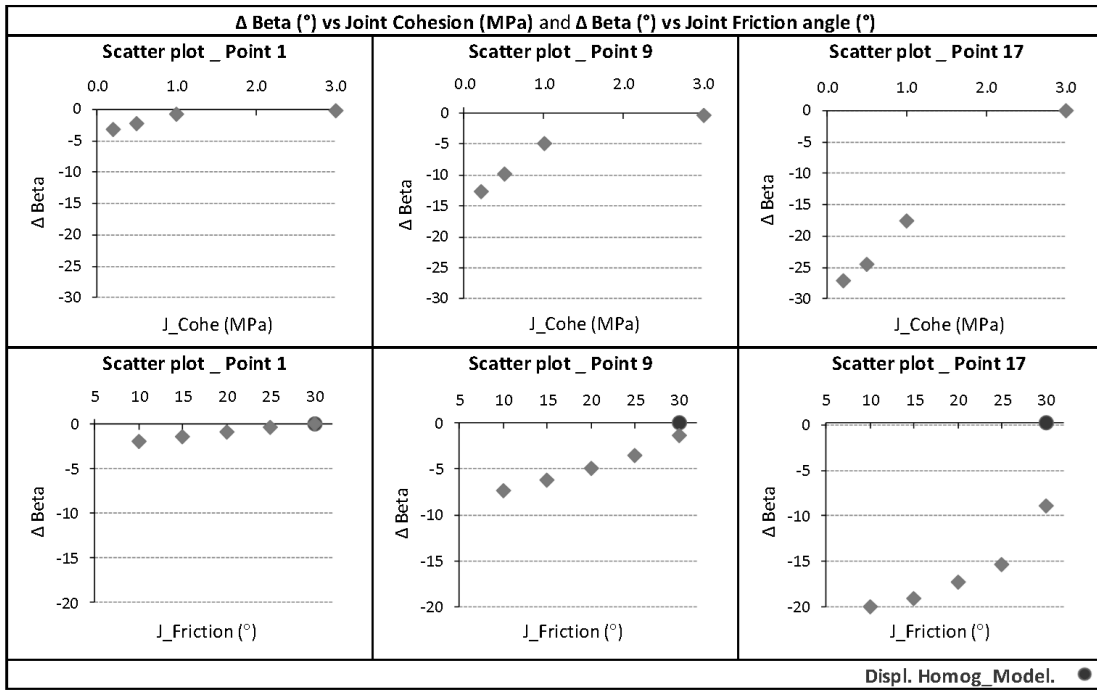


Fig. 70: Scatter plots, Δbeta vs. Weakness plane cohesion and friction angle

Shown in Fig. 71 is the variation of the 3D displacement angle, alpha. In this case, the reference homogeneous model displays a positive value, rotating towards the direction of the excavation (Fig. 48). The rotation of alpha for DD045 and dip angle of 45° , in contrast to the homogeneous model behavior, yields negative values indicating a vector rotation against the direction of the excavation (section 4.1.4).

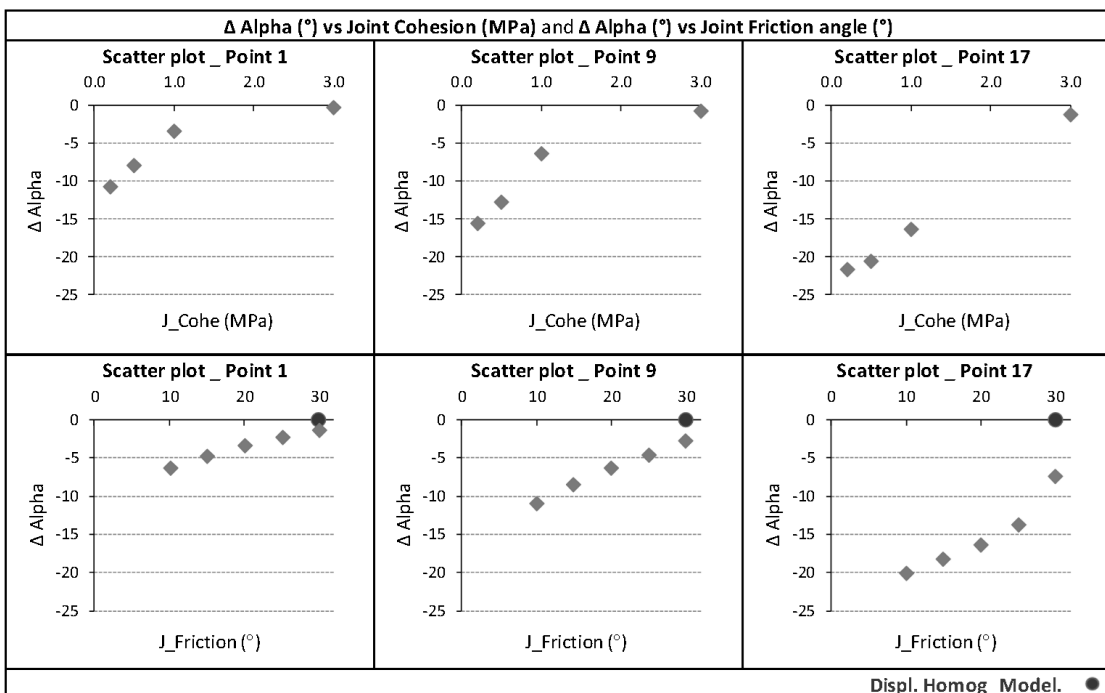


Fig. 71: Scatter plots, Δalpha vs. Weakness plane cohesion and friction angle

Similar to the results observed for beta, alpha rotation rapidly decreases with the increment on the J_{coh} . The angle reaches the values yielded by the homogeneous model, as the J_{coh} is set to approximately 30% of the matrix cohesion. The friction angle displays a similar behavior to the one observed for a beta, not reaching the value displayed by the homogeneous model, even when equal values are set for matrix and weakness plane friction angle.

Scatter plots were also assembled varying the joint dilatancy angle; however, no significant changes were observed on the evaluated monitoring point.

The results shown in this section are not taken as absolute or fix values, but rather as a trend as a variation (increase, decrease, positive or negative rotation, etc.) due to variations on the material properties. The variations addressed in this section are s further implemented into chapter 6.

5. DISCUSSION

The current study makes use of the ubiquitous joint model in order to simulate the ground behavior of rock masses entailing a plane of weakness. After a literature review and the description of the implemented numerical model, the study evaluated the capability of the numerical model to simulate the system behavior monitored during the construction. For this purpose the Galgenberg was used (section 3.4) and it was shown that the numerical model is able to simulate the displacements behavior recorded during construction (Fig. 34 and Fig. 36) under the requirements in terms of material properties, boundary conditions and a single weakness plane influencing the ground behavior (section 2.3.2).

More than 400 simulations were performed to establish the influence of orientation and material properties on the ground behavior. This chapter discusses the main findings regarding behavior of rock masses with the presence of weakness plane. On the one hand, summarizes and evaluates the causes leading to the observed trends and, on the other hand, the chapter highlights the applicability of the finding on: 1st the assessment of the ground and system behavior during design and 2nd the correct interpretation of displacement monitoring data, aiming towards a proper model validation and its updating during construction.

The discussion makes use of the eastern area of the stereogram ($000 \leq DD \leq 180$), taking into consideration the shown symmetrical behavior. All trends are evaluated in terms of magnitude, express by radial and tangential displacements, angle orientation, summarized by beta (2D) and alpha (3D) rotation and displacement development to assess the weakness plane influence on the percentage of displacements ahead of the face (pre-displacements).

5.1. Observed Trends

The below described trends are framed by the weakness plane influence in the ground behavior. As shown in chapter 2 and, complemented by the validation of the numerical model presented in section 3.4, there is a need to include all relevant geological (e.g. weakness planes) features in order to accurately understand and predict the behavior.

The perfect symmetrical prediction resulting from homogeneous models and models that directly smear the discontinuities into a continuum (section 2.3.1.2) do not accurately predict the ground behavior, this is highlighted by multiple researchers [1] [3-8] [12] and also seen during this study where the prediction of a numerical model incorporating a weakness plane into a Mohr Coulomb medium (e.g. ubiquitous joint model), is more in agreement with the monitored displacements data than the prediction made by the Mohr Coulomb model (Fig. 32 to Fig. 35).

5.1.1. Weakness plane orientated perpendicular to the tunnel axis

This section refers to weakness planes' orientation aligned with the tunnel axis. Two dip directions are discussed: DD000, plane orientated towards the direction of tunneling, and DD180, plane orientated against the direction of tunneling.

The magnitude of displacement is for both dip direction (DD000 and DD180) display a similar behavior. It is inversely proportional to the dip angle, reaching a maximum value at a dip angle of 20° and decreases for steeper angles to minimum displacements observed at a dip angle of 90° .

It is important to highlight that the observations regarding displacements magnitude, does not take into consideration a weakness plane with dip angle equal to 0° , which constitutes a common plane for all dip directions. It was observed, during this study, that this plane (dip angle equal to 0°) yields the highest displacements on the tunnel crown, due to shear stresses along the weakness planes and a subsequent bending behavior perpendicular to the this surface, same behavior described by Francis [37] and Vardar [39] in their studies.

All monitored points, up to a dip angle of approximately 45° , display larger displacements for DD180 than DD000. Steeper dip angles display the opposite behavior yielding larger displacements for DD000 than DD180 (Fig. 47). This complies with the observation from Francis [37] and Bieniawski [38], who set this dip angle (45°) to separate a "very unfavorable" from "favorable" conditions for discontinuities orientated perpendicular to the tunnel axis.

For the same in-situ stress conditions, no visible beta rotation was observed during this study for the mentioned dip direction. This is an expected result taking into consideration that the weakness plane surface, not its orientation, is aligned with a Z-X plane. Beta rotation orientated for weakness planes perpendicular to the tunnel axis, is mainly controlled by the minor principal stress (σ_3).

It has been seen throughout the study that major changes due to bending and shear take place perpendicular to the mentioned weakness plane surface, implying that displacement vector rotation, as well as displacements ahead of the excavation, will take place at a Z-Y plane (longitudinal section).

The displacement vector orientation is towards the excavation orientation for DD180 (positive angles), whereas DD000 displays a clear steady orientation again the direction of excavation (negative angles). The direction of the rotation is also related dilation causing shear (slide) and bending stresses perpendicular to the surface of the weakness plane. Two exceptions were observed for DD000 at a dip angle of 60° and 75° where monitoring points P1, P8 and P9 yielded positive values. A closer look at the displacement development, show that initially displacements, follow the same pattern as flatter dip angles ($<60^\circ$), however unlike flatter dip angles, as the excavation continues there is no visible reorientation of the vector but an alignment with the direction of the weakness plane surface, implying sliding along the surface only on monitoring points where a free surface is given by the excavation (e.g. P1, P8 and P9). This behavior becomes less prominent as the stress level increases (Fig. 41).

DD000 shows higher percentage of displacements ahead of the face in comparison to the ones yielded by DD180 (Fig. 49), this observation is in agreement with Klopčić [70] who, with a different numerical approach and using displacement monitoring data from a different project, came to the same conclusion.

5.1.2. Weakness plane parallel to the tunnel axis

This section discusses the behavior shown by dip direction DD090, the contents of this section also apply for dip direction DD270 on opposite side walls.

Displacement magnitude along the intrados is highly influenced by the weakness plane. From the studied dip angles, the crown point shows higher displacements for the flattest (0° and 20°) and for the steepest (75° and 90°) angles, mainly due to bending and sliding, respectively. The trend for the intermediate points displays a combination of sliding and bending. Bending, as a consequence of shearing along the weakness plane, sub-sequential increment on tensile stress, leading to bending stresses perpendicular to the weakness plane surface, was mainly observed for dip angles $<55^\circ$ (Fig. 51 and Fig. 52). It was also observed that as the dip angles increases ($>55^\circ$), sliding induced displacement predominates on the left side wall, where sliding is possible due to the free area given by the excavation (see upper part of Fig. 53). Both trends, for the crown and intermediate monitoring points, are in agreement with the observation of Goricki [40] and with Fig. 5, which summarizes the empirical observations made by Vardar [39].

Beta and alpha rotation display a similar behavior. Its rotation increases up to a maximum value, clockwise rotation for beta and rotation against the excavation for alpha, close to a weakness plane dipping approximately 50° . Beta and alpha rotation decreases to its initial values for steeper angles ($>50^\circ$). The behavior is well noted on the left side-wall, intermediate points show closely the same behavior in a much lower magnitude as seen in Fig. 52.

A distinct pre-displacement behavior involving the right side-wall was observed for DD090. The lowest percentages of pre-displacements are observed for the right side-wall (monitoring Point 17) for dip angles between 30° and 60° , independent of the stress magnitude (Fig. 54). DD090 also register higher pre-displacements on the left side-wall than on the right side-wall for dip angles steeper than 70° (Fig. 58).

5.1.3. Weakness planes in tunneling direction, acute angle between tunnel axis and weakness plane dip direction

The trends described and assessed in this section refer to dip directions $010 < DD < 080$ (the contents of this section also apply for $280 < DD < 350$ on the opposite sidewall). The trends mainly come from the simulations performed for DD015 and DD045 and complemented by multiple simulation performed between the mentioned dip directions. This section takes as a reference the results yielded by DD000 and DD090 in order to have a general overview.

The displacement magnitude is controlled by a combination of sliding and bending along the weakness plane surface. The crown point, for DD015 and DD045, displays maximum values for dip angles flatter than 20° and steeper than 75° . The behavior of intermediate and side-wall monitoring points, unlike the behavior displayed by DD090, do not display an outstanding displacement increment on the right side-wall due to shearing and subsequent bending (Fig. 57); the behavior is related to a reduced “common area” in which the weakness plane intersects the excavated area.

Fig. 72 depicts the referred “common area” as a line intersecting the weakness plane with the excavated area, it is important to keep in mind that a weakness plane is not defined by a single plane but rather a weakness direction given by a dip and a dip direction. Furthermore, a smaller “common area” in combination with the weakness plane orientation for DD015, limits the bending aptitude on the right-side wall. As a consequence, displacements for DD015 exhibit larger values on the right side-wall only for the lowest studied dip angle (10°), opposite to the behavior shown by DD045 where larger displacements on the right-hand side are displayed for all dip angles up to 45° due to bending, similar to the behavior shown by DD090.

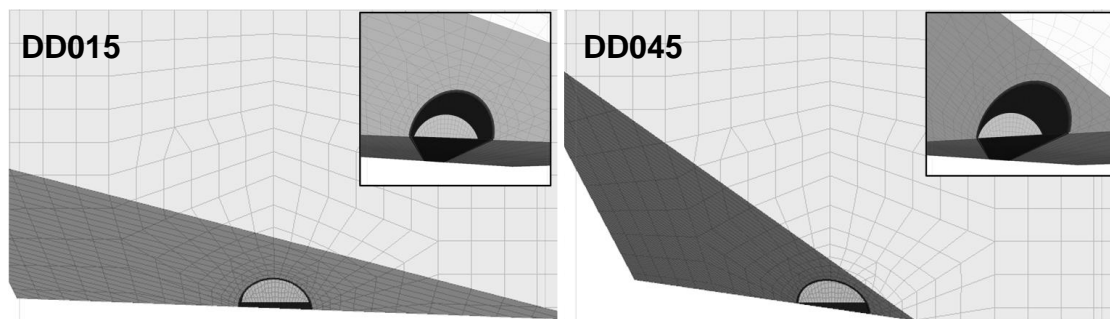


Fig. 72: Comparison weakness plane DD015 (left) and DD045 (right)

Beta rotation displays a similar behavior on the assessed dip directions (DD015 and DD045). First, monitoring point P1 remains almost unchanged for all dip angles and second, left wall monitoring points P8 - P16 and right wall monitoring points P9 - P17 display a counter clockwise and clockwise rotation, respectively, similar to the rotation shown by DD090 at a lower magnitude. Although the behavior is the same, its magnitude differs when comparing DD015 and DD045. For this evaluation it is important to keep in mind the influence of the weakness plane, on the right side-wall (bending) and on the left side-wall (sliding). Lower dip directions (e.g. DD015) display stronger influence on the left sidewall, resulting in similar opposite rotations on either side of the excavation. DD045 displays a much larger effect on the right side-wall, in other words the bending effect, as previously addressed, is larger for this dip direction.

Fig. 73 compares longitudinal displacements and alpha rotation for DD000, DD045 and DD090. Section 4.1.3 showed that maximum values for radial and tangential displacements were recorded for DD090 and the maximum rotation of the angle alpha was observed at a dip direction of 045.

The upper part of Fig. 73 displays the longitudinal displacements of a crown point (P1) and the right hand side-wall (P17), for weakness planes dipping 45° (orange) and 75° (brown). From the upper part of the figure it is worth highlighting, on the one hand, a rather low weakness plane influence on alpha rotation for the crown point, in agreement with Grossauer [76]. Additionally, an acute reorientation of this angle on the right side-wall for DD045 in comparison to the one yielded by DD090 at the same dip angle (45°). The orientation of the vector results as a combination of shear aptitude approximately perpendicular to the weakness plane orientation (Fig. 72) and tensile stresses, causing bending.

The above mentioned behavior is not seen for DD015, in this case, alpha rotates in the same order of magnitude as seen for DD000, rotating against the excavation for low dip angles (bending) and rotation towards the excavation for dip angles higher than 60° (sliding following orientation of the weakness plane).

DD045 displays another particularity of alpha rotation, not seen for DD015 or DD090. Dip angles $>60^\circ$ display a rotation on the left side-wall towards the direction of tunneling, opposite to the rotation display by right side-wall (Fig. 60). The lower part of Fig. 73 shows the variations of alpha along the arch length of the excavation, showing the above mentioned behavior, as well as clearly displaying the incremental weakness plane on the right side-wall.

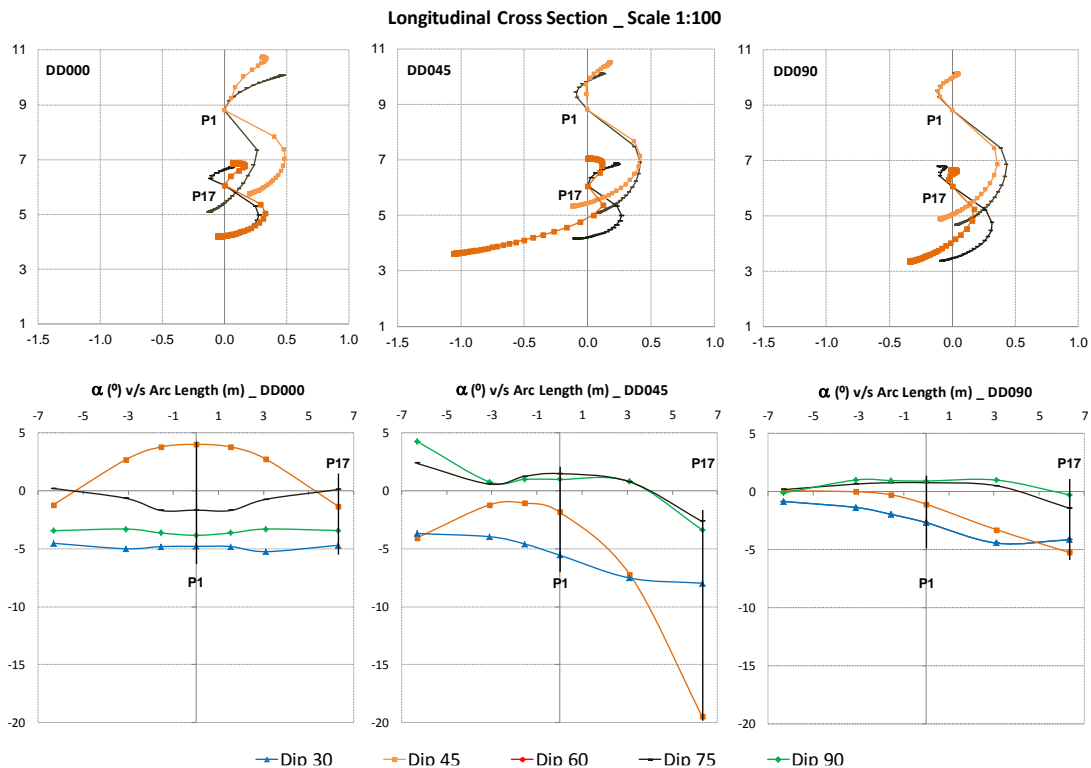


Fig. 73: Alpha results for DD000, DD045 and DD090

Displacements ahead of the face are, for all monitoring points and dip angles, lower for DD045 than for DD015. Dip direction 015 displays roughly the same pre-displacements percentage as the one registered for DD000, minor deviation were only registered for a dip angle equal to 60° . DD045 displays lower pre-displacements on the right side-wall than those registered on the crown and left

side-wall. The behavior remains constant, for all assessed stress conditions, up to a dip angle or approximately 45° when the trend changes displaying higher lower pre-displacements on the left side-wall (Fig. 58), the change of behavior was mentioned in section 5.1.2 (DD090) at a dip angle close to 70° . Fig. 74 displays this trend by comparing three different dip directions, highlighting the area in which the minimum percentage of pre-displacement are recorded. The highlighted area moves towards the right, indicating an increment on displacements on the right side-wall as the angle between the tunnel axis and the weakness increases up to a maximum value registered for DD090 and a dip angle of 45° .

Alpha rotates in the same order of magnitude as seen for DD000, framed by rotation against the excavation for low dip angles (bending) and rotation towards the excavation for dip angles higher than 60° (sliding following orientation of the weakness plane).

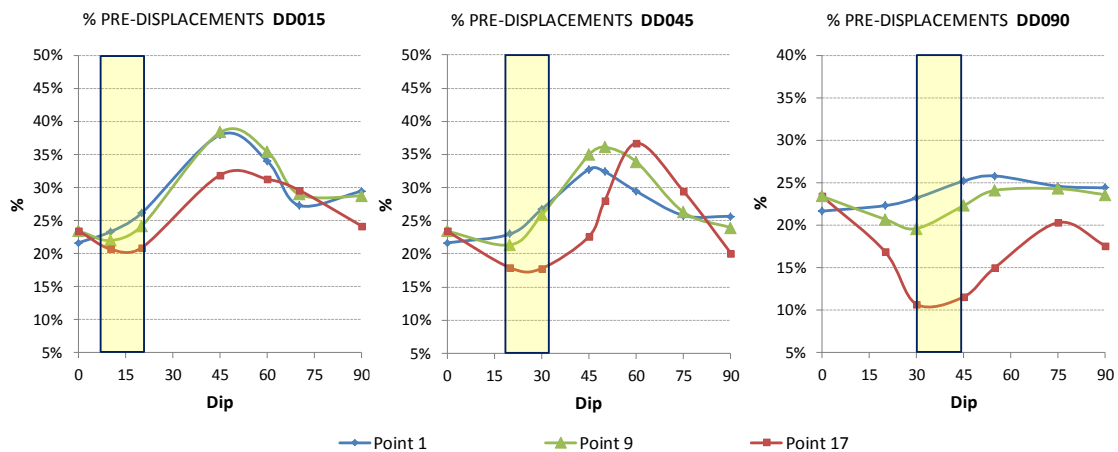


Fig. 74: Percentage of displacements ahead of the face for DD015, DD045 and DD090 ($\sigma_1 = 6.25\text{MPa}$)

The described pre-displacement trends imply: 1st. That the percentage of pre-displacements decreases as the dip direction angle increases, 2nd that the weakness plane influence increases on the right side-wall as the dip direction angle increases (e.i. lower pre-displacements are register for DD090 than for DD015) and 3rd that low dip direction angles exhibit the lowest pre-displacement percentage at a lower dip angle (e.i. dip angle 0° , 15° , 30° and 45° , exhibits the lowest percentage of pre-displacements for DD000, DD015, DD045 and DD090, respectively) (Fig. 74).

5.1.4. Weakness planes against tunneling direction, acute angle between tunnel axis and weakness plane dip direction

The trends described and assessed in this section refer to dip directions $100 < DD < 170$ (the contents of this section also apply for $190 < DD < 260$ on the opposite sidewall). Trends come from simulation performed for DD225, which will be consider for this section as DD135, and DD160, additional simulations between the mentioned dip directions were performed for verification.

A general observation is that displacement magnitude decreases as the dip direction increases from DD090 toward DD180. DD135 displays larger displacements on the right side-wall than on the left side wall for all dip angles lower than 75° , steeper dip angles show the opposite behavior with larger displacements on the left side-wall, the same behavior is seen for DD160 at a lower magnitude. In this case the dip angle of approximately 75° divides a shearing + bending aptitude on the right side-wall ($<75^\circ$) from, shearing + sliding on the left side-wall ($>75^\circ$).

For in the mentioned range ($100 < DD < 170$), α rotates toward the direction of tunneling for all dip angles below 75° . DD135, and at a lower magnitude DD160, displays an acute α rotation on the right side-wall (Fig. 60). The orientation of the vector results from a shear aptitude approximately perpendicular to the weakness plane orientation, this effect becomes less significant as the dip direction rotates towards DD180, where the shear aptitude is equal on both side-walls.

Note that the behavior described on the previous paragraph has a greater scale for DD225 and DD045, than those register for the previously assessed dip directions, striking towards (DD000) and against (DD180) the direction of excavation. A closer look at the Fig. 48, in which the α variation for different dip angles is displayed for DD000 and DD180, shows a maximum rotation of the angle of approximately 8° (from -5° for DD000 to 3° for DD180). Fig. 60, on the other hand, displays a maximum rotation of approximately 36° (from -20° for DD045, for monitoring point 17, to 16° for DD225, for monitoring point 16).

Previously evaluated was the dip angle which, in connection with the dip direction, yielded the minimum percentage of pre-displacement for the northern part of the stereonet ($270 < DD < 090$) (Fig. 74). The southern part ($90 < DD < 270$) is assessed in this section using weakness planes DD135 and DD160.

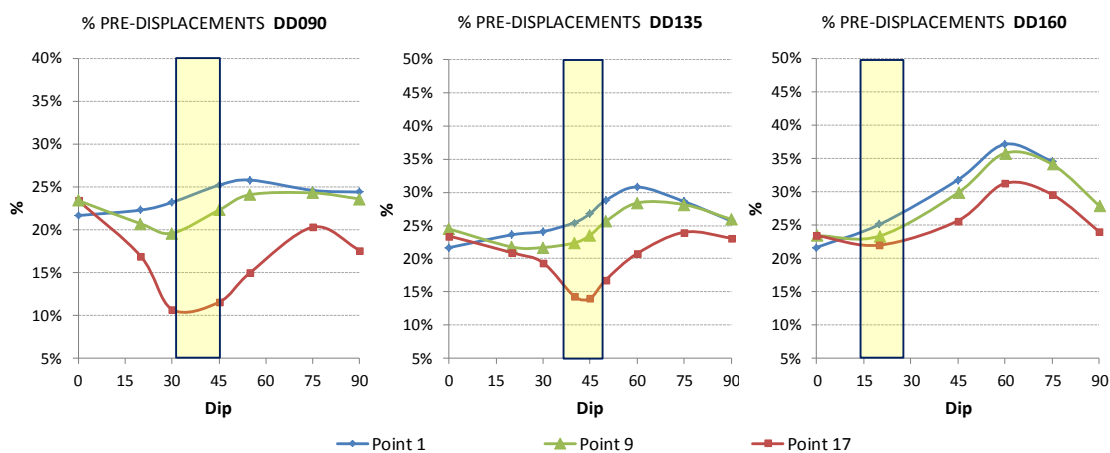


Fig. 75: Percentage of displacement ahead of the face for DD090, DD135 and DD160 ($\sigma_1 = 6.25\text{MPa}$)

The southern part of the stereonet, display a similar behavior to the one observed for DD090, where 45° is the dip angle with largest displacements, however, a notorious difference was detected as the dip direction moves toward DD180. Fig.

75 shows that the percentage of pre-displacements reached similar values between DD090 and DD135 and between DD160 and DD180.

5.1.5. Influence of material properties

It is important to take into consideration the failure criterion of the implemented constitutive model (Ubiquitous Joint Model). In general terms, the approach firstly inspects the general failure under standard Mohr Coulomb criterion and after applying relevant plastic corrections, the resultant stresses are used to analyze failure on the weakness planes define by strength properties and an orientation.

The scatter plots presented in section 4.2.1.1, showed no significant influence of the matrix strength properties on the overall behavior (Fig. 64). However, under this premise that the main scope of this work is to evaluate the influence of the weakness plane, the matrix properties where chosen not to play an important role on the overall behavior.

The displacement vector, described by a magnitude and a rotation of alpha, show a strong dependency with the weakness plane strength properties (Fig. 68 and Fig. 69). This is an expected outcome considering that the weakness plane defines its shear strength, opposite to the common definition of a discontinuity in which zero cohesion is assumed [27], as combination of the weakness planes' J_{coh} (c_j) and J_{fric} (φ_j) (and Eqn. 8). The mentioned definition is suitable considering that the scope of this work is to assess layered rock masses (e.g. phyllites) in which the joint cohesion plays a role.

Initially the weakness plane strength properties were addressed evaluating the influence in terms of a ratio, between the strength properties of the matrix and the weakness plane. However, framed by the shortcoming of the constitutive model, only general trends were reached.

Section 4.2.1.2 showed that weakness plane strength properties show a greater influence, on displacement magnitude, for the side wall for dip direction perpendicular to the tunnel axis, in agreement with the results described in section 4.1.3.

The weakness plane cohesion (J_{coh} .) displays an exponential decrement in terms of displacements as J_{coh} . increases. For dip directions not aligned with the tunnel axis, the described behaviors increases on the side-wall that the weakness plane intersects the excavation in a quasi-tangential manner (Fig. 75). The weakness plane friction angle (J_{fric} .) displays, a nearly linear influence, decreasing displacements linearly as J_{fric} . increases (Fig. 69 for DD045).

Fig. 76 displays the behavior resulting from the variation of the J_{coh} . for a weakness plane parallel to the tunnel axis (DD090), it is worth highlighting an incremental influence towards the right side-wall. Additional simulations showed that for monitoring point 17, and partially for monitoring point 9, the variation of J_{fric} . influences the behavior in the same manner as seen for J_{coh} . (exponential decrement).

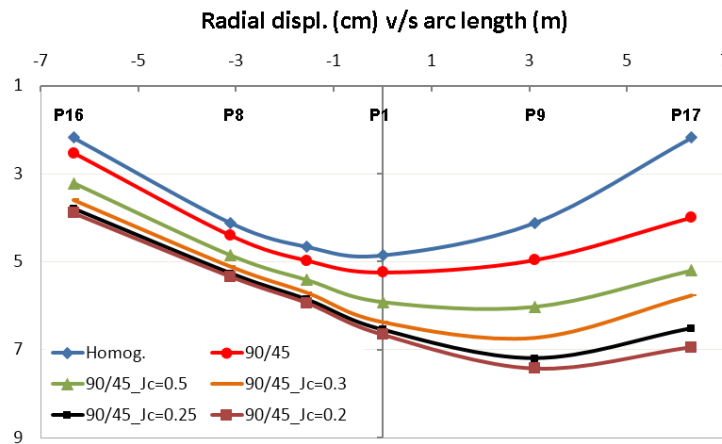


Fig. 76: Radial displacements variation for different J_coh values

Section 4.2.1.2, show the rotation of beta and alpha due to a variation on the weakness planes' strength properties, the rotation was framed by alpha and beta rotation to the values yielded by the homogeneous model if the J_coh. was set to approximately 25% of the matrix cohesion (Fig. 70), however, under the same conditions the values yielded by the homogeneous model are not reached, even when the J_fric. is set to the same value as the internal friction angle of the matrix. This behavior is caused by the combination of input parameter for this specific case, as shown in Fig. 77. The figure compares the stress plot for J_coh. equal to 3MPa, value in which the vector rotation is equal to the rotation of the homogenous model (left), and the results from J_fric. equal to 30°, which constitutes the upper limit value set by the matrix friction angle (right). The plot on the left shows a rather small sheared area when the J_coh. and J_fric. is set to 30% and 67%, respectively, of the matrix strength values. The figure on the right displays a larger sheared area when the J_coh. is set to 10% of the matrix cohesion value and Jfric. is set to its upper limit value. The described condition explains the results shown for point 17 (J_fric. scatter plots) in Fig. 69 to Fig. 71, were the rotations and displacement values, do not reach the ones yielded by the homogenous model.

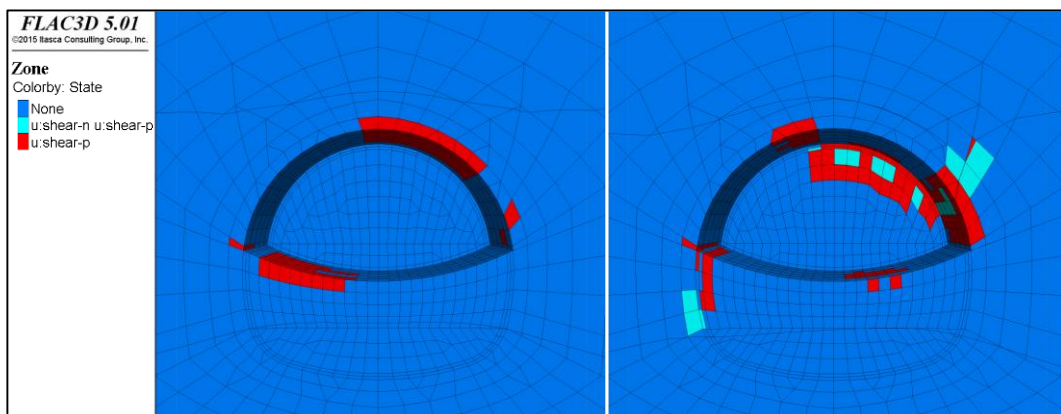


Fig. 77: State plot for J_coh=3MPa/J_fric=20° (left) and J_coh=1MPa/J_fric=30° (right)

It should be taken into account that following the definition of the ubiquitous joint model (chapter 3), the influence of the weakness plane strength properties directly

depends on additional factors such as: a) matrix behavior, of which general failure is initially evaluated, and b) stress conditions. This condition implies that the matrix properties variations have a direct impact on the weakness plane behavior. Note that this situation does not occur on the evaluated weakness plane orientation influence (section 4.1) in which, a fix set of parameters (stress condition, matrix and weakness plane properties), displays a quantifiable deviation with respect to a reference (homogeneous model).

The shortcoming of the implemented constitutive model (section 2.3.2) does not allow high contrast between the strength properties of the matrix and the weakness plane. The shortcoming restricts the behavior analysis for certain cross section parts where stress concentration, due to the influence of the weakness plane, lead to overestimation of displacements (section 5.4). Taking this into consideration, the applicability of the findings regarding a variation of the matrix and weakness plane properties is limited to: 1st a maximum ratio in which the weakness plane and the matrix do not display a high contrast: the contrast was compared by means of a ratio between the Plastic radii $P_{Rad.matrix}$ and $P_{Rad.WP}$ and 2nd a maximum value for the $P_{Rad.matrix}$. Note that limit ratio/values directly depend on the DD (see section 4.1 and chapter 6).

The plastic radius constitutes a useful tool considering that it involves the excavation size, stress conditions and it does not involve elastic properties which are not included in the weakness plane definition.

The conditions were verified and proved for all simulations in which overestimation of displacements was observed. The conditions are used in chapter 6 to limit the applicability of the prediction tool. Although partial results from the cross section are valid (see section 5.4) any result coming from a cross section not fulfilling the mentioned conditions was discarded.

5.2. General Trend Overview

Aiming to inspect the dip direction and dip angle in which maximum displacement magnitude, beta and alpha rotations are reached, this section makes use of results obtained in section 4.1.4. and evaluates two additional scenarios: 1st the result of varying the dip angle, for a fix dip direction (045), and 2nd the variation of dip direction with a fixed dip angle (45°).

The results presented in Fig. 78 show the displacement behavior for P1, P9 and P17 with the variation of the dip angle (the presented values are normalized by the maximum displacement). The figure shows the visualization of the dip angle in which the displacement magnitude reaches a maximum value and shows that the maximum displacements are linked to the monitoring point as follows: dip angles of 20°, 30° and 45° yielded the maximum value, for monitoring point P1, P9 and P17 respectively. The described trend is partially valid for all dip direction (the description of trends, displayed by different dip direction can be found in section 4.1). However, two general observations/trends can be summarized at this point:

1. Displacements on the right hand side are mainly cause by shearing along the weakness planes and sub sequential bending. Maximum displacements

depend on the weakness plane orientation in connection with the monitoring point where a quasi-tangential intersection takes place, between the plane and the excavation profile, and

- As seen in Fig. 78, the variation between the yielded values for different dip angles is greater towards the left side-wall, also in connection with weakness planes intersecting in a quasi-tangential manner the excavation profile (section 4.1.3, 4.1.4 and 4.1.5). This trend does not fit the behavior observed for weakness planes perpendicular to the tunnel axis (sections 4.1.1 and 4.1.2).

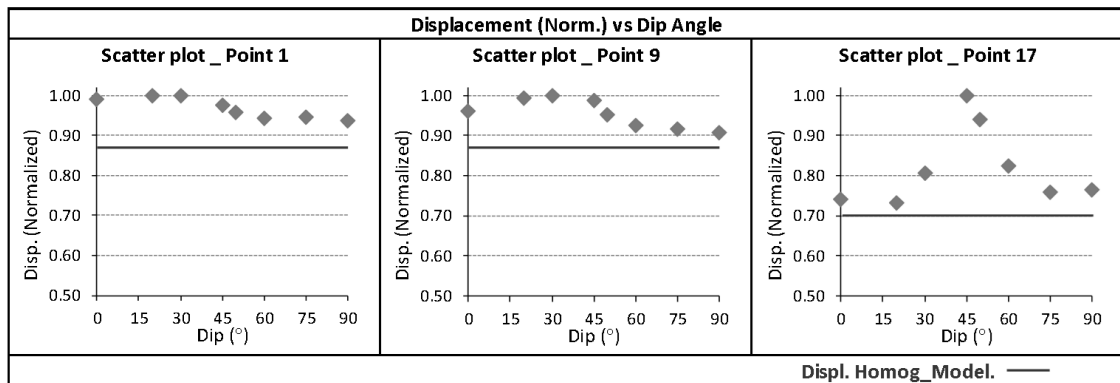


Fig. 78: Scatter plots, Displacements vs. Dip angles for DD045

The first described trend can be visualized in Fig. 79. The figure plots the maximum displacement values in connection with a dip angle and a dip direction. The figure also includes highlighted areas related to the dip angle which displays the maximum displacement, at a given monitoring point. The figure shows that the trend applies for all assessed dip directions not aligned to the tunnel axis, with some variation for DD015 and DD160.

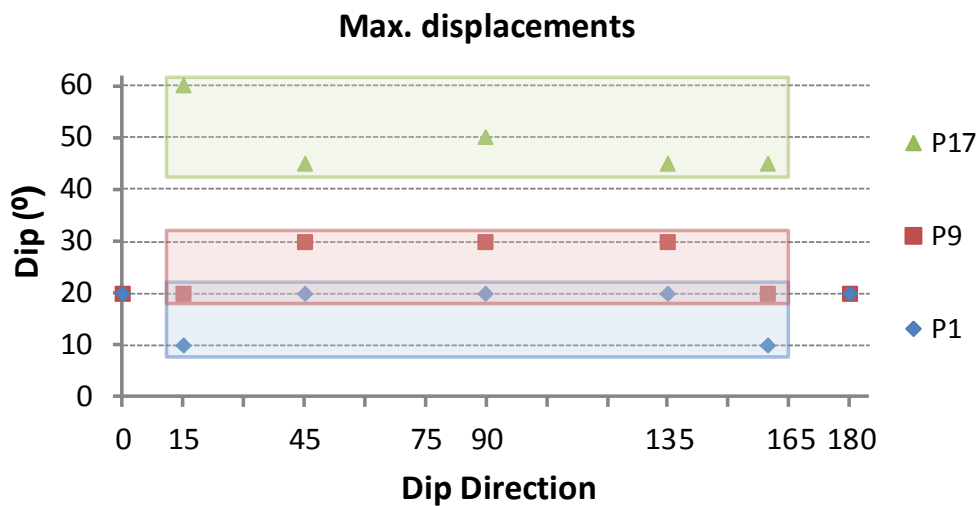


Fig. 79: Dip angle in which maximum displacements were registered for different dip directions

The results displayed in Fig. 79 are in agreement with the results shown in section 4.1.5 (Fig. 75) regarding displacement behavior for planes oriented close to DD000 and DD180. It was previously described that, as the dip direction rotates towards a parallel plane to the tunnel axis (e.g. DD015 and DD160), the dip angle, which exhibits greater influence, becomes lower. This trend can be seen in Fig. 79 where the dip angle in which P9 and P1 yielded maximum displacement values, is lower for DD015 and DD160 than for DD045, DD090 and DD135.

The variation of displacements for different dip directions is shown in Fig. 80 (the dip angle in the figure is fixed to 45°). The figure shows a symmetrical behavior with lowest displacement values for DD000 and DD180 and, for weakness planes not aligned to the tunnel axis, maximal displacement values for DD090. Note that symmetry of weakness planes is expected for dip directions DD135, DD220, DD270, DD315 and DD345. The plot in Fig. 80 also displays larger weakness plane influence towards the side-wall. Note that Fig. 79 does not include the weakness plane dipping 0° , which constitutes a common plane for all dip directions.

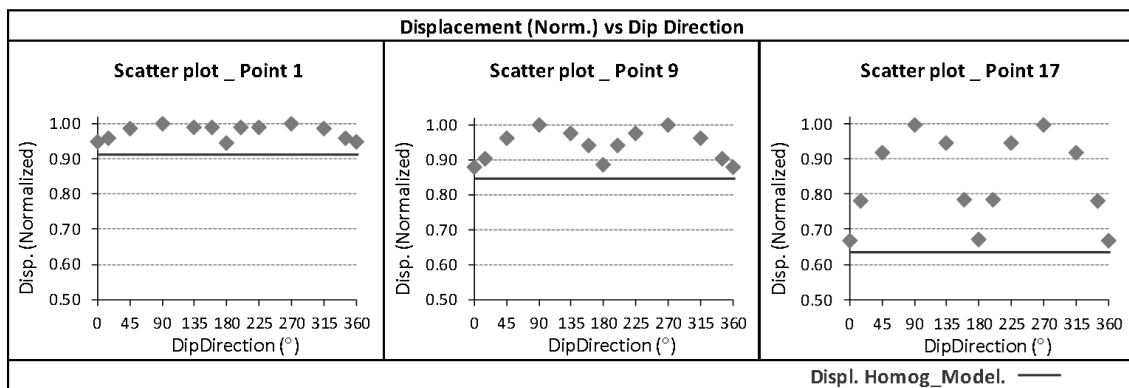


Fig. 80: Scatter plots, Displacements vs. Dip directions

The scatter plots for beta and alpha are plotted as a difference (Δ) with respect to the values resultant from the homogeneous model. The difference is a proper standardization aiming towards the prediction tool implementation (see chapter 6).

Entailed in Fig. 81 is the scatter plot of delta beta and delta alpha, for different dip angles and a fixed dip direction (DD045). Again, the scatter plots highlight the incremental difference toward the side-wall. Additionally, both beta and alpha display a maximum variation for a dip angle equal to 45° with the exception of alpha for monitoring point P1 where the maximum variation takes place at a lower dip angle (20°).

Form Fig. 81 two additional trends can be described, on the one hand beta displays a clockwise rotation (decreasing tangential displacements), represented as a negative value with respect to the rotation yielded by the homogeneous model (as the dip angle increases, the angle rotates to its initial position). On the other hand, alpha behavior is framed by a rotation against the direction of tunneling, this behavior trend was observed for tunneling in the same dip direction of the weakness plane (e.g. DD000, DD015 and DD045) (sections 4.1.1 and 4.1.4).

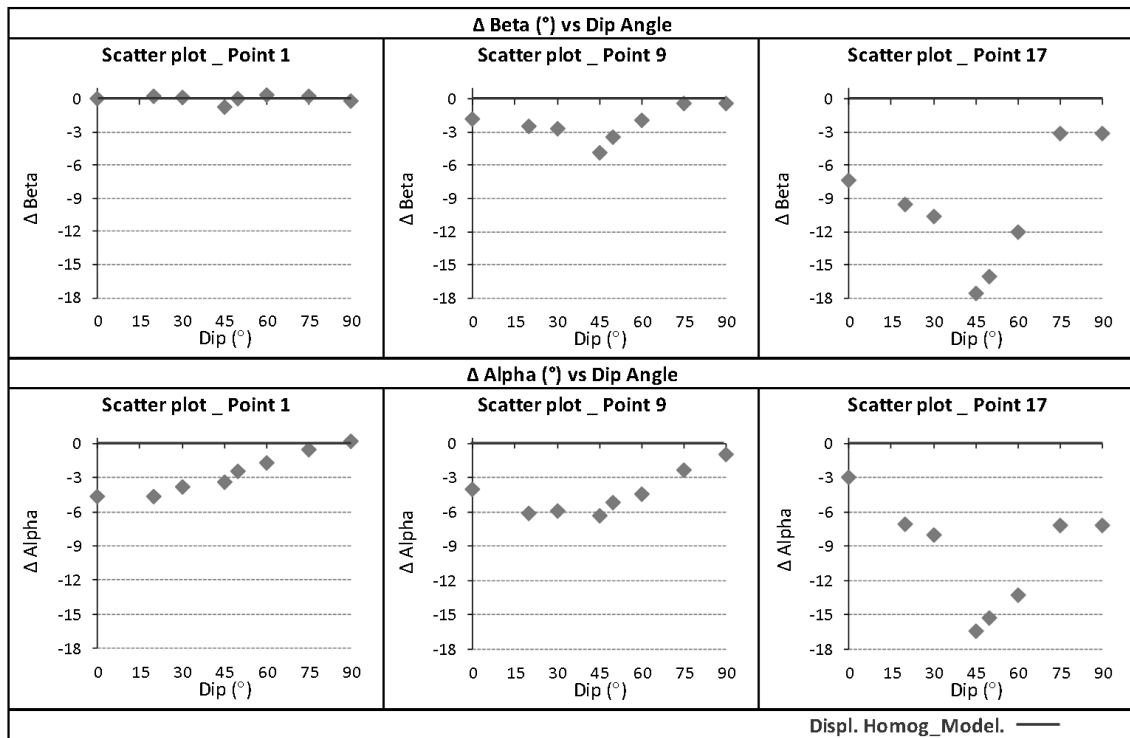


Fig. 81: Scatter plots, Displacements vs. Dip directions

Fig. 82 was assembled in order to check, if the observation regarding the maximum variation of beta and alpha at a dip angle equal to 45°, applies for other dip directions. The figure shows, on the left hand side, that the mentioned observation fits the behavior shown for DD045, DD090 and DD135. The behavior of the planes orientated perpendicular to the tunnel axis (DD000 and DD180) is framed by low dip angles (20°- 30°). Note that the beta plot, for DD000 and DD180, does not include the monitoring point P1, where no variation is expected (Fig. 39).

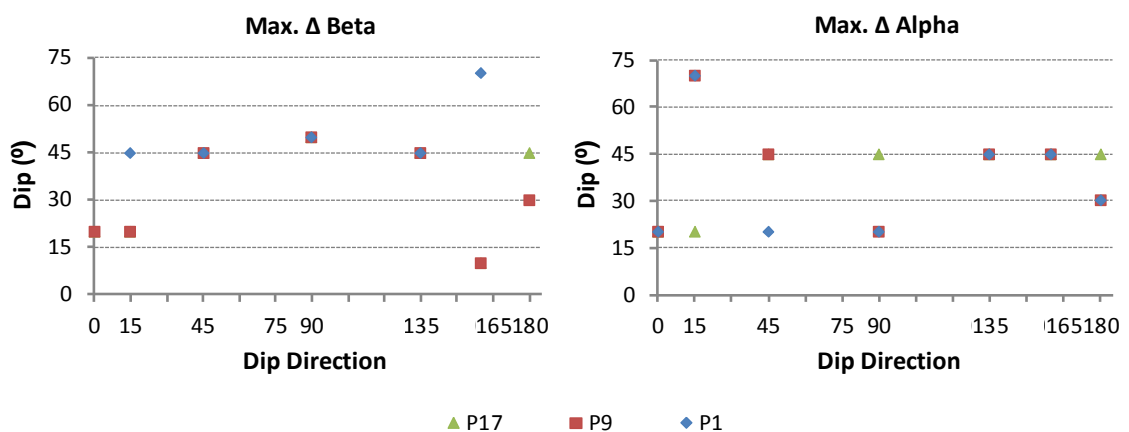


Fig. 82: Dip angle in which maximum beta (left) and alpha (right) rotation were registered for different dip directions

The rotation of alpha, right hand side of Fig. 82, does not display a generalized trend; the maximum rotation at a dip angle of 45° is observed for DD135 and DD160. However, it should be noted that in the case of alpha, unlike beta, the

same dip direction displays a rotation against and in the direction of the excavation depending on the dip angle; this is mainly observed for dip direction orientated towards the tunneling excavation ($270 < DD < 090$) as seen in sections 4.1.1 and 4.1.4. The situation can be visualized in Fig. 40, Fig. 48 and Fig. 60. The figures display the angle rotation depending on the dip angle and, additionally, a steadier trend for alpha can be observed for dip angles orientated against the direction of the excavation ($090 < DD < 270$). In this case, most monitoring points rotate towards the direction of the excavation.

The incremental difference on monitoring points towards the side-wall is also shown in Fig. 83 and Fig. 84. The figures display the behavior of beta and alpha, respectively, for different dip directions and multiple dip angles.

Fig. 83 visibly displays a maximum rotation of beta for dip direction equal to 090 (270) independent of the dip angle. It is also seen that dip angles between 30° and 60° display higher values than those yielded by other dip angles; this behavior has been seen for beta rotation throughout this study (section 4.1).

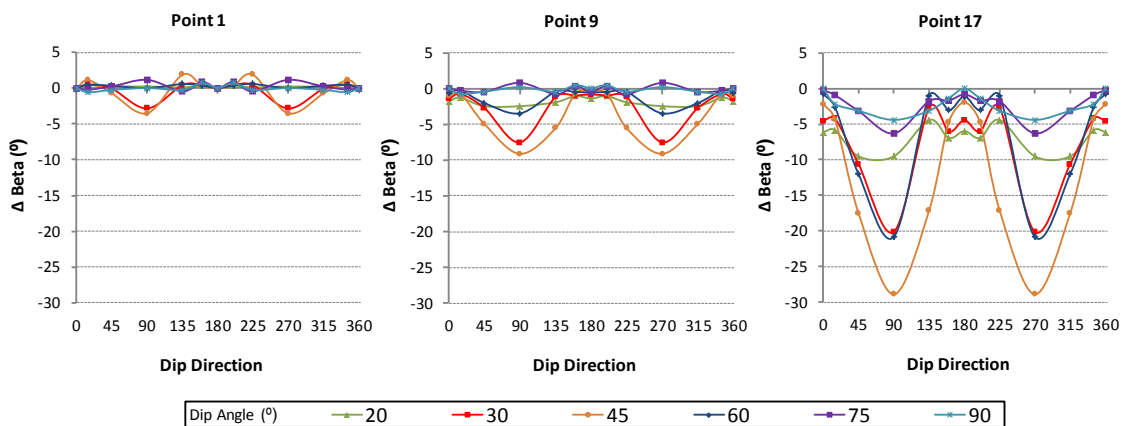


Fig. 83: Beta behavior at different dip directions and dip angles

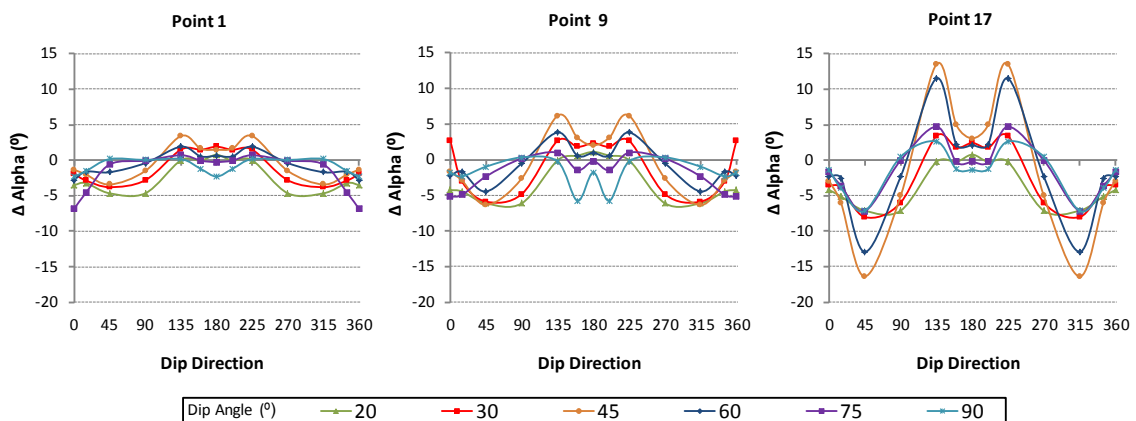


Fig. 84: Alpha behavior at different dip directions and dip angles

Fig. 84 displays the rotation of alpha for multiple dip angles and dip directions. Alpha behavior, similar to the one displayed by beta in Fig. 83, shows higher

rotations for dip angles between 30° and 60° and maximum values for a dip angle equal to 45° . However, unlike the rotation of beta, alpha's maximum values are reached for acute angles between the tunnel axis and weakness plane dip direction (e.g. DDD045 and DD225); this behavior has previously been observed in section 4.1 (Fig. 60).

It is worth highlighting that Fig. 83 and Fig. 84 were assembled considering symmetry of weakness planes, the figures display the differences of angle taking the rotation yielded by the homogenous model as reference. Also note that rotation of beta for dip direction $270 < DD < 360$ in Fig. 83 was assembled, for better visualization, following a different convention system than the one displayed in Fig. 20 and Fig. 21, where positive or negative value depends on a clockwise or counter clockwise rotation. The convention used in this case, independent of the side-wall, are taken as negative if the rotation takes place towards the center of the tunnel and positive for an opposite rotation.

5.3. Practical Application

The application of this work is for rock masses which display statistical homogeneity in joint properties and spacing. The areas of application are interdependent and can be separated into its applicability into projects stages:

- **Design:** during this stage a complete understanding of the ground “normal behavior” is needed in order to determine excavation sequences and support requirements, which leads to a system behavior to be monitored during construction.
- **Construction:** the stage is framed by a verification of the assumption made during design through monitoring and, if needed, adjustment of the geological model, support requirements and excavation sequence, all tasks aimed to conduct an efficient and safe tunneling.

5.3.1. Design stage

Section 2.3.1 described the shortcoming of traditional approaches used for excavation sequence and support design. The approaches mainly present either basic recommendations regarding support requirements [3-9] or smeared discontinuities into a continuum, by decreasing the overall rock mass properties [10]. Further on, section 3.4.3 displayed the incapability of such approaches to accurately display the ground behavior influenced by a weakness plane.

Design of excavation sequences and support selection is based on a clear understanding of the ground behavior [1], in other words, the failure mechanism that governs the ground [15]. The mechanism and trends described in chapter 5, allow designer to foresee difficulties, during tunneling and deliver design according to the requirements.

The implementation of the finding during design shall be done considering the weakness plane relative orientation to the tunnel axis and a dip angle, given by a geotechnical model, and could be divided into:

1. Consistent support design based on overstress areas by concentrating the support elements on the area of the intrados where higher displacements are expected (due to stress concentration caused by the weakness planes).

A proper example can be made using the observation made in section 5.1.2 for weakness planes orientated parallel to the tunnel axis (DD090) and a dip angle of 50° . Fig. 51 displays the stress condition on the cross section and, accordingly, section 4.1.3 describes that the area close to monitoring point 17 is expected to yield larger displacements. Fig. 85 displays on the left, the support requirements achieved smearing the weakness plane by decreasing the ground properties and, on right, a support design consistent with the areas expected to have higher stresses.

A consistent design could represent savings by relying on the ground structure, aiming the support towards areas where it is needed or, even if the same amount of support is implemented, a safer and more efficient tunneling can be achieved.

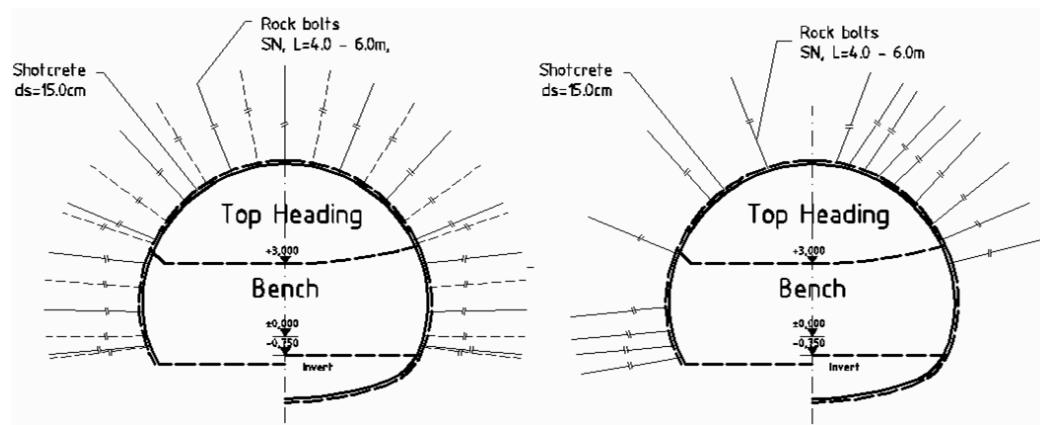


Fig. 85: Design considering for homogeneous ground (left) and ground considering discontinuities influence (right)

This example could be extrapolated to odder dip direction/dip in which the weakness plane has a direct influence on the displacement behavior (section 5.1) or to implement support updates or adjustments during construction (section 5.3.2).

2. Determination of System Behavior, in layered rock masses, can be partially determined taking into consideration the observations of this study.

During design a normal range of vector rotation and displacements magnitude should be given, although this range is influenced by support measures and excavation sequences, it is at the same time directly influenced by the ground behavior. The determination of this range allows the implementation of further tools such a prediction of ground conditions ahead of the face, in which

variation of the ground is predicted based on trend variation with respect to a given normal range [44] [76] (Fig. 87).

3. Expected tunneling conditions can be assessed based on the observation made in section 4.1 and 5.1 regarding displacements ahead of the face (pre-displacements). Fig. 49 and Fig. 62 compare pre-displacements for weakness planes dipping towards (DD000 and DD045) and against (DD045 and DD225) the direction of tunneling.

The results yielded differences up to 10% more pre-displacements for tunneling in the direction of the weakness plane than against it. Implying better conditions for tunneling in the same direction of the weakness plane, since higher displacements ahead of the face entails lower support requirements.

5.3.2. Construction stage

The implementation of the finding at this stage is necessarily linked to the design stage. In tunneling, unlike other civil engineering disciplines, the final designs are only achieved during construction by adjusting design of previous stages, to the found ground conditions and verifying its effectiveness through monitoring.

This support concept addressed in section 5.3.1 was successfully implemented in 2013 in tunnel 6A of the Bogota-Villavicencio road (Geology: Graphitic phyllites, Overburden: 140m, Tunnel axis: N35°W, Foliation: DD040dip40°, Relative orientation: DD075). Initially a symmetrical design was implemented leading to difficulties (over breaks) on the right side-wall (between 1h and 2h). In this case the number of bolts remained unchanged; however, they were redistributed densifying bolting on the overstressed areas. The example of tunnel 6A shows that the findings could be applied for improvement/update support systems and represents a tool to justify changes during construction.



Fig. 86: Tunnel 6A, road Bogota-Villavicencio

The normal range referred in section 5.3.1 is usually adjusted during construction. Any interpretation of monitoring data is based on a normal range. The range estimation is based on a complete understanding of the ground behavior, which for layered rock masses must include the weakness plane influenced, due to its orientation with respect to the tunnel axis. Fig. 87 portrays this situation during construction, up to chainage 1080 the displacement vector was within an estimated “normal range”, a variation of the ground conditions ahead can be predicted considering the displacement vector deviation from the “normal range”.

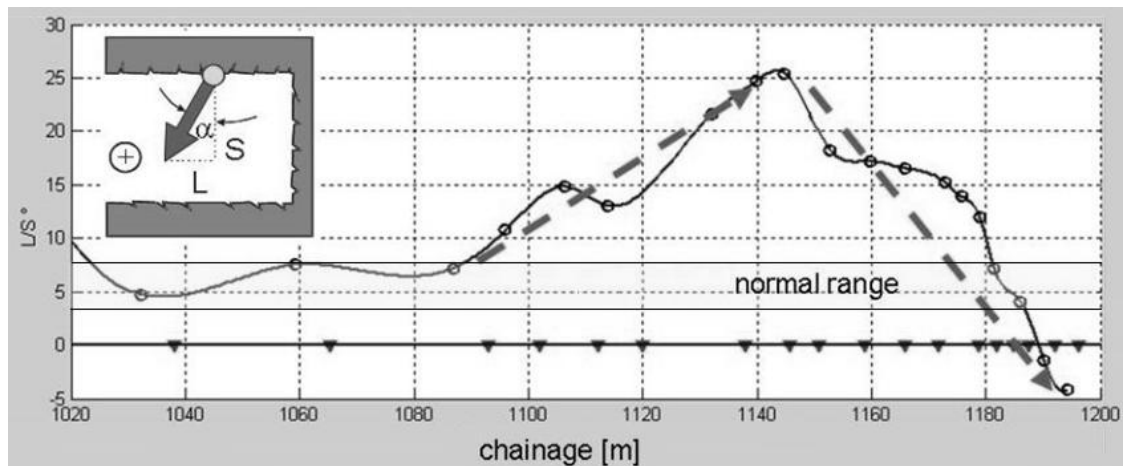


Fig. 87: Displacement vector deviation

5.4. Limitations and Recommendation for Further Investigations

The limitations of this work are set by the shortcoming of the implemented constitutive model (Ubiquitous Joint Model). It was mentioned in section 2.3.2 that the main drawback is the inclusion of only one shear component (no bending component) leading to displacements overestimation as the bending component is reduced to zero if the shear strength limit is reached.

The overestimation is caused by the weakness plane properties that in combination with the stress conditions lead to high displacements (stress concentration areas). The location of such areas, as previously addressed, depends on the relative orientation of the weakness plane to the tunnel axis.

Sections 4.1.4 and Fig. 79 present the location along the intrados where higher displacements are reached for DD045 with a dip angle of 30° . Fig. 88 makes use of this dip direction and dip angle to display the mentioned overestimation (displacements shown in the figure are normalized by the principal stress value). The figure clearly shows that the overestimation takes place for high stress conditions and only in the area where, according to this study, higher displacements are expected.

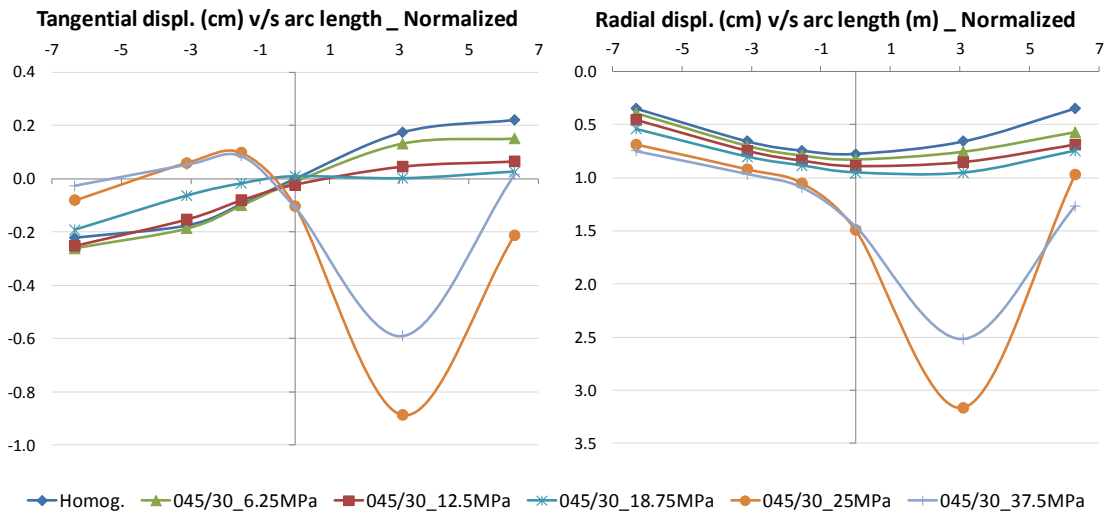


Fig. 88: Tangential and radial displacements for different stress conditions (DD045/Dip45)

A second example makes use of the result presented in section 4.1.5. Comparing the result of tunneling with (DD045) and against (DD135) the weakness plane orientation, yielded a difference between 6% and 11% for σ_1 equal to 6.25MPa and 12.5MPa respectively (see Table 9 for ground and weakness plane properties). Doing the same comparison for a higher stress condition (σ_1 equal to 25MPa) the increase reached was between 90%-150%.

It is worth mentioning that this increment, mainly takes place behind the face portion rather than ahead of it, where no detachment is possible. Fig. 89 shows the displacement contour plot for this discarded case. It shows the displacement behavior as the face distance from the monitored cross section increases; there are thresholds in which the weakness plane shear strength is exceeded, entailing detachment and leading to the mentioned overestimation.

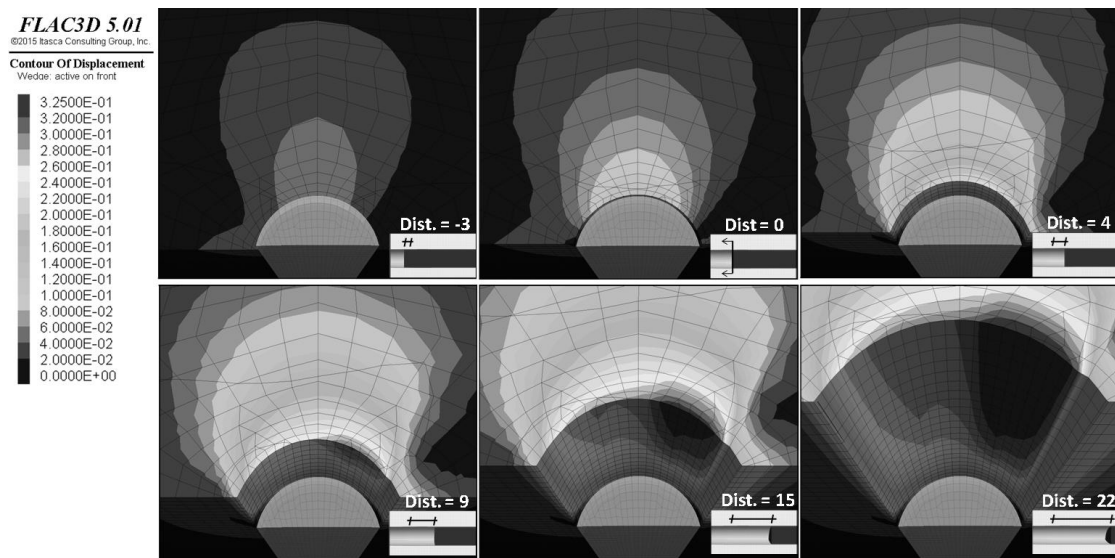


Fig. 89: Displacements contour plot for DD135/Dip45 ($\sigma_1 = 25\text{MPa}$)

The shortcoming does not allow reliable results if complete detachment takes place; on this basis, approximately 10 to 15% of the simulations were discarded and not included into the final results and analysis. However, it should be considered that, although there is an evident displacement overestimation, the general failure mechanism could be observed in the simulation output.

Fig. 90 shows the result of a scale model on the left and the numerical result on the right, the model was assembled for a DD270 and dip angle of 30° considering material with the same material properties shown in as Table 9 with the exception of the J_{coh} which was set to 0.1KPa, following the definition of joints given by Goodman [27] (joint shear strength with zero cohesion). The numerical model displays the same failure mechanism given by the scale model, with much larger displacements in the area where detachments takes place.

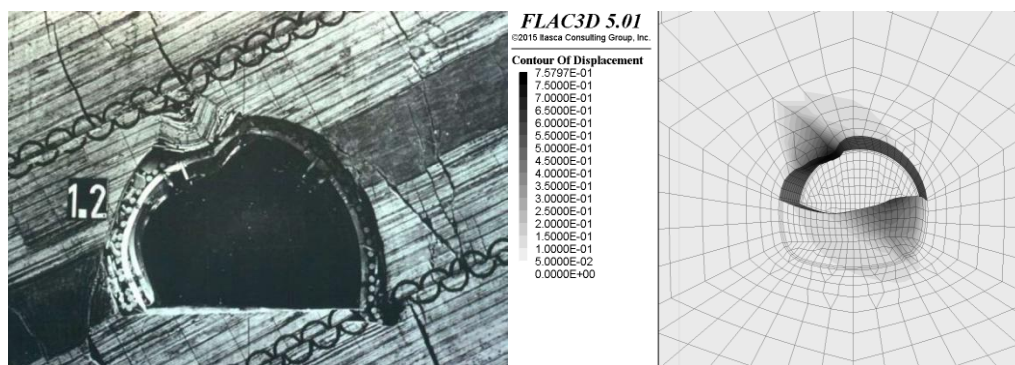


Fig. 90: Failure mechanism for DD270/Dip30 ($\sigma_1 = 6.25\text{MPa}$)

Highlighted in this section was the limitation of the ubiquitous joint model, to simulate large displacements. Additional tools or alternative constitutive models shall be used, when the failure mechanism displays detachment due to stresses induced on the excavation.

Future work should focus on the simplifications and assumptions that can be used in 3-D modelling while capturing the correct failure mechanisms, providing realistic results in complex rock mass structures. In an elastic state of the rock mass a continuum approach is suitable. However, the usage of more sophisticated constitutive models in order to assess the ground behavior, including detachment and large displacements, should be considered

Better results could be achieved considering that there has been important advances in continuum models (e.g. Cosserat continuum) and hybrid models discrete–continuum (e.g. Abaqus CAE). Behavior influencing factor must be considered when evaluating which simplifications should be made for designing underground excavations.

Future works should also consider a discrete approach taking into account its advantages when simulating discontinuities or weakness planes [1]. Although nowadays it is still difficult, due to time and computation glitches, to run very large amounts of 3D simulations with this approach, the on-going improvement in computational performance will allow the usage of such approaches in the near future.

6. INTERFACE FOR DISPLACEMENT BEHAVIOR PREDICTION

An interface was programmed in the computational software Matlab in order to summarize and facilitate the visualization of the findings. The prediction tool bases its displacement prediction on Feder's formulation [31] which, opposite to other closed form solutions, includes the lateral pressure coefficient into the calculation. Feder's basic prediction is extended to integrate the influence of the weakness planes on the displacements behavior.

Feder's prediction integrates the results and observations from the present study (see chapter 4 and sections 5.1 and 5.2) by accessing a database assembled to specify the magnitude of the variation, regarding displacement magnitude and orientation of the displacement vector. The variation of each monitoring point is governed by three different databases containing:

1. Magnitude variation,
2. Beta (2D) and
3. Alpha (3D) rotation.

The databases take into consideration the result yielded by the homogenous model as a bench mark. On the one hand, variation regarding magnitude is taken as a percentage (normalized value) with respect to the bench mark and on the other hand, beta and alpha rotation is taken as a delta difference (Δ) increasing or decreasing the orientation angle in relation to the bench mark.

Shown in Fig. 38 are the simulations performed for the present work, the database contains not only those simulation results but also displacement magnitude and rotation of the "weakness planes of symmetry".

The values of the performed simulations and planes of symmetry are taken as "Fix values" for a surface which contains the monitoring point magnitude variation and delta rotation. In order to assess all possible combinations of dip direction and dip angle the surface was assembled by means of a linear interpolation between the 3D scatter "Fix values" (e.g. x value: DD, y value: Dip angle and z value: Δ beta).

Fig. 91 presents an example of a surface containing the displacement magnitude (normalized) for monitoring point P9. The surface is assembled as a stereonet in which each surface point consists of 3 components: 1st dip direction, 2nd dip angle (the first two components allow determining the location of the weakness plane pole on the stereonet -upper hemisphere-) and, for this case, a correspondent magnitude variation for monitoring point 9. Observe in the figure how the "lightest area", representing the highest displacements variation for point 9, is located near a DD 090, in agreement with the observation made in section 4.1.3.

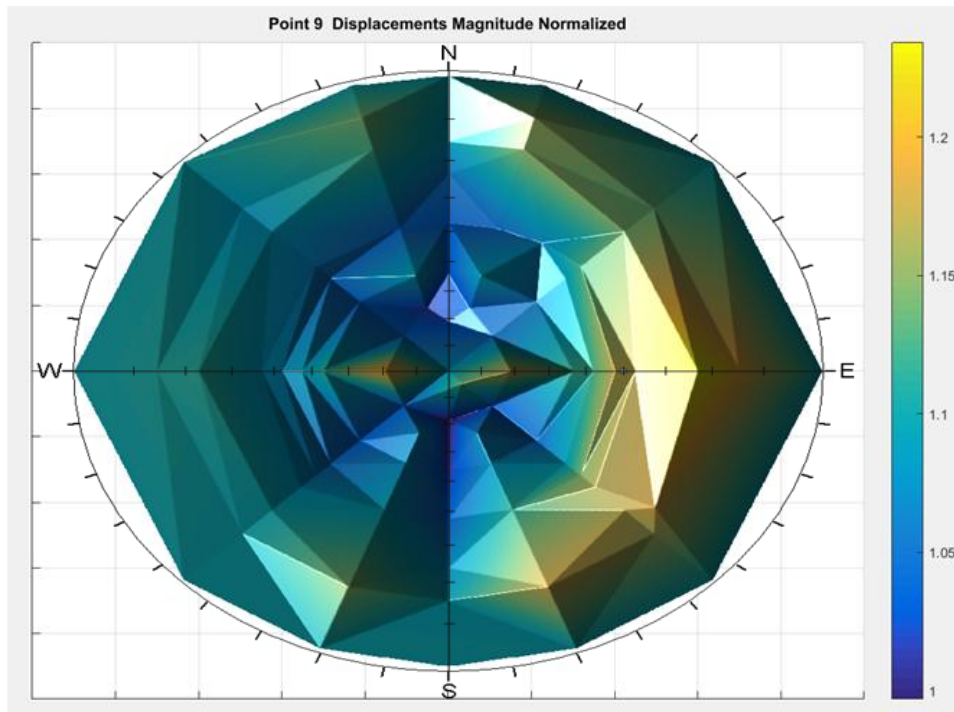


Fig. 91: Example of a surface summarizing displacement magnitude results, monitoring point P9

6.1. Interface Components

The interface is divided into “Input” and “Output” sections, located on the right and left hand side respectively (see Fig. 92).

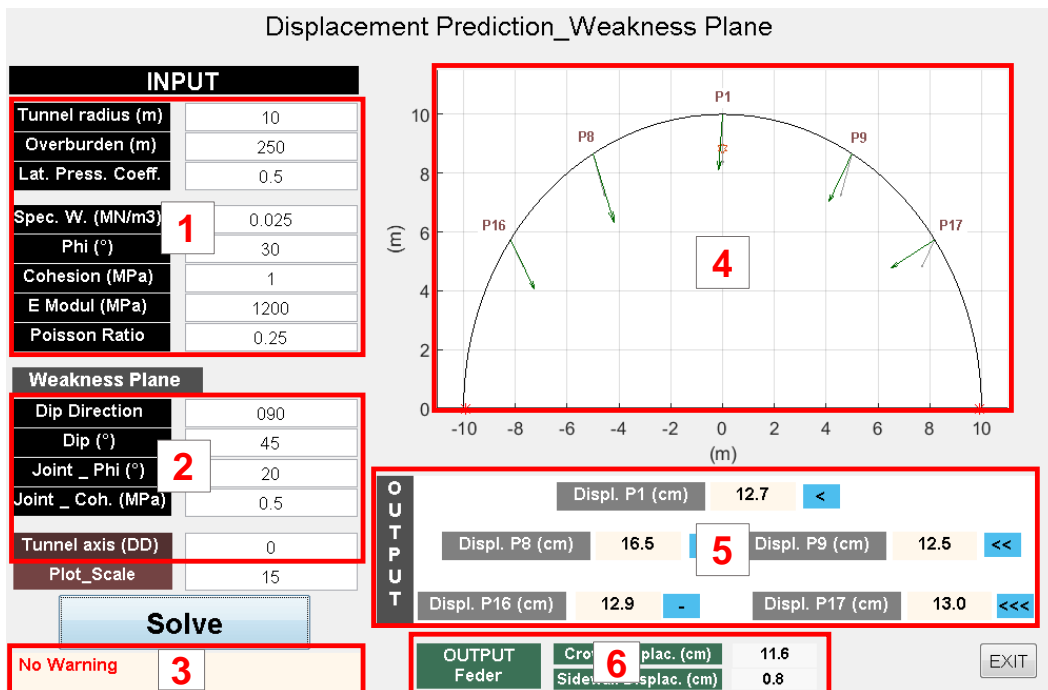


Fig. 92: Graphical user interface (GUI) for displacement behavior prediction

The interface includes an “EXIT” button used to terminate any calculation and/or to close the interface and a “Solve” button which either starts the prediction or displays a “warning” if a restriction is surpassed or if any input parameter should be checked by the user.

The following two sections describe the different components of the interface (the numbering in section 6.1.1 refers to the one shown in Fig. 92).

6.1.1. Input section

The input section gathers all data that enable the prediction to be made, including:

[1]. Feder’s basic solution Input data

The code initially calculates displacements in the tunnel crown and sidewall making use of the listed input data.

1.1	Tunnel Radius	(m)
1.2	Overburden	(m)
1.3	Lateral pressure coefficient	(--)
1.4	Specific weight	(MN/m ³)
1.5	Friction angle	(°)
1.6	Cohesion	(MPa)
1.7	Elasticity modulus	(MPa)
1.8	Poisson Ratio	(--)

At this stage the basic solution is extended to include intermediate points (P8-P9 and P16-P17) into the cross section (see Fig. 93). A function was programmed in order to evaluate center coordinates “Center F_{disp} ” and radius “Radius F_{disp} ” of a circle fitting the three coordinates delivered by Feder’s solution (x and y displacement coordinates for: 1st crown point, 2nd left side-wall and 3rd right side-wall)

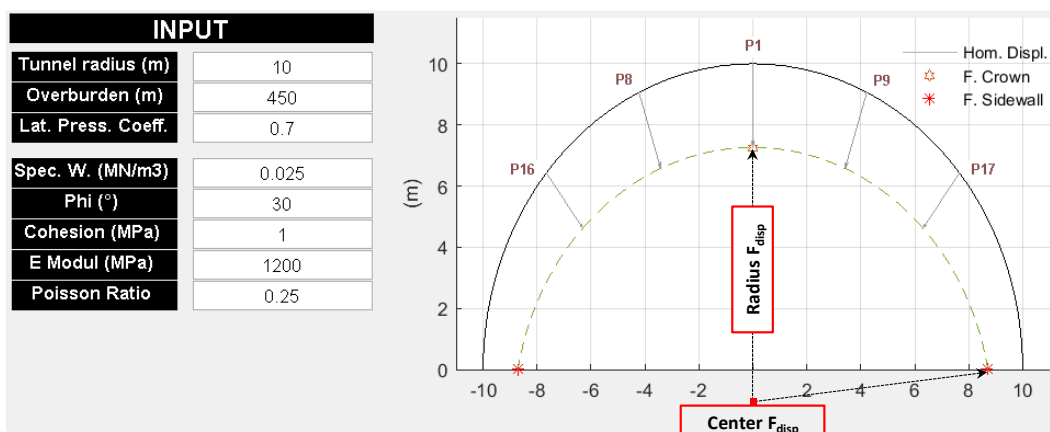


Fig. 93: Feder’s solution extension to include intermediate points

[2]. Weakness plane Input data: the following input values allow the access to the mentioned databases

- | | | |
|-----|-------------------------------|-------|
| 2.1 | Dip Direction | (°) |
| 2.2 | Dip angle | (°) |
| 2.3 | Weakness plane friction angle | (°) |
| 2.4 | Weakness plane cohesion | (MPa) |
| 2.5 | Tunnel axis orientation | (°) |

The orientation of the tunnel axis should be given as a dip direction. The interface internally calculates the relative angle between the orientation of weakness and tunnel axis.

Variation on the weakness planes' strength values are handled considering the calculated ratio between plastic radii of homogeneous model " $P_{Rad.matrix}$ " and of the weakness plane " $P_{Rad.WP}$ " (see section 5.1.5). The following figure summarizes this handling; note that even though the notation is for the angle rotation (sub-index " Rot "), the same handling is applied for alpha's displacement magnitude variation, due to the strength properties of the weakness planes.

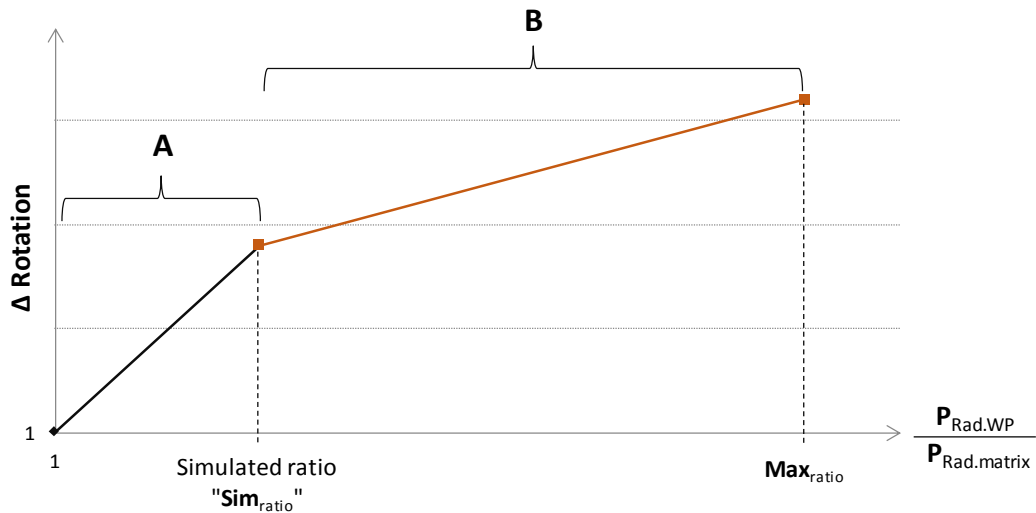


Fig. 94: Handling of weakness plane strength properties in the displacement characteristics

The equation describing the variation of the rotation in the range "A" is given by:

$$\Delta Rot P_{xx(A)} = S_{Rot(A)} \cdot \left[\frac{P_{Rad.WP}}{P_{Rad.matrix}} - 1 \right] + 1 \quad \text{Eqn. 9}$$

$$\text{with } S_{Rot(A)} = \frac{Sim_{Rot} P_{xx} - 1}{Sim_{ratio} - 1}$$

The equation describing the variation of the rotation in the range "B" is given by:

$$\Delta \text{Rot}P_{xx(B)} = S_{\text{Rot}(B)} \cdot \left[\frac{P_{\text{Rad.WP}}}{P_{\text{Rad.matrix}}} - \text{Sim}_{\text{ratio}} \right] + \text{Sim}_{\text{Rot}} P_{xx} \quad \text{Eqn. 10}$$

$$\text{with } S_{\text{Rot}(B)} = \frac{\text{Sim}_{\text{Rot}} P_{xx} \cdot \text{Perc}_{\text{Rot}} - \text{Sim}_{\text{Rot}} P_{xx}}{\frac{P_{\text{Rad.WP}}}{P_{\text{Rad.matrix}}} - \text{Sim}_{\text{ratio}}}$$

Where

$\Delta \text{Rot}P_{xx(A/B)}$	Rotation variation for the monitoring point “xx”
$P_{\text{Rad.WP}}$	Plastic radius yielded by the weakness plane strength properties
$P_{\text{Rad.matrix}}$	Plastic radius yielded by the ground properties
$S_{\text{Rot}(A/B)}$	Gradient of the curve for the range “A/B”
$\text{Sim}_{\text{Rot}} P_{xx}$	Simulated variation accessed via the database
$\text{Sim}_{\text{Ratio}}$	Simulated ratio between plastic radii
Perc_{Rot}	Maximum increase with respect to the simulated value

Included in the database is the value “ $\text{Sim}_{\text{Rot}} P_{xx}$ ”, the value is access by the code with the input parameters DD and Dip angle.

Due to the shortcomings of the ubiquitous joint model (section 2.3.2), a maximum rotation “ Perc_{Rot} ” is set. This value is limited by the two restrictions set for the prediction (section 5.1.5): 1st “ $\text{Max}_{\text{ratio}}$ ” between Plastic radii $P_{\text{Rad.matrix}}$ and $P_{\text{Rad.WP}}$ and 2nd a maximum value for the $P_{\text{Rad.matrix}}$. Note that the $\text{Max}_{\text{ratio}}$ depends on the DD (section 4.1) (Fig. 94).

[3]. Warning messages

The prediction is preformed if no “warning messages” appear after pressing the “Solve” button. The conditions will generate a warning message:

3.1 Erroneous orientation of the tunnel axis

Warning: “Tunnel axis Dip Direction between 0 and 360”

3.2 Erroneous Dip direction value

Warning: “Dip Direction between 0 and 360”

3.3 Erroneous Dip angle value

Warning: “Dip angle between 0° and 90°”

3.4 Limitations for lateral pressure coefficient

Warning: “Lateral pressure coefficient between 0.3 and 2”

3.5 Weakness plane’s strength properties exceeding those from the matrix

Warning: “Check WP strength properties”

3.6 Violation of the restrictions regarding ubiquitous joint model prediction (section 5.1.5)

Warning: “Displacement overestimation due to Ubiquitous Joint Model limitations”

The “Plot_Scale” input value controls the scale of the displacement vector graphical representation included in the interface’s section [4].

6.1.2. Output section

The output section is divided into a graphical representation, displacement prediction magnitude and a qualitative indication of the variation of alpha.

[4]. Displacement behavior graphical representation

- 4.1 Graphical representation of the displacement vector yielded by Feder’s prediction (gray arrow)
- 4.2 Graphical representation of the displacement vector influenced by the weakness plane (green arrow)

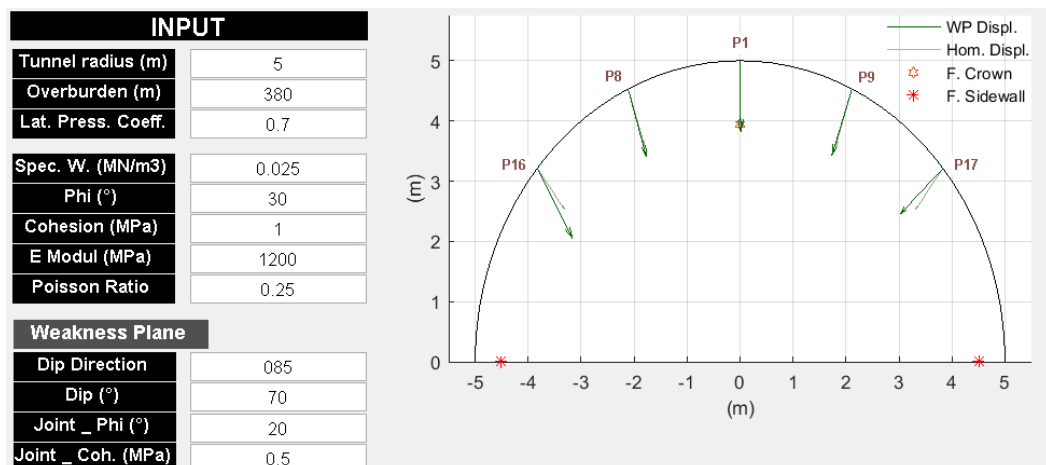


Fig. 95: Graphical results delivered by the interface

Beta rotation, due to the weakness plane influence, is included as a “green arrow” in the cross section shown in Fig. 95.

[5]. Displacement prediction values for monitoring points and qualitative reorientation of the angle alpha

5.1 Displacement prediction for the assessed monitoring points

The displacement magnitude is displayed in cm. Notations for each monitoring point (e.g. “Displ. P17”) refer to the ones in the graphical representation, see Fig. 95.

5.2 Alpha rotation

The differential rotation of alpha (Δ), with respect to the angle yielded by the homogeneous model, is displayed in a qualitative form.



Fig. 96: Results deliver by the interface

The number of signs “less-than” or “more-than” indicate the quantitative rotation either against the direction of tunneling (e.g. <<) or towards the tunneling direction (e.g. >) (for conventions see Fig. 20). The maximum number of “less-than” or “more-than” signs is 3, if the delta rotation is less than + 0.5° the sign “-” is displayed.

[6]. Feder’s basic solution output

- 6.1 Tunnel crown displacement (cm)
- 6.2 Tunnel side-wall displacement (cm)

6.2. Interface Assessment with Monitored Displacement Data

Displacement monitoring data are used in this section in order to verify the capability of the developed interface to deliver appropriate results. The behavior predicted by the interface is compared in terms of displacement magnitude and displacement vector rotation, on the cross and longitudinal section.

It should be acknowledge that the prediction tool, unlike the displacement monitoring data used for the comparison, delivers the prediction of the “ground behavior” where no considerations of support elements or excavation sequence is included into the calculation. Therefore, the assessment presented in this section focuses not on the magnitude but rather on trend prediction, regarding displacement vector rotation and its magnitude. Taking this into consideration, a set of parameters, for the matrix and the weakness plane, was chosen for each cross section aiming to exceed the monitored displacements; the main focus is centered on assessing the influence of the weakness plane in the overall displacement behavior.

The assessment used displacement monitoring and geological data from the Galgenberg tunnel [83], Strengen tunnel [87] and Inntal tunnel [88]. The mentioned tunnels were selected considering that they were partially excavated on a layered rock mass (schists, phyllites, slates, and quartz-phyllites) and considering that data regarding the 3D displacement monitor system as well as the geological characteristics (geological face mapping), are available. Considering that the implemented monitoring system for the projects located 3 monitoring targets on the top heading, the prediction tool makes used of points P1, P16 and P17 (see

section 6.1.1) which roughly match the location of monitored targets installed and monitored on-site.

6.2.1. Galgenberg tunnel

Two cross section of the Galgenberg tunnel (Jassing drift) were used for the calibration conducted for the ubiquitous joint model (see section 3.4). In this section for the assessment of the prediction tool, the displacement monitoring data of two monitoring station are compared with the results delivered by de prediction tool, the station 0+290 of the Jassing drift and station 0+770 from the Leoben.

Fig. 97 displays the predicted displacements and the displacements monitoring data documented during excavation, on the left and right hand-side respectively. The figure is useful to visualize the quantitative variation of alpha (longitudinal section) yielded by the prediction tool (see Fig. 96). Although displacement monitoring data show a slight rotation against the direction of tunneling for the 3 monitoring points, the prediction tool only captures the behavior at monitoring point 1 with the symbol “<” and for monitoring points 17 with the symbol “<<<”.

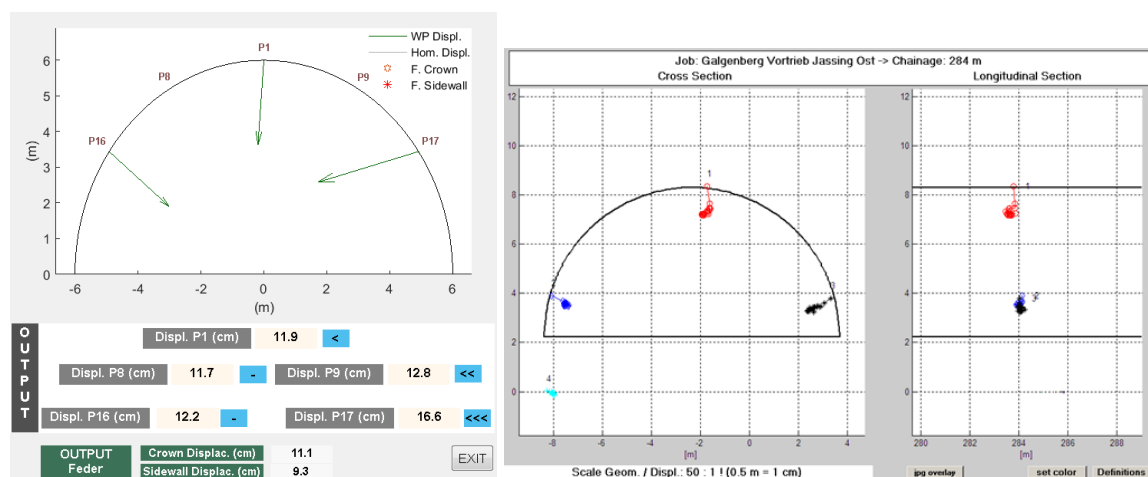


Fig. 97: Displacements prediction and monitored data (Geofit®) _ Galgenberg tunnel, cross section: k 0+290

Summarized in Fig. 98 are the principal components needed to assess the prediction tool on the cross section, including: basic information of the monitored section (overburden, Fisher concentration contour plot, ground and weakness plane parameters, etc.), a graphical representation of the monitored and predicted displacements, sketch of the geological situation and magnitude of displacements presented in centimeters and normalized by the maximum displacement among the evaluated monitoring points. The information contained in Fig. 98 is used as a template in this section to conduct the assessment of the prediction tool.

It was previously mentioned that the magnitude of displacements are not directly assessed, however, its normalized values easily display the general trend of the overall displacement behavior. In this case, monitored data showed the maximum displacement for point 16, followed by point 17 and the minimum value is

registered at point 1, the displacement prediction follows the same pattern. Regarding beta rotation, the prediction tool shows a comparable counter clockwise rotation for monitoring point 16, the rotation registered at monitoring points 1 and 17 are significantly larger than the ones predicted by the tool.

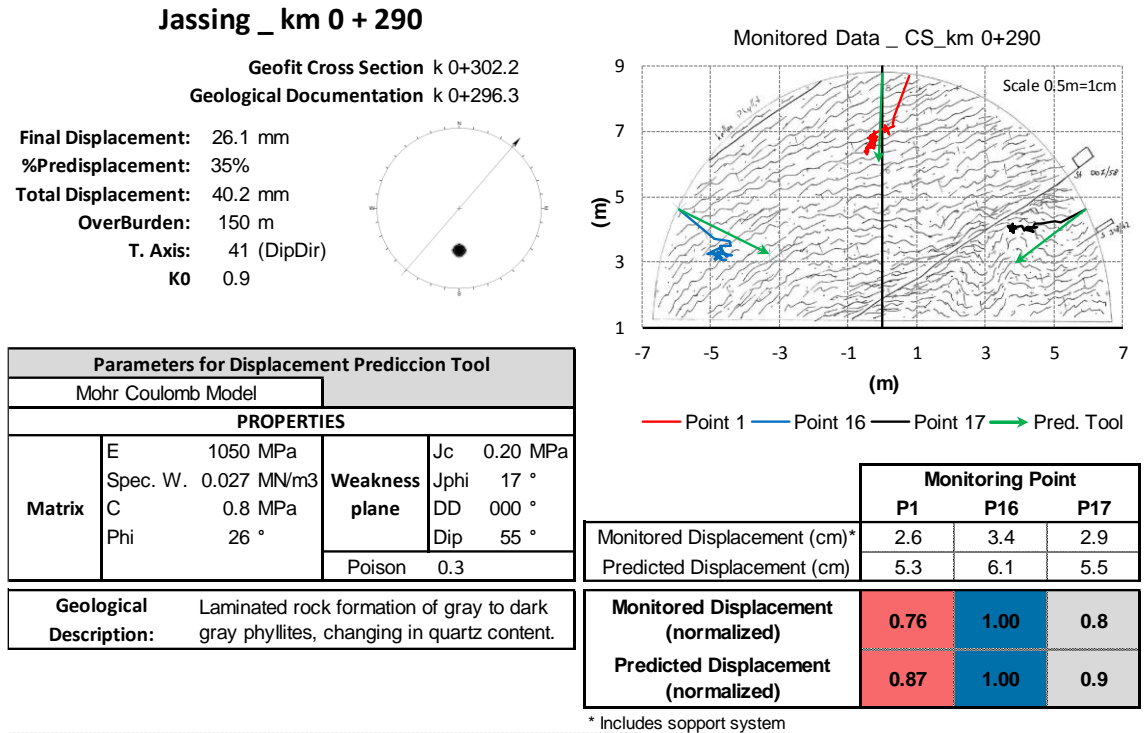


Fig. 98: Comparison between monitored and predicted displacements _ Galgenberg tunnel, cross section: k 0+290

Monitoring section 0+770 of the Galgenberg tunnel is shown in Fig. 99.

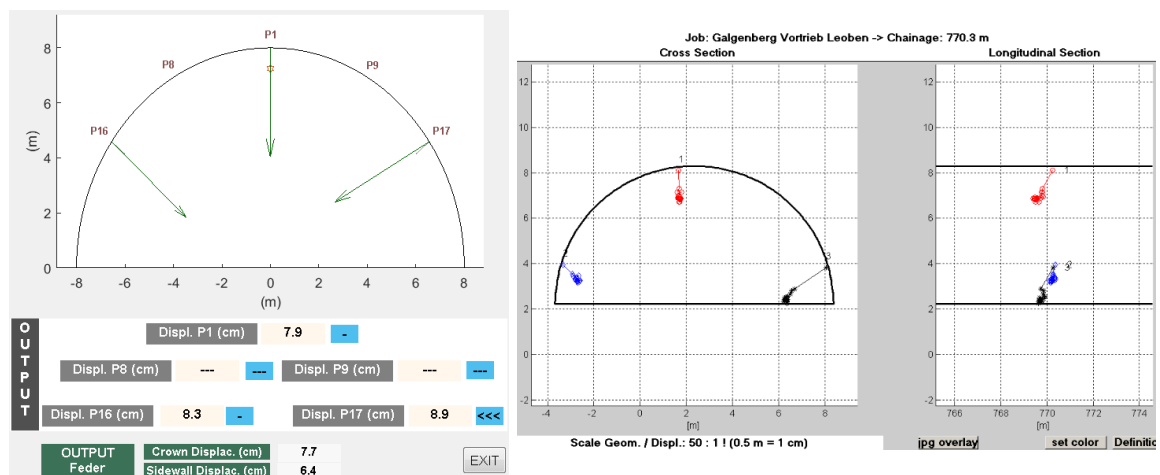


Fig. 99: Displacements prediction and monitored data (Geofit®) _ Galgenberg tunnel, cross section: k 0+770

The quantitative prediction (alpha rotation) shows a rotation against tunneling direction only for monitoring point 17. The trend is common for the three monitoring points, however, the prediction tool displays it only on the monitoring with the larger displacements (point 17). This could be due to the multiple geological structures documented on the excavation face.

On the cross section, the monitoring data and the prediction tool show a small rotation at monitoring point 1 (see Fig. 100). However, the rotation documented on site is counter clockwise and the predicted rotation is on the opposite direction (clock wise). The displacement prediction for points 16 and 17 roughly follow the monitored data; it can be seen that at point 17 predicted and monitored data display a clockwise rotation, clearly caused by the influence of the weakness plane.

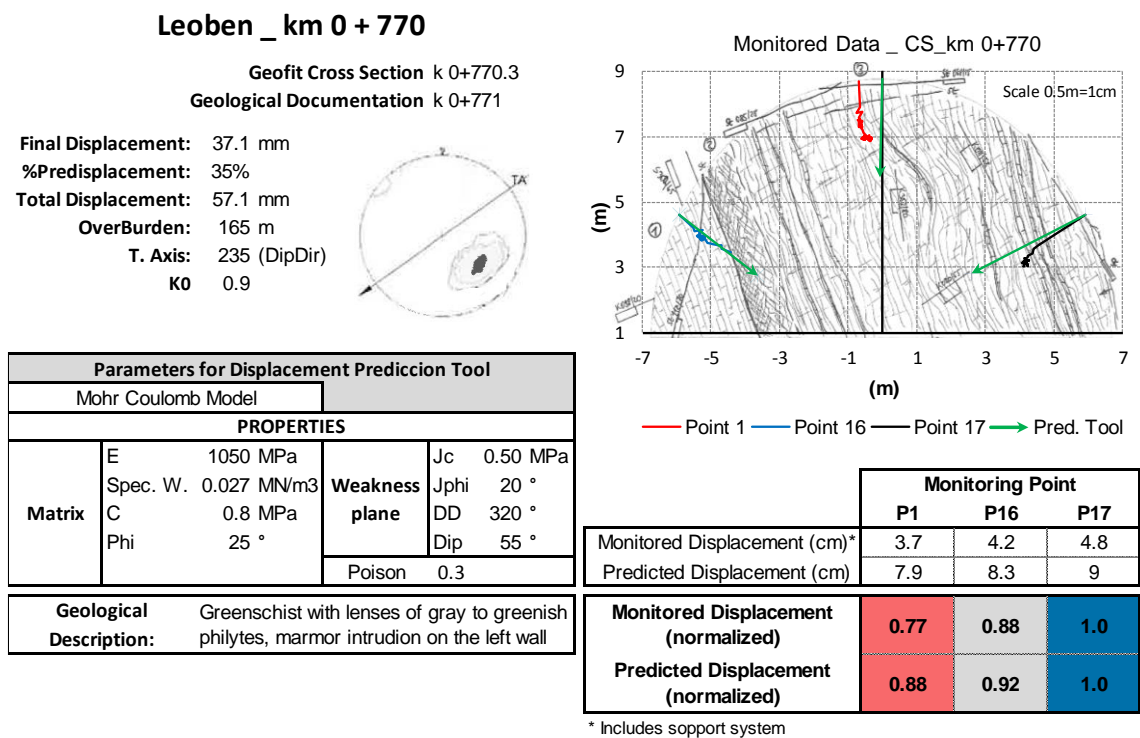


Fig. 100: Displacements prediction and monitored data (Geofit®) _ Galgenberg tunnel, cross section: k 0+770

6.2.2. Strengen tunnel

Cross sections k 2+025 of the Strengen was used for assessment purposes. Taking into consideration that the cross sections displays rather large displacements, it should be noted that the restriction mentioned in sections 5.1.5 and 6.1.1, had to be partially lifted to allow the prediction. The restriction does not play a major role in this case considering that displacements are not being compared in terms of magnitude but rather as a trend (see section 5.4).

The monitored section is displayed in Fig. 101. The figure shows that the monitored displacements present a rotation is well matched by the qualitative prediction of the tool. The vector rotation matches the rotation towards and against

the tunneling direction, for monitoring point 1 displaying “>” and monitoring point 16 displaying “<” respectively. The rotation display by monitoring point 17 is not captured by the prediction tool.

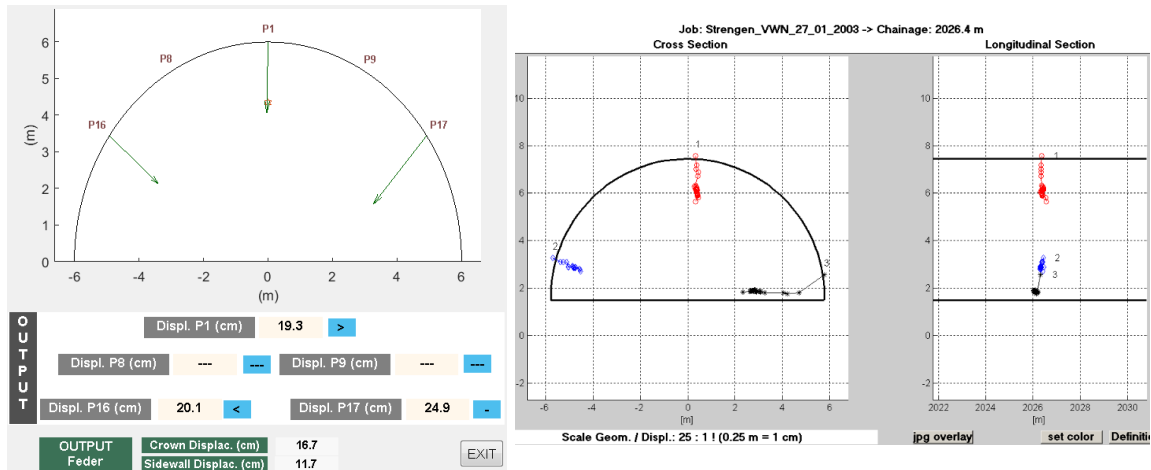


Fig. 101: Displacements prediction and monitored data (Geofit®) _ Strengen tunnel, cross section: k 2+025

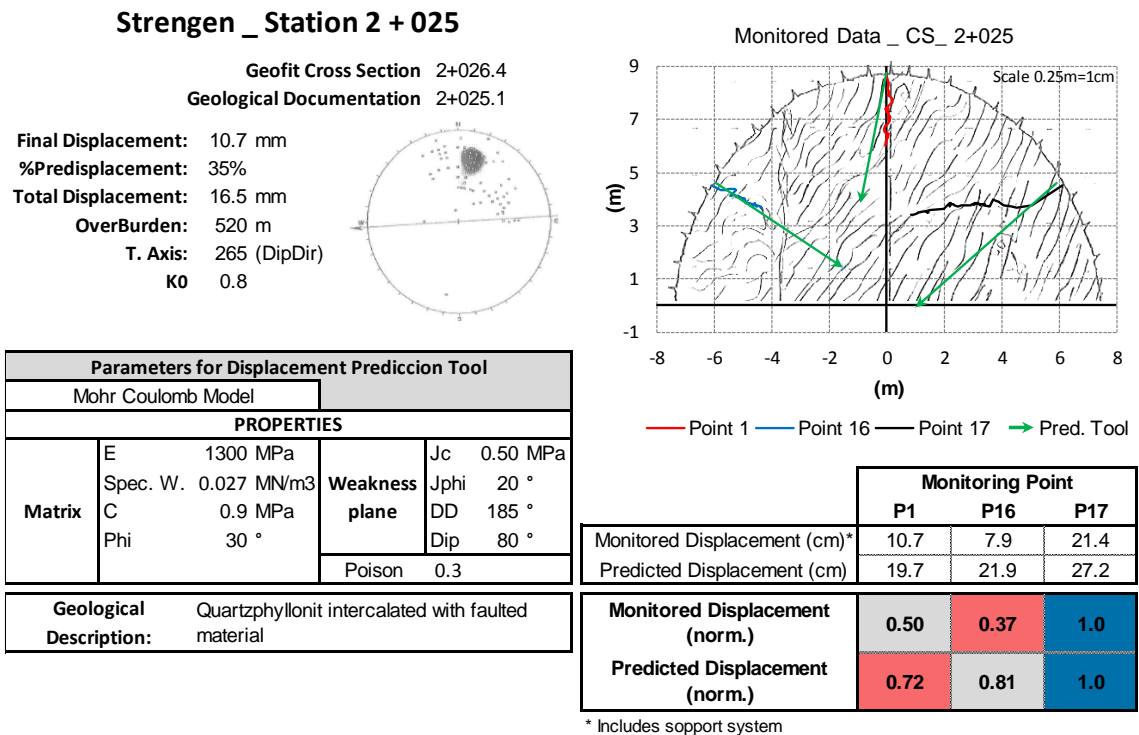


Fig. 102: Comparison between monitored and predicted displacements _ Strengen tunnel, cross section: k 2+025

The general monitored trend on the cross section is portrayed by the prediction tool in Fig. 102. The displacement prediction matches the rotation at monitoring point 16. Monitoring data for point 1 yielded almost no rotation, however the prediction yielded a clockwise rotation. Although the prediction tool displays clockwise rotation, the monitoring data for monitoring point 17 showed a much

larger rotation than the one predicted (see Fig. 102). Regarding magnitude trend the prediction tool matched the large displacements documented at monitoring point 17.

6.2.3. Inntal tunnel

During the construction of the Inntal tunnel large displacements were recorded during the monitoring campaign. For this prediction and opposite to the situation presented for the first cross section evaluated for the Stregen tunnel (k1+611), the restriction set for the prediction tool were not lifted. As previously mentioned (section 6.2.2) there is no impact on the assessment conducted in this section, since displacements are being compared in terms trends in the overall section.

Cross section k 3+364 at the Inntal tunnel exhibits a relative flat weakness plane (dip 20°), orientated towards the direction of tunneling (relative orientation with respect to the tunnel axis equal to 015); the cross section was selected considering that it presents a different relative orientation than the previously assessed cross sections.

For the longitudinal section, a rotation against the direction of tunneling was documented during construction, the trend is well matched by the prediction tool for monitoring points 1 and 16. For monitoring point 17, the tool predicts a significant rotation against the tunneling direction, which does not match the minor rotation monitored during construction (see Fig. 103).

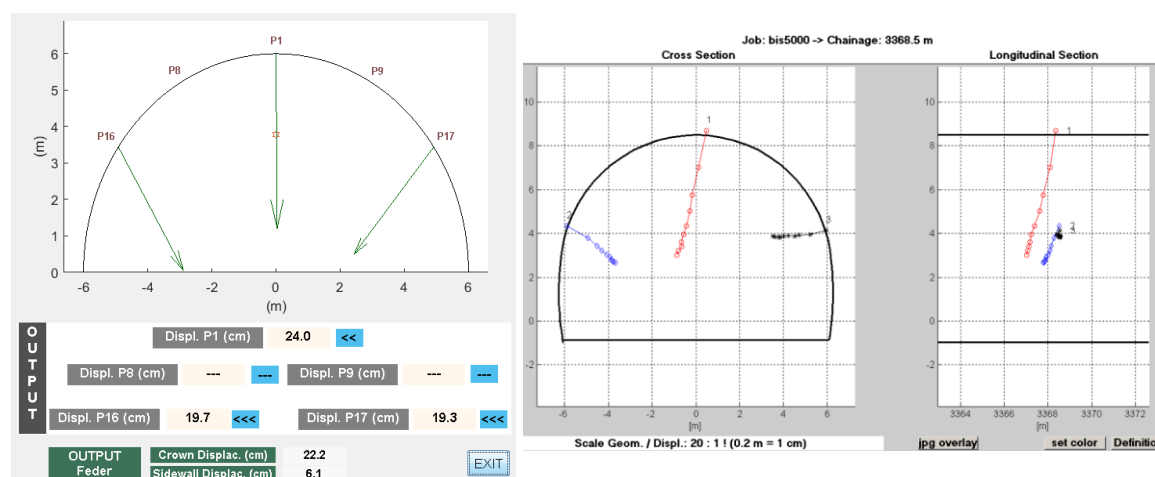


Fig. 103: Displacements prediction and monitored data (Geofit®) _ Stregen tunnel, cross section: k 3+364

Sections 4.1.1 and 5.1.3 described the expected behavior of a weakness plane orientated towards the direction of tunneling, framed by large displacements at the crowns and a rather low rotation of the displacement vector. The documented displacements on the contrary display large clockwise rotation for monitoring points 1 and 17 and counter clockwise rotation for monitoring point 16 (see Fig. 104). Displacement magnitude trend is well depicted by the prediction tool

matching the monitoring point with largest displaces (point 1) and setting monitoring point 16 and 17 to similar displacement values.

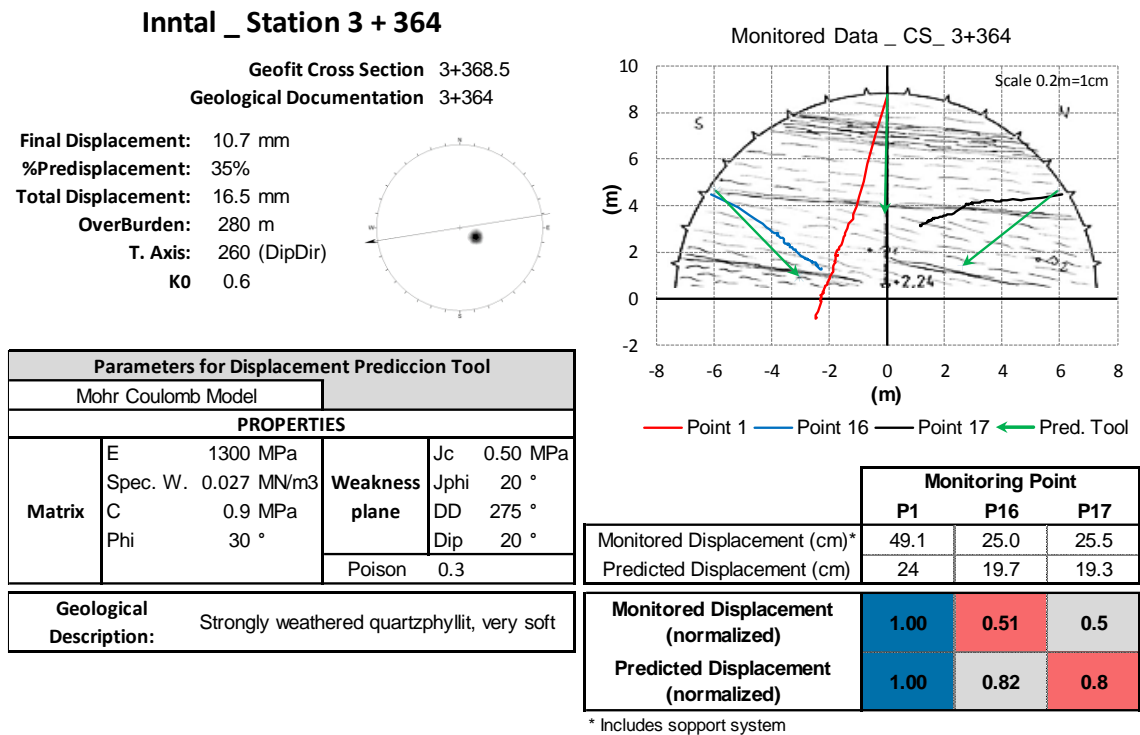


Fig. 104: Comparison between monitored and predicted displacements _ Inntal tunnel, cross section: k 3+364

The evaluation of the prediction tool should to take into consideration that the prediction tool has a back ground based on Feder’s basic solution and on data gathered through numerical simulation using the ubiquitous joint model, both scenarios are framed by ideal conditions in terms of homogeneity throughout the cross section. Ideal conditions are not often found in everyday projects where the geological complexity plays a major role in the overall displacement behavior.

The displacement prediction was compared with 4 different cross section found at 3 projects in Austria. Considering the above mentioned complexity, the overall behavior in the cross section is well captured by the prediction tool. Particularly the assessment of the areas (monitoring points) where larger displacements are expected, can be useful for design considerations.

7. CONCLUSIONS

Through this study, the importance and large impact of the relative orientation between a weakness plane and the tunnel axis on the ground behavior has been shown. The subject has been addressed by multiple authors whose observations and conclusions have been taken into consideration either to assess or to validate observed trends.

The study addressed the subject simulating such geological structures (weakness planes) by using numerical simulations in a continuum approach (Ubiquitous Joint Model). The model was selected in order to reach a significant number of conditions varying relative orientation, material properties and stress conditions. Initially the capability of the numerical model to achieve realistic results was evaluated by means of a comparison between monitored displacement data from the Galgenberg tunnel in Austria and the results delivered by the numerical model.

A complete summary of the relative orientation influence was accomplished in the study. However, only general trends regarding the ground (matrix and weakness planes) parameters influence were reached, mainly due to the limitation of the implemented numerical approach.

The result and conclusion shown in the study apply to rock masses exhibiting a statistical homogeneity in joint properties and spacing, features that are often found in metamorphic rocks entailing a foliation.

The relative orientation of the weakness plane showed a direct influence on the ground behavior, increasing displacements in the area where the weakness planes lead to stress concentration and exhibiting rotation patterns on the displacement vector. In general terms, the variation of the behavior is related, on the one hand, to a sliding and/or bending aptitude and, on the other hand, to a variation of the displacements ahead of face, both induced by the weakness planes dip angle in combination to its relative orientation with respect to the tunnel axis.

The weakness planes influence on the displacement magnitude should be considered in order to properly assess required over-excavation to account for displacements, support requirements and excavation sequences during design. The study showed the importance of including such influence and the shortcomings of classification schemes or simplifications where the weakness planes are smeared into a continuum. Such approaches lead to predetermined support/sequence arrangements ignoring the heterogeneous displacement distribution displayed by such rock masses. Trends regarding displacement vector rotation are a useful tool during construction to correctly interpret displacement monitoring data and being able to assess variations with respect to an established "normal behavior".

A computation interface was assembled summarizing the main findings of this study. The interface is considered a practical tool for designers and geotechnical engineer on site in order to include and understand the influence of such geological structures on the ground behavior.

8. REFERENCES

- [1] Goricki, A., Button, E., Schubert, W., Poetsch, M. & Leitner, R.: The influence of Discontinuity Orientation on the Behavior of Tunnels; In: Felsbau 23 (5), pp. 12-18; Essen; (2005)
- [2] Adhikary, D.: Shortcomings in the Standard Continuum Based Implicit Joint Model of Layered Rocks; In: Journal of Geology and Mining Research 2 (2), pp.23-28; Australia; (2010)
- [3] Daller, J., Riedmüller, G. & Schubert, W.: Zur Problematik der Gebirgsklassifizierung im Tunnelbau; In: Felsbau 12 (6), pp. 443-447; Essen; (1994)
- [4] Palmström, A. & Broch, E.: Use and Misuse of Rock Mass Classification Systems with Particular Reference to the Q-system; In: Tunnelling and Underground Space Technology 21 (6), pp. 575-593; (2006)
- [5] International Tunneling Association (ITA): Guidelines on Contractual Aspects of Conventional Tunneling; In: ITA Report N. 13; (2013)
- [6] Riedmüller, G. & Schubert, W.: Critical Comments on Quantitative Rock Mass Classifications; In: Felsbau 17 (3), pp. 164-167; (1999)
- [7] Schubert, W.: Some Remarks on Current Rock Engineering Design Practices; In: Rock Engineering & Technology for Sustainable Underground Construction. Proc. Eurock 2012, Stille, H. (ed); Stockholm; (2012)
- [8] Riedmueller, G. & Schubert, W.: Rock Mass Modeling in Tunneling Versus Rock Massing Classification Using Rating Methods. In: Rock Mechanics for Industry; Proc. 37th U. S. Rock Mechanics Symp., Amadei, B., Kranz, R., Scott, G. & Smeallie, P. (eds), Vol. 2, pp. 601-605; Vail; (1999)
- [9] Schubert, W.: Are Classification Systems Outdated?; In: Rock Mechanics for Resources, Energy and Environment. Proc. Eurock 2013, Kwasniewski & Łydzba (eds), pp. 831-834; Wrocław; (2013)
- [10] Hoek, E. & Brown, E.: Practical Estimates of Rock Mass Strength; In: Int. J. Rock Mech. Min. Sci. 34 (8), pp. 1165-1186; (1999)
- [11] Peck, R.: Advantages and Limitation of the Observational Method in Applied Soil Mechanics; In: Geotechnique 19 (2), pp. 171-187; (1969).
- [12] Davila, J., Kluckner, A. & Schubert, W.: Applying the Observational Approach for Tunnel Design; In: Rock Characterisation, Modelling and Engineering Design Methods, pp 691-696; London; (2013)
- [13] Schubert, W.: The Development of the Observational Method; In: Geomechanik und Tunnelbau 1, pp. 352-357; Berlin; (2008).
- [14] Moritz, B. & Schubert, W.: Application of the Observational Method within the Geotechnical Safety Management; In: Geomechanik und Tunnelbau 2 (3), pp. 269-281; Berlin; (2009).
- [15] Austrian Society for Geomechanics (OeGG): Guideline for the Geotechnical Design of Underground Structures with Conventional Excavation; Salzburg: In-house publication; (2010)

- [16] British Standards Institutions: BS 5930 Code of Practices for Site Investigations; (1999)
- [17] Button, E. & Bluemel, M.: Characterization of Phyllitic and Schistose Rock Masses: from System Behavior to Key Parameters; In: Rock Engineering - Theory and Practice. Proc. 53rd Geomechanics Colloquy & EUROCK 2004, W. Schubert (ed), pp. 459-464; Salzburg; (2004)
- [18] Button, E.: Characterization of Phyllites for Tunneling; In: Int. J. Rock Mech. Min. Sci. 41, pp. 396 - 396; (2003)
- [19] Einstein, H., Venezino, D., Baecher, G. & O'Reilly, J.: The Effect of Discontinuity Persistence on Rock Slope Stability; In: Int. J. of Rock Mech. 5, pp. 227-236; (1993)
- [20] Barton, N.: The Shear Strength of Rock and Rock Joints; In: Int. J. Rock Mech. Min. Sci. & Geomech. Abstr. 13 (9), pp 255-279; (1976)
- [21] Bluemel, M. & Bezat, F.: Advanced Control Techniques for Direct Shear Testing of Jointed Rock Specimens; Nondestructive and Automated Testing for Soil and Rock Properties, ASTM STP 1350; West Conshohocken; (1998)
- [22] Deisl, F.: Numerische Simulation von Felskluftparametern mittels des zweidimensionalen Finite Differenzen Programmes UDEC; Master Thesis; Technical University of Graz; (1998)
- [23] Jade, S. & Sitharam, T.: Characterization of Strength and Deformation of Jointed Rock Mass Based on Statistical Analysis; In: Int. J. of Geomech. 3 (1), pp. 43-54; (2003)
- [24] Hoek, E. & Brown, E.: Practical Estimates of Rock Mass Strength; Int. J. Rock Mech. Min. Sci. 34 (8), pp. 1165–1186; (1998)
- [25] Palmström, A.: Measurement and Characterization of Rock Mass Jointing, In: In-Situ Characterization of rocks, chapter 2; Norway; (2001)
- [26] Amadei, B. & Stephansson, O.: Rock Stress and its Measurement; Chapman & Hall; United Kingdom; (1997)
- [27] Goodman, R.: Methods of Geological Engineering in Discontinuous Rocks; West Publishing CO., pp. 159 - 165; Saint Paul; (1976)
- [28] Sugawara, K. & Obara, Y.: Measuring Rock Stress; In: Comprehensive Rock Engineering, J. A. Hudson (ed.), chapter 21; Oxford; (1993)
- [29] Savin, G.: Stress Concentration Around Holes; Pergamum Press; Oxford; (1961)
- [30] Love, A.: A Treatise on the Mathematical Theory of Elasticity; Update forthcoming (ed.); New York; (1927)
- [31] Feder, G. & Arwanitakis, M.: Zur Gebirgsmechanik Ausbrunnaher Bereiche Tiefliegender Hohlräumbauten; In: Berg- und Hüttenmännische Monatshefte 121 (4), pp. 103-117; New York; (1976)
- [32] Terzaghi, K. & Richart, F.: Stresses in Rock About Cavities; In: Geotechnique 3 (2), pp 57-90; (1952)
- [33] Kirsch, G.: Die Theorie der Elastizität und die Beduernisse der Festigkeitslehre; In: Zeitschrift des Vereines deutscher Ingenieure 42, pp 797–807 ; (1898)

- [34] Brandy, B. & Brown, E.: Rock Mechanics for Underground Mining; Kluwer Academic Publishers, pp 204-209; (2004)
- [35] Hoek, E. & Brown, E.: Underground Excavations in Rock; Institute of Mining and Metallurgy, chapter 5 and 7; London; (1980)
- [36] Raji, M. & Sitharam, T.: Stress Distribution Around the Tunnel; In: Proc. of the IGC, pp. 973-976; Kochi; (2011)
- [37] Francis, E.: Determination of the Influence of Joint Orientation on Rock Mass Classification for Tunneling; In: Journal of Engineering Geology and Hydrogeology 24, pp. 267-273; (1991)
- [38] Bieniawski, Z.: Engineering Rock Mass Classification; John Wiley and Sons; New York; (1989)
- [39] Vardar, M.: Zeitenfluss auf das Bruchverhalten des Gebirges in der Umgebung von Tunneln; Institut fuer Bodenmechanik und Felsmechanik der Universitaet Fredericana; (1977)
- [40] Goricki, A.: Base Friction Versuche fuer felsmechanische Kluffkoerper; Institut fuer Felsmechanik und Tunnelbau der Technische Universitaet Graz; Austria; (1999)
- [41] Schubert, W., Goricki, A., Button, E., Riedmueller, G., Poelsler, P., Steindorfer, A. & Vanek, R.: Excavation and Support Determination for the Design and Construction of Tunnels; In: Proc. Int. symposium of the ISRM, Sarkka P. & Elorante P. (eds), pp. 383-388; Finland; (2001)
- [42] Steindorfer, A. & Schubert, W.: Application of New Methods of Monitoring Data Analysis for Short Term Prediction in Tunnelling; In: Proc. World Tunnel Congress, Golser J., Hinkel W. & Schubert W. (eds), Vol.1; Vienna; (1997)
- [43] Schubert, W. & Budil, A.: The Importance of Longitudinal Deformation in Tunnel Excavation; In: Proc. 8th Inter. Congress of Rock Mecha., Fujii T. (ed), pp 1411-1418 ; Tokyo; (1995)
- [44] Grossauer, K., Schubert, W. & Lenz, G.: Automatic Displacement Monitoring Data Interpretation; In: Proc. 42nd Rock Mechanics Symposium, Wilson S., Ewy R. & Tutuncu A. (eds), pp. 1084-1090; San Francisco; (2008)
- [45] Kluckner, A.: Aspekte der Gebirgskarakterisierung im Tunnelbau; Institut fuer Felsmechanik und Tunnelbau der Technische Universitaet Graz; Austria; (2012)
- [46] 3G Gruppe Geotechnik Graz, ZT GmbH
- [47] Jing, L. & Hudson, J.: Numerical Methods in Rock Mechanics; In: Int. J. Rock Mech. and Min. Sci. 39 (4), pp. 409-427; United Kingdom; (2002)
- [48] Rziha, Franz.: Lehrbuch der gesamten Tunnelbaukunst I; Ernst & Sohn; Berlin; (1872)
- [49] Terzaghi, K.: Rock Defects and Load on Tunnel Supports; In: Rock Tunneling with Steel Supports, pp. 17-99; Ohio; (1946)
- [50] Stini, J.: Tunnelbaugeologie; Springer-Verlag; Austria; (1950)
- [51] Coates, D.: Classification of Rocks for Rock Mechanics; In: Rock Mech. and Mining Sci. 1, pp. 421-429; (1964)

- [52] Wickham, G., Tiedemann, H. & Skinner, E.: Support Determination Based on Geologic Prediction; In: Proc. 1st North American Rapid Excavation & Tunnelling Conference, pp. 43-64; (1972)
- [53] Barton, N., Lien, R. & Lunde, J.: Engineering Classification of Rock Masses for the Design of Rock Support; In: Rock Mechanics 6 (4), pp. 189-236; (1974)
- [54] Bieniawski, Z.: Engineering Classification of Jointed rock Masses; In: Trans S. Afr. Inst. Civ. Engineers, pp.335-344; (1973)
- [55] Bieniawski, Z.: Rock mass classification in Rock Engineering; In: Exploration for Rock Engineering, pp. 97-106; Cape Town; (1976)
- [56] Palmström, A.: RMI – a Rock Mass Characterization System for Rock Engineering Purposes; Doctoral Thesis; Norway; (1995)
- [57] Palmström, A.: Recent developments in Rock Support Estimates by The RMI; In: J. of Rock Mecha. and Tunneling Technology 6 (1), pp. 1-19; (2000)
- [58] Gibson, R.: The Analytical Methods in Soil Mechanics; In: Geotechnique 24 (2), pp. 115-140; (1974)
- [59] Brown, E.: Analytical and Computational Methods in Engineering Rock Mechanics; E.T. Brown. George Allen & Unwin Ltd.; London; (1987)
- [60] Jing, L.: Fundamentals of Discrete Element Methods for Rock Engineering; L. Jing and O. Stephansson (eds); Netherlands; (2007)
- [61] Shen, B. & Barton, N.: The Disturbed Zone Around Tunnels in Jointed Rock Masses; In: Int. J. Rock Mech. Min. Sci. 34 (1), pp. 117-125; (1997)
- [62] Button, E., Leitner, R., Poetsch, M. & Schubert, W.: Spatial Relationships Between Discontinuity Orientation and System Behavior in Underground Excavations; In: Proc. 41st U.S. Symposium on Rock Mecha., Yale D. (ed), Vol 1, pp. 165-175; Golden; (2005)
- [63] Ferrero, A., Migliazza, M. & Giagi, P.: Analysis of Tunnel Stability: Comparison Between Continuous and Discontinuous Approaches; In: Int. J. Rock Mech. Min. Sci. & Geomech. 41 (1), pp. 646-651; (2004)
- [64] Yeo, Oliver.: Comparison of Finite Difference and Finite Volume Methods; Academic project at the National University of Singapore; (2010)
- [65] Solak, T.: Influence of the Geological Features Block Size, Shape and Joint Strength on the Ground Behavior; Institute for Rock Mechanics and Tunneling; Doctoral Thesis; (2007)
- [66] Riahi, A., Hammah, E. & Curran, J.: Limits of Applicability of the Finite Element Explicit Joint Model in the Analysis of Jointed Rock Problems; In: Proc. 44th U.S. symposium on Rock Mecha., pp. 1057-1066; Salt Lake City; (2010)
- [67] Tzamtzis, A.: Finite Element Modeling of Cracks and Joint in Discontinuous Structural System; 16th ASCE Engineering Mechanics Conference; (2003)
- [68] Wittke, W.: Rock Mechanics: Theory and Application with Case Histories; Berlin Springer; (1990)
- [69] Hammah, E., Yacoub, T., Corkum, B. & Curran, J.: The Practical Modeling of Discontinuous Rock Masses with Finite Element Analysis; In:

- Proceedings, 42nd Rock Mechanics Symposium, Ewy R. & Tutuncu A. (eds), pp. 436-443; San Francisco; (2008)
- [70] Klopčič, J.: Analysis and Prediction of Displacements for Tunnel in Foliated Rock Masses of Perm-carboniferous Age; Doctoral Thesis; University of Ljubljana; Slovenia; (2009)
- [71] Kazakidis, V. & Diederichs, S.: Understanding Jointed Rock Mass Behavior Using a Ubiquitous Joint Approach; In: Int. J. Rock Mech. Min. Sci. & Geomech. 30 (2), pp. 163-172; (1993)
- [72] Singh, M., Singh, B., Choudhari, R. & Goel, R.: Constitutive Equation for 3-D Anisotropy in Jointed Rocks and Its Effect on Tunnel Closure; In: Int. J. Rock Mech. Min Sci, & Geomech. 41 (1), pp. 652-657; Ontario; (2004)
- [73] Goricki, A., Schubert, W. & Riedmueller, G.: New Developments for the Design and Construction of Tunnels in Complex Rock Masses; Int. J. Rock Mech. Min Sci, & Geomech. 41 (3), pp. 720-725; Ontario; (2004)
- [74] Kavvadas, M.: Monitoring Ground Deformation in Tunneling: Current Practice in Transportation Tunnels; In: Engineering Geology 79 (1), pp. 93-113; Athens; (2004)
- [75] Schubert, W.: Displacement Monitoring in Tunnels – an Overview; In: Felsbau 20 (2), pp. 7-15, Essen; (2002)
- [76] Grossauer, K.: Expert System Development for the Evaluation and Interpretation of Displacement Monitoring Data in Tunneling; Institute for Rock Mechanics and Tunneling; Doctoral Thesis; (2009)
- [77] Einstein, H.: Quantifying Uncertain Engineering Geologic Information; In: Felsbau 19 (5), pp. 72-84; USA; (2001)
- [78] Kluckner, A.: Aspekte of Gebirgscharakterisierung im Tunnelbau; Institute for Rock Mechanics and Tunneling; Master Thesis; (2012)
- [79] Itasca FLAC3D: User Manuals; (2002)
- [80] Kellich, W., Lee J., Aziz N. & Baafi E.: Numerical Modeling of Undermined River Valleys - A Case Study; In: Coal Operator' Conference, pp. 39-48; (2005)
- [81] Meissner, H.: Empfehlungen des Arbeitskreises 1.6 „Numerik in der Geotechnik“ abschnitt 2, Kaiserslautern
- [82] Schubert, P.: Beitrag zum rheologischen Verhalten von Spritzbeton; Felsbau 6 (1), pp. 150-153; (1988)
- [83] Geologiebüro - Dr. Werner FÜRLINGER: Galgenbergtunnel Geologischer Laengsschnitt der aufgefahrenen Gebirgsverhaeltnisse; (1993)
- [84] Hoek, E., Carranza, C., Diederichs, M. & Corkum B.: The 2008 Kersten Lecture Integration of Geotechnical and Structural Design in Tunneling; Annual Geotechnical Engineering Conference; Minneapolis; (2008)
- [85] Carranza-Torres, C. & Fairhurst, C.: Application of the Convergence-Confinement Method of Tunnel Design to Rock Masses that Satisfy the Hoek-Brown Failure Criterion; Tunneling and Underground Space Technology 15 (2), pp. 187-213; (2000)

- [86] Sellner, P.: Prediction of Displacements in Tunneling; Institute for Rock Mechanics and Tunneling; Doctoral Thesis; (2000)
- [87] Geologiebüro – Alpen Strassen AG_TIWAG: Geologische Dokumentation Strengen Tunnel; (2002)
- [88] Geologiebüro - ILF_Consulting Engineers: Baugeologische Dokumentation Inntaltunnel; (1991)